Computational Hyperspectral Microscopy for Bioimaging

Neerja Aggarwal

Electrical Engineering and Computer Sciences
University of California, Berkeley

Technical Report No. UCB/EECS-2025-83
http://www2.eecs.berkeley.edu/Pubs/TechRpts/2025/EECS-2025-83.html

May 16, 2025

Computational Hyperspectral Microscopy for Bioimaging

by

Neerja Aggarwal

A dissertation submitted in partial satisfaction of the

requirements for the degree of

Doctor of Philosophy

in

Engineering - Electrical Engineering and Computer Science

in the

Graduate Division

of the

University of California, Berkeley

Committee in charge:

Professor Laura Waller, Chair
Professor Miki Lustig
Professor Gokul Upadhyayula

Spring 2025

Computational Hyperspectral Microscopy for Bioimaging

Abstract

Computational Hyperspectral Microscopy for Bioimaging

by

Neerja Aggarwal

Doctor of Philosophy in Engineering - Electrical Engineering and Computer Science

University of California, Berkeley

Professor Laura Waller, Chair

Hyperspectral imaging involves detecting the spectrum (intensity vs wavelength) of light emitted at each point in space. It has applications in biology such as fluorescence imaging of live cells and interferometry to see inside tissues. However, traditional hyperspectral systems often have to scan through this three-dimensional spatial-spectral datacube (x, y, λ) due to a 2D sensor, resulting in long acquisition times and large setups. Snapshot imaging fits the entire 3D datacube onto a 2D sensor at once but sacrifices resolution. Computational imaging involves the codesign of both optics and algorithms together to beat traditional tradeoffs. In this work, we present three imaging systems for various bioimaging applications that benefit from computational imaging to improve spectral imaging performance.

In the first application, we redesigned a traditional spectrometer using a diffuser instead of a grating to diffract light. The resulting speckle pattern was captured using an image sensor and inverted to solve for the spectrum. This compact spectrometer was developed for optical coherence tomography, an interferometry technique for imaging eyes.

In the second project for fluorescence microscopy, we used a diffuser to multiplex light onto a spectral filter array on an image sensor. We used compressed sensing to solve for more voxels in the hyperspectral data cube than pixels on the sensor. We developed a compact attachment for a traditional benchtop microscopy that enables live imaging on biological samples and demonstrate high fidelity reconstructions in experiment.

In the final project, we adapted a Fourier ptychography system for spectral imaging using a filter array. Fourier ptychography uses angled illumination to scan through the spatial Fourier plane and build up a higher resolution image. By placing the filter array in the Fourier plane, we can scanned the object's spatial frequencies through each spectral filter to build up a high resolution spatio-spectral datacube. We investigated this idea via simulation and proposed an experimental setup that could be used for digital pathology.

Contents

List of Figures

Acknowledgments

I've been looking forward to the day when I could finally say that I've completed my PhD and thank all the people who have helped me get here. Science doesn't hapeen in a vacuum; we stand on the shoulders of giants for every advancement. First of all, I would like to thank my advisor Laura Waller. I'm so grateful to have had such a kind, supportive, and enabling advisor. Laura's scientific leadership and reputation is an inspiration. She attracts brilliant and kind scientists to her group and gives them the freedom to explore their ideas.

The Computational Imaging Lab at UC Berkeley has been such a welcoming and creative group to be a part of the past six years. I've been lucky to learn from them. I'd like to especially thank Eric Markley who worked on two of my main projects with me. I learned so much from his applied math background and computational skills, and it was way more motivating to show up to work each day when I had a co-author to collaborate with. There are so many others in the lab who have made my time here special - Amit Kohli was a joy to share an office cubicle with. I always felt more relaxed and hopeful after our conversations - plus had fun testing a telescope together. Tiffany Chien and I enjoyed many lunches together as office mates. Thanks also to Ruiming Cao, Leyla Kabuli, Charles Dove, Henry Pinkard, Guanghan Meng, Yunzhe Li, Mingxuan Cai, Chaoying Gu, Kevin Zhou for being such great colleagues always willing to converse. I also had the pleasure of overlapping with Ruizhi Cao, Loza Tadesse, Sixian Yu, Ryan Mei, Nalini Singh. I also want to thank Kristina Monakhova and Kyrollos Yanny who mentored me through my first year in the lab. Thanks to Zack Philips for initially recruiting me for the lab, mentoring me during my summer internship, supporting my spectral ptychography work. Thank you also to my undergrad researchers, especially Yashovardhan Raniwala, for letting me be a part of their research journey.

I also want to thank my qual committee: Ren Ng, Gokul Upadhyayula, and Miki Lustig for their helpful feedback in guiding my research. Thank you to Gokul and Miki for continuing on as thesis committee members. Thanks to Babak Ayazifar and Steve Connolly for giving me a chance to teach my love of signals and systems and imaging to the Berkeley undergrads.

I have so many other labs and institutions that helped transform me into the scientist-engineer I am today. At MIT, I was fortunate to be mentored by Rajeev Ram, Janet Sonenberg, Vladmir Bulovic, and Neri Oxman. At Rice, I got my lucky break to do scientific research as a high school student in the lab of Andrew Barron under the guidance of Alvin Orbaek. I've also had so many teachers who have supported and believed in me throughout my academic career - thank you to them all.

Now moving on to the people who have supported my personally through my life. Despite being the weird science one in my family, I've always been encouraged to pursue my dream. My parents Uma and Gopal Aggarwal who taught me diligence, hard work, and persevering towards your vision no matter the challenges in the way. My sister, Supriya Aggarwal, was my first math teacher and nurtured my love of math and science at a young age. My brother, Raghav Aggarwal, and I spent time coworking and adventuring during my Ph.D. My brother-in-law Ari Meher Homji has also been very kind and encourging through the journey. My

partner Alexander Mouschovias has been a constant source of love, patience, kindness, and encouragement. We had many adventures together and I'm excited to continue exploring and growing with him. My fellow Ph.D. student Meg Everett was the best roommate a girl could ask for. Thank you to my special friends Daniel Kramnik, Vaish Ramesh, Natalia Luka, Clarissa Bhargava, and many others. Thank you to the Burnell-Schafer family (Ruth, Michael, Ned, and Nevin) for opening their Mendocino home to me as a retreat. I'd also like to thank the extended Aggarwal-Nagori family for being a part of my life. Through their support, I became one of the first to earn a Ph.D. and I hope it inspires others to also pursue science.

Any creative process - engineering, art, science - is about pushing boundaries to learn something new about our universe. And in doing so, to learn something new about ourselves.

Chapter 1

Introduction

Light interacts with matter in fascinating ways. In 1928, Indian scientist Sir C.V. Raman discovered that filtered sunlight changes wavelength when scattering through a liquid [46]. This phenomenon became known as Raman scattering and is the basis of Raman spectroscopy. Other spectroscopy techniques like fluorescence, phosphorescence, and infrared spectroscopy probe the internal structure of matter via radiation induced electronic and molecular transitions. Through absorbance, transmission, refraction, and scattering, light offers a noninvasive way to probe the properties of matter. We can use light to learn about the structure and function of biological samples. One way to do this is to analyze the wavelength components of the emitted light.

However to do this, we must capture and measure light and that is where imaging systems come in. From the early days of Leeuwenhoek in the 1600s to modern day super-resolution microscopes, we have pushed the limits of optical techniques mostly via advancement in hardaware. The advent of computational imaging, which is the codesign of hardware and software, has given a new direction to continue innovation.

The rise of computation and machine learning allows us to make sense of the data captured via these light-matter imaging systems. We are no longer limited by our ability to analyzed data, but rather to produce it. And so, the aim of this thesis is to push the limits of high-throughput hyperspectral imaging systems through the codesign of optics and algorithms. We extract hyperspectral information with optimized imaging systems and computational methods in hopes of learning new insights about the samples we study.

In this chapter we first present some background technical knowledge relevant to hyperspectral imaging and computational imaging. Next, we share a toolbox of components and discuss the imaging applications relevent for the projects in this thesis.

1.1 Background

Hyperspectral imaging involves capturing light from a scene at multiple wavelengths and points. It has a wide range of applications, including biological microscopy, medical imaging,

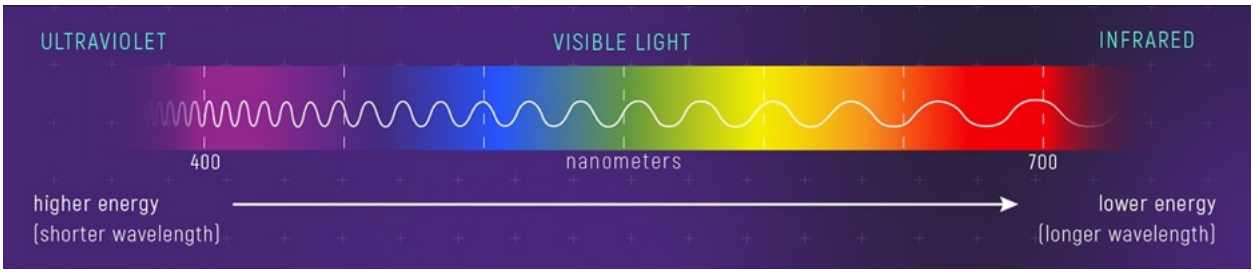

Figure 1.1: Electromagnetic spectrum from ultraviolet to near infrared. Figure from NASA Webb Space Telescope.

remote sensing, satellite imaging, materials science, food science, and art conservation. Here we review the basics of light and light matter interactions before discussion hyperspectral imaging in detail. Then we discuss the basics of computational imaging which involve image formation and reconstruction.

Fundamentals of Light

Light is electromagnetic radiation composed of oscillating electric and magnetic fields. All light fields can be expressed as a sum of plane waves. The electric field component of a plane wave propagating through space can be written as:

$$E(x, y, z, t) = A_0 e^(i(k_x x + k_y y + k_z z - \omega t + \phi_0)) \tag{1.1}$$

The vector $\mathbf{k} = k_x\hat{x} + k_y\hat{y} + k_z\hat{z}$ determines direction of propagtion. The wavelength between common phase fronts in this wave is related to the propagation vector by $\lambda = 2\pi/|\mathbf{k}|$. The wavelength of light in free space is related to the perceived color as shown in Figure 1.1. We will refer to the wavelength of the light often in hyperspectral imaging.[1]

Light as a wave has both amplitude and phase. The amplitude is given by the constant A_0. As light transmits through and is absorbed by various materials, this amplitude decreases. The phase of light is given by the term in the exponential: $k_x x + k_y y + k_z z - \omega t + \phi_0$. Here ϕ_0 is any initial phase. The term ωt indiciates that the phase oscillates even at a fixed position in space through time (since light is a wave). The terms $k_x x + k_y y + k_z z$ show that the phase increases linearly along the propagation direction. Light can accumulate additional phase as it passes through medium with refractive index $n > 1$. For a given thickness h of material with index n, the total accumulated phase is $\phi = \frac{hn}{2\pi}$.

The beauty of light is that it is noninvasive and can probe properties of samples. Here we briefly discuss such phenomenon. Light matter interactions relevant to hyperspectral imaging in the UV-NIR are shown in Figure 1.2 and include:

[1]The physical wavelength of light can change inside different media. The oscillation frequency ω of light which remains constant is a more consistent identifier. The wavelength in free space is related to the frequency by $\lambda = \frac{2\pi c}{\omega}$ where c is the speed of light in free space (aka vacuum). Hence when we mention wavelength from now on, we refer to the wavelength in free space.

- Reflection, refraction, and transmission at boundaries between materials which can be wavelength dependent
- Absorption and fluorescence emission of light by atoms and materials
- Scattering phenomena such as Raman, Rayleigh, and Mie which can change the wavelength profile of incident light.
- Dispersion of light (i.e. nonuniform phase delay across wavelengths) through medium
- And more

We discuss the specific phenomemon relevant for the projects in this theses later in this chapter.

Hyperspectral Imaging

Spectroscopy is the measure of electromagnetic spectra and its interpretation. It allows the physical structure, composition, and electronic structure of matter to be investigated due to the light-matter interactions listed above. Whereas traditional spectroscopy usually analyzes either bulk or single point emission from a sample, hyperspectral imaging attempts to build a spatially resolved profile of wavelengths (or colors) in the emitted light.

The shift from sensing a single point to imaging a whole scene at multiple wavelengths requires changes in the optics hardware and strategies for acquiring the full hyperspectral datacube. For our discussion, this datacube consists of two spatial axes and one spectral (wavelength) axis: $v(x, y, \lambda)$.

There are three different types of capture schemes in hyperspectral imaging:

- spatial scanning
- spectral scanning
- snapshot (no-scanning)

In spatial scanning cases, the hyperspectral datacube is built through sequential scanning of different points in space. This includes point scanning and line scanning (aka pushbroom) systems. Examples include confocal fluorescence microscopes with spectral attachments (ex: Nikon) and many remote sensing systems (ex: Headwall). The image is built up slowly over time and this system cannot capture rapidly changing scenes accurately. In spectral (or wavelength) scanning systems, the entire field of view is captured in every exposure but limited to single wavelength channel. Filter wheels on fluorescence microscopes could fall in this category. The third scheme is snapshot which attempts to capture the entire hypercube in a single acquisition. In the case of one to one mapping between voxels in the scene and pixels on the sensor, the spatio-spectral resolution of the datacube is limited.

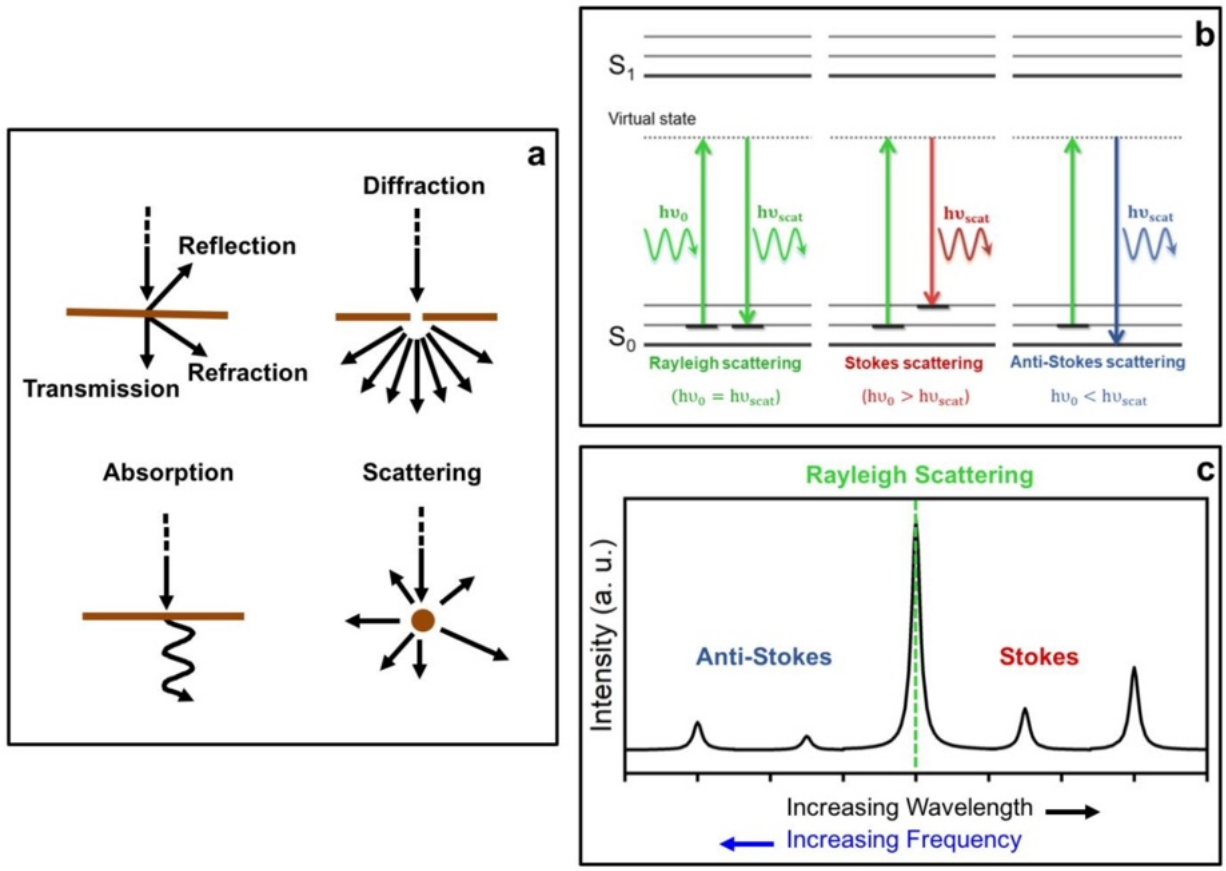

Figure 1.2: Various light matter interactions. a) shows common interactions when propogating through dielectric media. b) and c) show Raman and Rayleigh scattering processes. Figure from Reference [57]

Thus, the goal of the projects in thesis is to achieve high-resolution snapshot hyperpsectral imaging for various applications. In chapter 2, we discuss a compact spectrometer for optical coherence tomography. The vision of that research project was to work towards a snapshot system, however a spatial scanning system is demonstrated so far. In chapter 3, we discuss improving the resolution of a snapshot fluorescence microscope using multiplexing to purposefully spread out the light across the sensor. Finally in chapter 4, we discuss a new idea of scanning in spatial frequency and build up the hyperspectral datacube in Fourier space.

The engineering trade-offs in an hyperspectral imaging system include size, sensitivity, cost, speed, number of reconstructed voxels/channels, and spatio-spectral resolution [2].

[2]Note: the spectral resolution in hyperspectral imaging is not solely determined by the number of spectral channels reconstructed as is sometimes assumed in literature. It is characterized by the resolvability

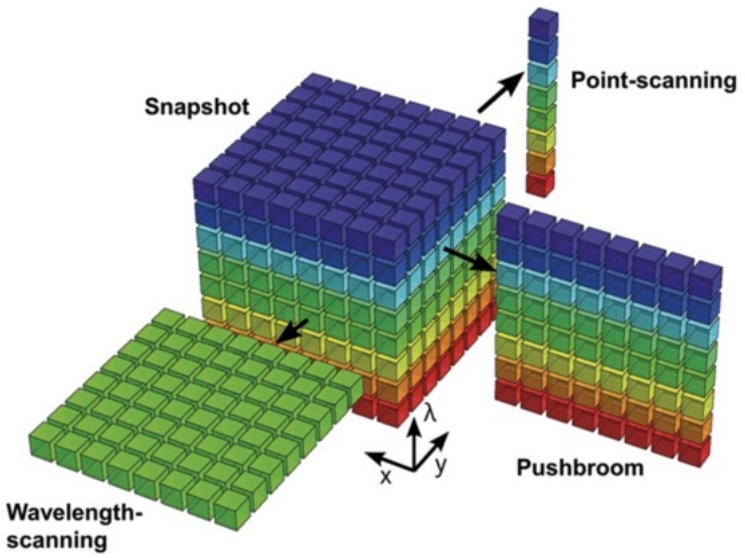

Figure 1.3: Hyperspectral scanning and snapshot techniques shown on the datacube. Each inset shows the voxel slice acquired by a single acquisition of that technique. Snapshot techniques capture the full datacube. Figure from Reference [17]

Through computational imaging, we hope to improve this tradeoff space.

Computational Imaging

Computational imaging is the codesign of hardware and software to push the limits of traditional imaging. It has many applications across science and engineering including optical microscopy, astronomical imaging, remote sensing, medical imaging, etc.

A computational imaging system usually consists of two stages:

1. The image formation process in which light from a sample is captured and converted into information bits via a sensor.

2. The conversion of the measured image into a reconstruction of the intended scene.

In contrast, traditional imaging consists of only the first stage. The load of creating an image which matches the spatial profile of the object lies solely on the hardware. This is shown in Figure 1.4.

Beyond these two stages of image formation and reconstruction, the computational imaging workflow can also consist of subequent post-processing such as segmentation, classification, or other tasks.

---

of monochromatic peaks which is largely affected by the condition number of the system as we'll discuss later.

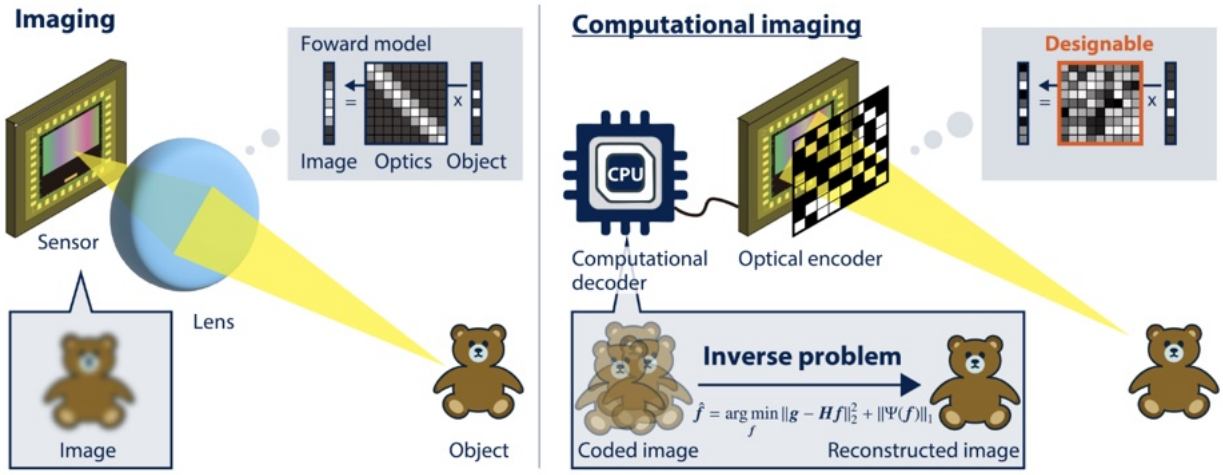

Figure 1.4: Hyperspectral scanning and snapshot techniques shown on the datacube. Each inset shows the voxel slice acquired by a single acquisition of that technique. Snapshot techniques capture the full datacube. Figure from Reference [67]

Image formation

For the first stage, a typical image formation process could be the convolution of an object, $v(x, y)$ with the point spread function (PSF), $h(x, y)$, which dictates how a point in the scene spreads out on to the sensor. If this PSF does not vary based on the location of the originating point, we call this system shift-invariant. If the final image, $m(x, y)$, is the sum of the contributions from all the points in the object, the system also obeys linearity. A linear, shift-invariant system can be modeled via a convolution operation.

$$m(x, y) = v(x, y) * h(x, y) \tag{1.2}$$

This can also be computed in Fourier space as the elementwise multiplication of the Fourier transforms of the object and the PSF.

$$\tilde{M}(k_x, k_y) = \tilde{V}(k_x, k_y)\tilde{H}(k_x, k_y) \tag{1.3}$$

Another representation of this same process uses linear algebra. Here, we vectorize the pixels in the object and the sensor into $\mathbf{v}$ and $\mathbf{h}$. Then the convolution operation can be executed using a circular matrix $\mathbf{C}$ which contains the shifted PSFs for each row.

$$\mathbf{m} = \mathbf{C}\mathbf{v} \tag{1.4}$$

The important thing to note here is that we've represented the same image formation process three different ways. This is because often the process is faster to compute in Fourier domain and easier to understand using linear sytems.

The image formation model is also typically called the "forward model" which helps us move from object to measurement or image space. It is important to accurately model the image formation process, or the foward model, otherwise errors and artifacts are introduced during reconstruction. These inaccuracies in the forward model could be due to miscalibration, nonideality in the assumptions, or lack of knowledge of the system. For example, a slightly shift varying PSF would break the shift-invariant assumption. Sometimes, it's easier to fix these in accuracies in hardware (ex: realighn the setup and improve the optics to obtain shift invariance). And other times, it's easier to mitigate them in software (ex: learn the LED positions for a Fourier Ptychography setup). The forward model along with guidance for assumptions and calibration for each project is discussed in detail in the subsequent chapters.

Reconstruction

The reconstruction process can rely on knowledge of the image formation model to invert the scene. This section assumes a basic knowledge of linear algebra; reference [20] Chapter 2 provides a good background and is available online for free.

If we generalize any imaging system into the operator, $\mathbf{A}$, which acts on an object, $\mathbf{v}$, to produce the measurement, $\mathbf{m}$ we can write:

$$\mathbf{A}\mathbf{v} + \mathbf{n} = \mathbf{m} \tag{1.5}$$

Here $\mathbf{n}$ is additive noise in the system, a stochastic process which affects the measurement. The inverse problem we must solve consists of recovering the object given a sensor measurement. A common approach is to solve the minimum least squares problem:

$$\hat{\mathbf{v}} = \arg\min_{v} ||\mathbf{A}\mathbf{v} - \mathbf{b}||_2 \tag{1.6}$$

which attempts to minimize the L2-norm of the error between the estimated measurement $\mathbf{A}\mathbf{v}$ and the actual measurement $\mathbf{b}$. The reasoning is the recovered object should output the same image on the sensor as the experimental measurement.

The condition number of the forward matrix, A, dictates the noise amplification and the quality of the reconstruction. The condition number is given by the ratio between the largest and smallest singular values:

$$\kappa(\mathbf{A}) = \frac{\sigma_{max}(\mathbf{A})}{\sigma_{min}(\mathbf{A})} \tag{1.7}$$

If the condition number is significantly larger than 1 (ex: $\kappa = 100$), then the system is ill-conditioned. The inverse will be difficult to compute and any noise components along the singular vectors of $\mathbf{A}$ with $\sigma_i < 1$ will be amplified.

For example, If the matrix A was square and invertible, that means the system is perfectly determined and there is a one-to-one mapping between object space and measurement space.

The analytical solution takes the inverse of both sides of Equation 1.5 to solve least squares problem:

$$\hat{\mathbf{v}} = \mathbf{A^{-1}m} = \mathbf{A^{-1}}(\mathbf{Av} + \mathbf{n}) = \mathbf{v} + \mathbf{A^{-1}n} \tag{1.8}$$

The second term above indicates any additive noise in the measurement would still be amplified or attenuated based on the singular values (or in this case, eigenvalues) of $\mathbf{A}$.

However, a square, invertible $\mathbf{A}$ matrix is uncommon. More typically, the number of measurement pixels either exceeds or subceeds the number of reconstructed pixels resulting in a correspondingly overdetermined (ex: Chapter 2) or undertdetermined system (ex: Chapter 3). In such cases, the $\mathbf{A}$ matrix is ill-posed and rectangular in shape: short and fat for the undertdetermined case or tall and skinny for the overdetermined case. In an underdetermined system, there are many possible solutions to a single measurement. In an overdetermined system, the algorithm finds the closest solution that lies in the subspace of A.

To deal with the issues above, reconstruction loss functions include regularization terms:

$$\hat{\mathbf{v}} = \arg\min_{v} ||\mathbf{Av} - \mathbf{b}||_2 + R(v) \tag{1.9}$$

We use regularization for one or more of the following reasons:

- Improve the stability and robustness to noise (i.e. improve the condition number)
- Bias the solution space to be more well-defined (i.e. improve the ill-possedness)
- Incorporate existing knowledge about the object (i.e. prior information)
- Reduce overfitting of the data

The regularization and initialization determines which local minima the gradient descent problem falls into and thus which solution is selected.

The most common regularization terms include the L1 (sparsity) and L2 (Tikhonov) norms on the object. In LASSO regression, the cost function uses sparsity regularization:

$$\hat{\mathbf{v}} = \arg\min_{v} ||\mathbf{Av} - \mathbf{b}||_2 + \tau||\mathbf{v}||_1 \tag{1.10}$$

where τ is the hyperparameter controlling the relative strengths of the two terms (also commonly written as the Lagrange multiplier, λ). The L1-norm is a convex relaxation of the L0 norm which penalizes nonzero values, hence the favored solution is sparse. See Sections 1.2.2 and 2.2 of Reference [65] for deeper discussion.

In ridge regression (aka Tikhonov regularization), the L2 norm is used instead:

$$\hat{\mathbf{v}} = \arg\min_{v} ||\mathbf{Av} - \mathbf{b}||_2 + \tau||\mathbf{v}||_2 \tag{1.11}$$

This cost function will favor solutions with less energy. This problem is equivalent to using a modified $\mathbf{A}^*$ matrix with the following singular values:

$$\sigma_i(\mathbf{A}^*) = \frac{\sigma_i^2(\mathbf{A})}{\sigma_i(\mathbf{A}) + \tau} \tag{1.12}$$

In fact many regularization terms can be thought of as spectral filters [34]. In Chapter 2 we will use a filter on the $\mathbf{A}$ matrix during inversion to assist with overfitting. We can also use both L1 and L2 in the same problem. In Chapter 3 and 4 we will use multiple regularization terms and parameter tuning to improve the reconstruction quality.

Gradient descent is the basic algorithm used to solve the loss function. The optimization problem itself is solved via numerical computation using Python libraries like Pytorch and Jax which can run on GPUs to speed computation time. Before the advent autodifferentation dtools in computational imaging , we used to write the function for the adjoint operator which acted on the error $Av^{(i)} - b$ in the i-th iteration to compute the gradients for updating $v^{(i)}$ [39]. As the forward model became more and more complex, so did the adjoint operation. Additionally, the regularization terms were implemented via proximal steps after the gradient update in most algorithms used for LASSO regression (ex: ISTA and FISTA [4]). The rise of neural networks came with the tools to autodifferentiate and backpropagate through them to compute gradients with respect to a scalar loss function. We apply the same tools for solving inverse problems. Thus instead of computing adjoints and proximal steps, autodifferentiation [59] gives the total gradient of the cost function with respect to the learnable parameters incorporating partial gradients from the regularization terms. We use off the shelf optimizers like Adam [27] to accelerate the gradient descent algorithm.

For deeper discussion on computational imaging see Reference [26] and [5].

Computational Imaging Examples

Here we discuss some relatable examples of computational imaging.

Almost all modern smartphone cameras also use computational imaging. The space constraint and cost budget limits the size and specifications of the optics in the imaging chain. The load for denoising, deblurring often falls on the image signal processing firmware and software stack. Here the goal is to recolor, sharpen, or brighten the picture to be more apealing to the end user. To do so, image processing algorithms use both traditional signal processing and machine learning. Features like HDR, Portrait mode, night mode creatively use the data from the sensor with knowledge of the optics and processing algorithms to achieve the feature. Recently the use of deep learning in algorithms has become more popular to create hyperrealistic images with priors trained on large sets of natural images.

Computational imaging for scientific research requires a more rigorous approach. Here the goal is to extract possibly new information from the images to increase our knowledge of the world. One of the most famous examples of computational imaging is the picture of the M87 black hole released to the public in 2019 by NASA and the Event Horizon Telescope collaboration. Scientists reconstructed the image from a sparse network of telescopes around the world. The inverse problem was underconstrained since only a few spatial frequencies were measured and the rest of the information was filled in using additional assumptions and

constraints that are consistent with the captured data. Something about different approaches compared to yield final result. [58]

One thing to note is the difference in reconstruction approach for many of these computational imaging examples. In the case of photography where large datasets are readily available and the aim is to create an aesthetically pleasing image, deep learning has been widely implemented. In scientific imaging cases however, limited training datasets are available and the aim is to gain new insights about the sample. In such cases a physics-based reconstruction approach is more widely used with data-driven priors to improve the reconstruction quality. The work in this thesis is focused on the latter approach due to limited data. We build prototypes of imaging systems that can be further developed to product larger datasets for training faster reconstructions algorithms.

1.2 Our Toolbox

We now look at some of the components in our toolbox that are used across the projects in this thesis.

Compressed Sensing

Compressed sensing is a signal processing for acquiring and reconstructing a signal (such as a hyperspectral datacube) from limited measurements or samples far below the Nqyuist limit. It exploits sparsity inherent in the signal of interest to find the correct solution to the underdetermined problem.

Compressed sensing requires two aspects to work. The first is sparsity in the signal of interest. The second is incoherence, or low mutual coherence, in the sensing matrix. This sensing matrix in our case is the image formation matrxix $\mathbf{A}$. Mutual coherence is given by the maximum absolute value of the normalized inner product between any two different columns of the marix (Equation 2.3.1 from Wright & Ma [65]):

$$\mu(\mathbf{A}) = \max_{i \neq j} \left| \left\langle \frac{\mathbf{a}_i}{||\mathbf{a}_i||_2}, \frac{\mathbf{a}_j}{||\mathbf{a}_j||_2} \right\rangle \right| \tag{1.13}$$

The lower the mutual coherence in the $\mathbf{A}$ matrix, the denser $\mathbf{v}$ can be and still be recovered successfully. This is represented in the relation from Theorem 3.3 of Wright & Ma [65]:

$$||\mathbf{v_o}||_0 \leq \frac{1}{2\mu(\mathbf{A})} \tag{1.14}$$

where $\mathbf{v_o}$ is the unique optimal solution to the problem:

$$\min ||\mathbf{v}||_1 \quad \text{subject to} \quad \mathbf{b} = \mathbf{A}\mathbf{v} \tag{1.15}$$

Note that if $\mathbf{v_o}$ isn't intrinsically sparse in the native domain, we can apply a matrix operation, ex: $\mathbf{D}\mathbf{v_o}$, to transform it to a domain where the coefficients are sparse (ex:

gradient, Fourier, wavelet, etc). The sensing matrix would have to be adjusted accordingly and still meet the incohoerence requirement: $\mathbf{A'} = \mathbf{AD^{-1}}$. This Section 3.2 of Reference [65] for further discussion.

Random Optics: Diffusers

Chapter 3 exploit diffusers to act as randomizing optics. Rather than forming a one to one map from object space v to measurement space b, a diffuser creates a one to many mapping. The light is spread out from each point in v across multiple pixels on the sensor, a.k.a multiplexed. Then if we subsample the pixels on the sensor, the remaining subset of pixels still contain information from most of the voxels in the scene. Wright & Ma goes on to discuss how a random A matrix is actually the most optimal.[3]

The point spread function of a diffuser used as a refractive element as in Chapter 3 is a pseudo-random caustic pattern. The diffuser can be thought of as as multiple lenslets with some average focal length. The sensor is placed at the focal plane of the diffuser.

In contrast in Chapter 2, we shine a plane wave incident on the diffuser and sense the field farther away than in the refractive cause. The random phase variations from a thin diffuser creates a speckle pattern in the far field. This speckle pattern is also a pseudo-random pattern that changes with wavelength. However, we aim to do denoising instead of sparse recovery for that application.

Speckle Optics

Gratings and prisms are the most basic element for obtaining spectral dispersion, or separation of wavelengths in a light field. However they don't achieve the low coherence multiplexing that's desirable for computational imaging. The diffuser also acts as a dispersive element but with wavelength dependent speckle pattern that decorrelates quickly. In Chapter 2 we experimentally measure the speckle pattern for each wavelength during calibration. Here we use light propagation methods to understand how the speckle pattern is affected by wavelength and diffuser features.

If a monochromatic plane wave is normally incident on the diffuser with refractive index n and height profile $d(x, y)$, the field directly after is equal to:

$$U_1(x, y, z = 0, \lambda) = A_0 e^{i(\frac{2\pi n}{\lambda} d(x,y))} \tag{1.16}$$

Additionally, the free space propagation kernel varies with wavelength since the same distance induces different amount of phase delay depending on the wavelength. The field after propagating a distance z under the paraxial approximation is given by the Fresnel kernel $h(x, y, z, \lambda)$:

[3]Here by random, we mean that the relationship is still deterministic, but lacks noticeable structure.

$$U_2(x,y) = U_1(x,y,0,\lambda) * h(x,y,z,\lambda) = U_1(x,y,0,\lambda) * \frac{e^{i\frac{2\pi}{\lambda}z}}{i\lambda z} e^{(i\frac{\pi}{\lambda z}(x^2+y^2))} \tag{1.17}$$

This calculation is typically done in Fourier space using Angular Spectrum Method and involves taking the Fourier transform of U_1 along x and y which we'll represent via $\tilde{U_1}$:

$$\tilde{U_1}(k_x,k_y) = \int_{-\infty}^{\infty}\int_{-\infty}^{\infty} U_1(x,y)e^{-i(k_x x+k_y y)}dxdy \tag{1.18}$$

The field is given by:

$$\tilde{U_2}(k_x,k_y,z,\lambda) = \tilde{U_1}(k_x,k_y,0,\lambda)\tilde{H}(k_x,k_y,z,\lambda) = \tilde{U_1}(k_x,k_y,z,\lambda)e^{ik_z z} \tag{1.19}$$

where $k_z = (\frac{2\pi}{\lambda} - k_x^2 - k_y^2)^{1/2}$. The transfer function $\tilde{H}$ essentially oscillates the amplitude of each plane wave based on its spatial frequency component along z. Note that $\tilde{H}$ is also a function of wavelength λ. Thus, even for a fixed length z, it will act differently for different wavelengths. And so even for a thin diffuser where the phase delay differences between wavelengths are negligible, the propagation will result in drastically different final fields.

We take the inverse Fourier transform of $\tilde{U_2}$ and take the superposition of all wavelength components to get the resulting field on the sensor:

$$I(x,y,z) = \sum_{\lambda} |F^{-1}(\tilde{U_2}(k_x,k_y,z,\lambda)) \tag{1.20}$$

This image formation model was used to simulate the diffraction from a diffuser and understand the effects of wavelength.

We follow the analysis in Chapter 5 and 6 of *Speckle Phenomenon in Optics* [22] to further understand the speckle pattern. If we assume a random surface $d(x,y)$ with a uniform distribution of heights, then the autocorrelation of the speckle field, $\Gamma_A(\Delta x, \Delta y)$ is approximately given by the Fourier transform of the 2D intensity right after the surface $I(x',y')$ (Eq. 5.7 adapted from [22]):

$$\Gamma_A(\Delta x,\Delta y) = \frac{\kappa}{\lambda^2 z^2}\int_{-\infty}^{\infty}\int_{-\infty}^{\infty} I(x',y')e^{ikz(x'\Delta x + y'\Delta y)}dx'dy' \tag{1.21}$$

The autocorrelation of the intensity is closely related to the autocorrelation of the speckle field:

$$\Gamma_I(\Delta x,\Delta y) = \bar{I}^2[1 + |\Gamma_A(\Delta_x,\Delta_y)/\Gamma_A(0,0)|^2] \tag{1.22}$$

The speckle size as measured by correlation area A_c is given by:

$$A_c = \lambda/\Omega^2 \tag{1.23}$$

where Ω is the solid angle subtended by the scattering spot. This scattering spot can be up to the size of the diffuser.

Thus we want uniform or broad illumination onto the surface to get the sharpest autocorrelation.

The autocorrelation roll off with wavelength, and hence obtainable spectral resolution, also improves with the following:

- larger amplitude of the diffuser height variations and smaller features, both with result in higher standard deviation of the height.
- larger incident beam on the diffuser
- longer propagation distance z
- smaller central wavelength $\bar{\lambda}$

For more info see References *Optics* [29] and *Intro to Fourier Optics* Goodman2005-zu and *Speckle Phenomenon in Optics* [22]. Reference [16] has code for Angular Spectrum Method.

Spectral Filter Arrays

In Chapter 3 and 4 , we rely on optical coatings to filter broadband light into the specified wavelength. Advances in optical coating and photoresist-based lithography allow the patterning of multiple dielectric stacks with overlapping boundaries resulting in a spectral filter array. [42]

Computational tools

GPU accelerated compute has reduced the reconstruction time significantly (3-10x). Autodifferentiation in Pytorch and Jax allows us to compute gradients of our object estimates with respect to the loss function. We also used machine learning tools like Weights and Biases which are useful for tracking the hyperparameters and results of the experiments.

1.3 Imaging modalities

We now discuss the light-matter phenomenon and imaging modalities that the following chapters adapt to hyperspectral imaging systems.

Optical Coherence Tomography

Optical coherence tomography (OCT) helps penetrate into biological tissue to image the structure several hundreds of microns deep. It is commonplace now for eye imaging and diagnostics with several commercial systems on the market (ex: Zeiss). OCT works based on the principles of a Michelson interferometer as shown in Figure 1.5

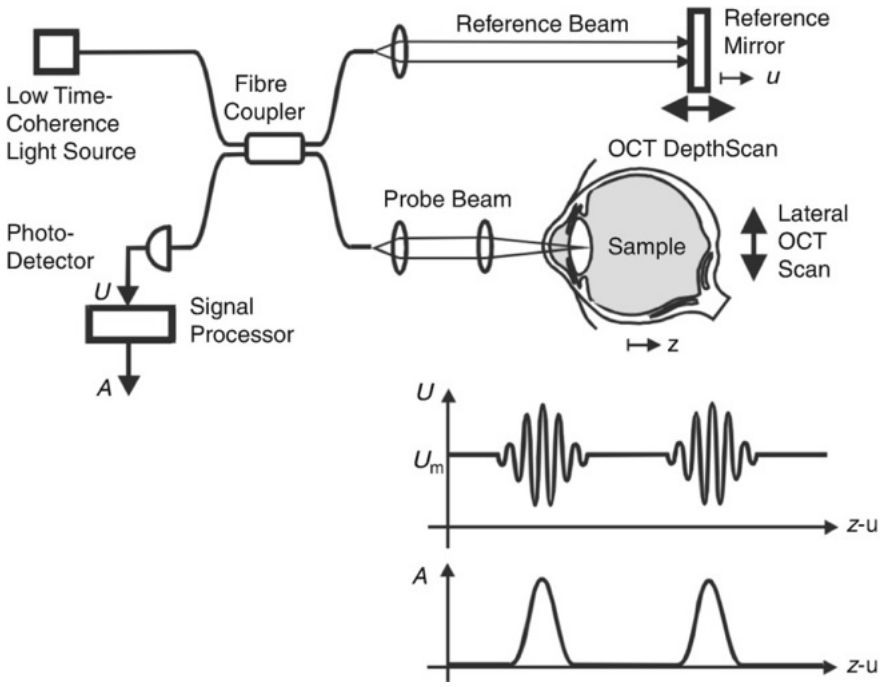

Figure 1.5: Optical setup for time-domain Optical coherence tomography. A fiber coupler is used in place of a beam-splitter to split the light source into the reference and probe (sample) beams. The combined light is captured via a photodetector. On the bottom, we see the detected and processed signal conveying depth vs reflectance information. Figure from Reference [15]

Light from a source is split into two paths using a beam splitter: one path goes to a reference mirror which reflects the light. The other path goes to the sample, which may consist of single or multiple layers of material. Light reflects off the interfaces in the sample back towards the beam splitter. Here it interferes with the reference light from the mirror. The optical path difference between the sample and reference beams determines whether light is constructively or destructively interfering. The interference spectrum is captured on a detector. OCT uses light with low temporal coherence, meaning it is made up of multiple wavelengths. The advantage of this is that all the wavelengths will only constructively interfere when the reference path matches the sample path length exactly (as opposed to constructive interference at every multiple of the wavelength difference in path length). This helps with optical sectioning, as light only at a specific depth is captured on the sensor. The reference mirror is scanned in z to capture the signal from all depths in the sample. This scheme is called time-domain optical coherence tomography which has limitations including scan time and the need of moving parts.

Another scheme was developed to mitigate these limitations called Fourier-domain OCT which consists of swept-source OCT and spectral-domain OCT as shown in Figure 1.6. In

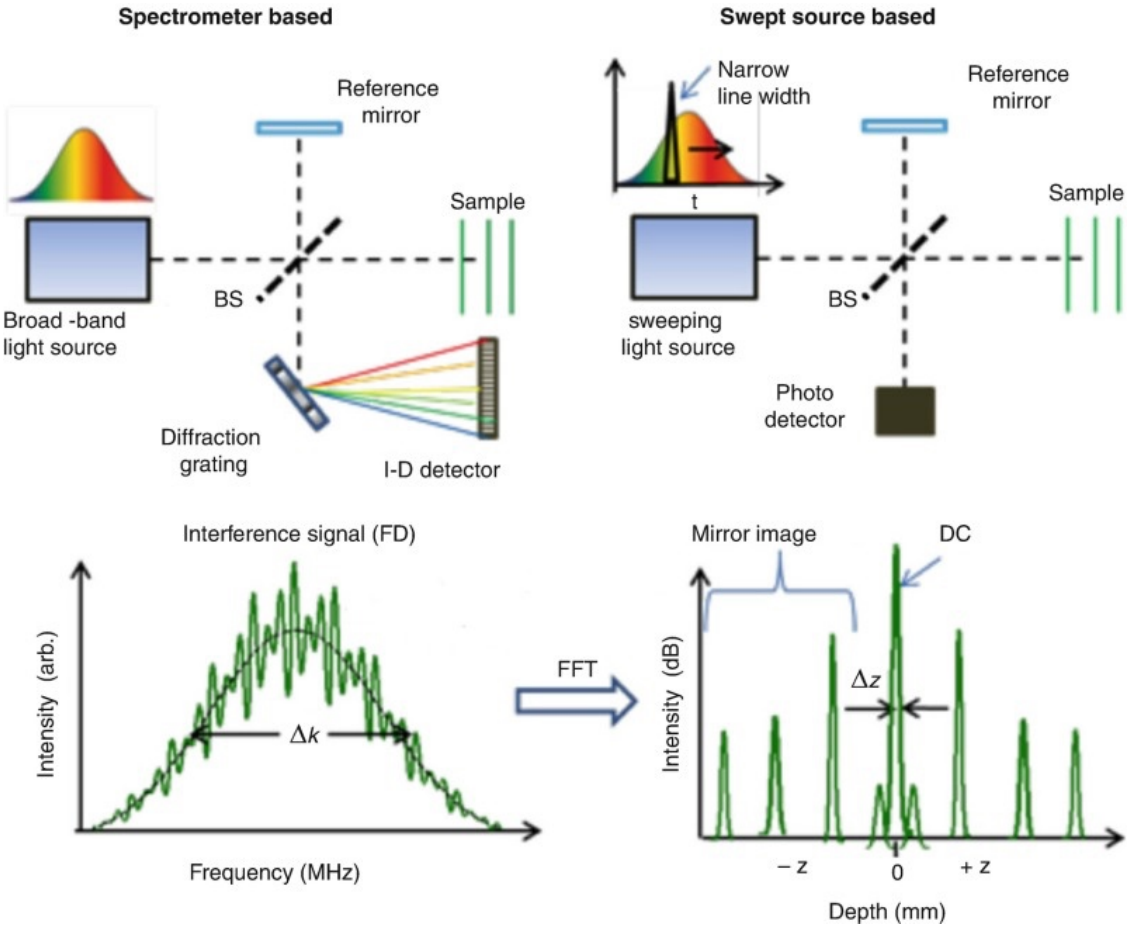

Figure 1.6: Schematics of Fourier-domain OCT systems including spectrometer based (aka spectral domain) and swept-source. The interference signal is Fourier transformed to obtain the depth vs reflectance intensity graph. Note the mirror image (due to the Fourier transform of a real signal resulting in a symmetric output) is usually ignored. Figure from Reference [11]

these cases, the spectrum of the light source is modulated by the sample and Michelson interferometer. The Fourier transform of this modulated spectrum gives us the reflectance vs depth curve as found in time-domain OCT. The final modulated spectrum is either directly measured by a spectrometer in the case of spectral-domain OCT or via a photodiode at each wavelength from a tunable laser in the case of swept-source OCT. In chapter 2, we develop a compact spectrometer for mobile or field use of spectral-domain OCT. The spectral resolution of the spectrometer dictates the imaging depth in OCT and the spectral bandwidth dictates axial resolution. Hence we aim to maintain the resolution and bandwidth of the compact computational spectrometer. For more background on OCT see References [3] [11].

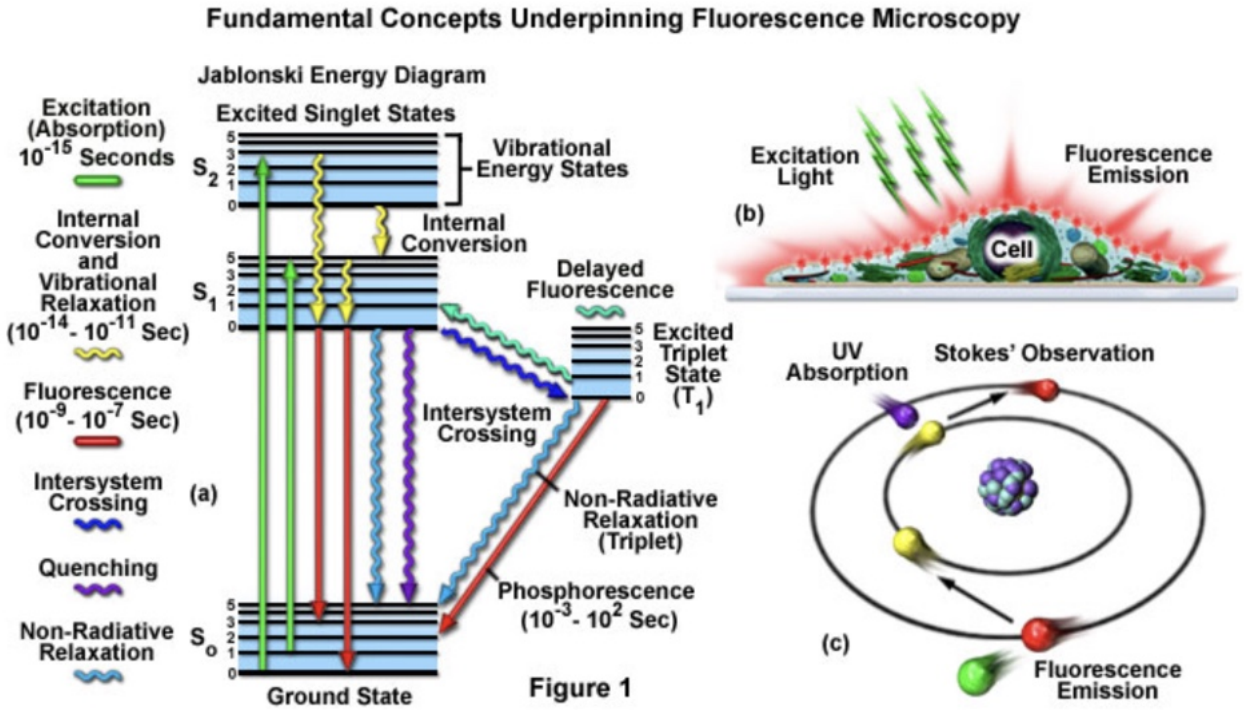

Figure 1.7: Jablonski energy diagram showing electronic transitions during fluorescence. Figure from Reference [51]

Fluorescence Microscopy

Fluorescence microscopy is a major workhorse of modern biological imaging. It allows the labeling of specific cell structures (organelles, proteins, etc) with fluorescent dyes for morphological and functional analysis of cells.

The basic principle of fluorescence relies on excitation and radiative relaxation of electrons inside a molecule. The band gap energy between the ground state and excited singlet states dictates the energy (and wavelength) of the emitted photon. Fluorescence is a spontaneous, incoherent process meaning the emitted photons have no correlation with the incident light or emission from other parts of the sample. Figure 1.7 shows the fluorescence transition (nanoseconds) in a Jablonski energy diagram. Fluorescent labels include organic dyes, quantum dots, and fluorescent proteins all of which are commonly used in cellular imaging.

In a fluorescence microscope as shown in Figure 1.8, the excitation light shines on to a sample either in epi (same side as collection objective) or trans (opposite side) configuration. The sample then emits light at a longer wavelength. A dichroic filter is used to reject the excitation light and allow the longer emission wavelengths to continue towards the sensor. Typically a bandpass filter is placed in the emission path to capture light from the intended label and reject any autofluorescence or stray excitation light. The dichroic and bandpass

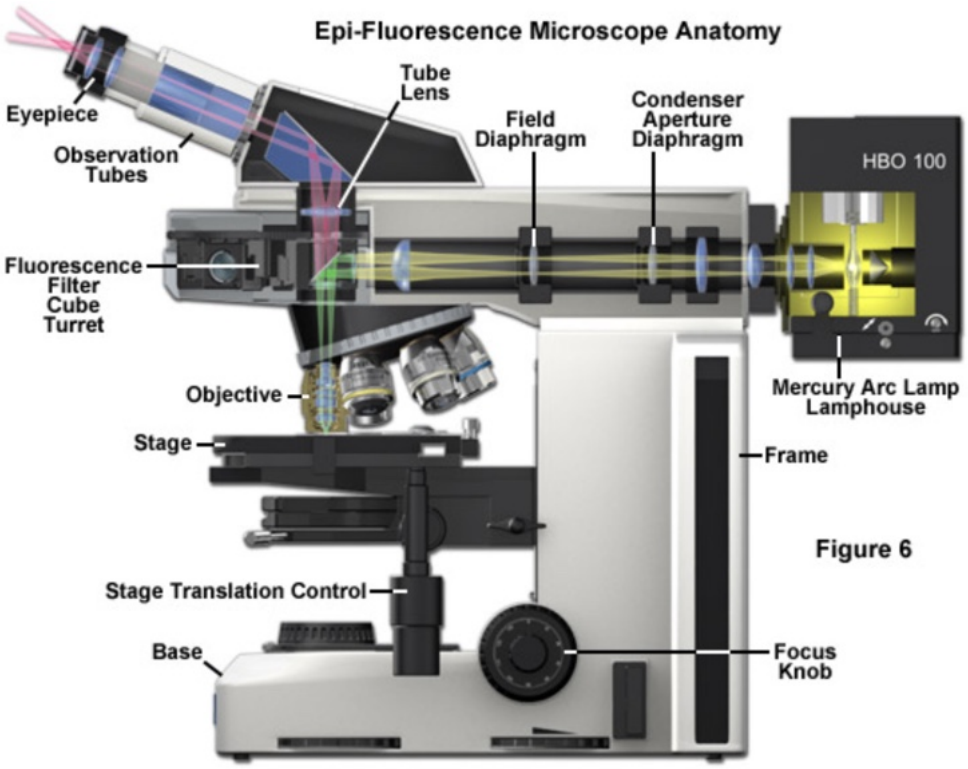

Figure 1.8: Epifluorescence upright microscope for fluorescence imaging. Figure from Reference [51]

filter are changed inside a filter wheel to obtain the emission from multiple dyes.[4] The objective and tube lens are used to focus the light from the sample onto the image plane where it is captured by a camera or eyepiece. In chapter 3, we replace the camera with the hyperspectral imager to detect the spectra from each point in the the scene while aiming to preserve the spatial resolution.

For more info on fluorescence microscopy see References [24][53].

Fourier Ptychography Microscopy

The third project improves upon Fourier Ptychography Microscopy (FPM), a synthetic aperture imaging technique which builds up the Fourier space of the object through multiple acquisitions. Applications for Fourier Ptychography include dynamic cell imaging and digital pathology.

[4]Typically fluorescence dyes have differing excitation spectra. Thus when choosing the dyes in Chapter 3 for our hyperspectral fluorescence microscopy experiments, we had to select dyes with similar excitation spectra.

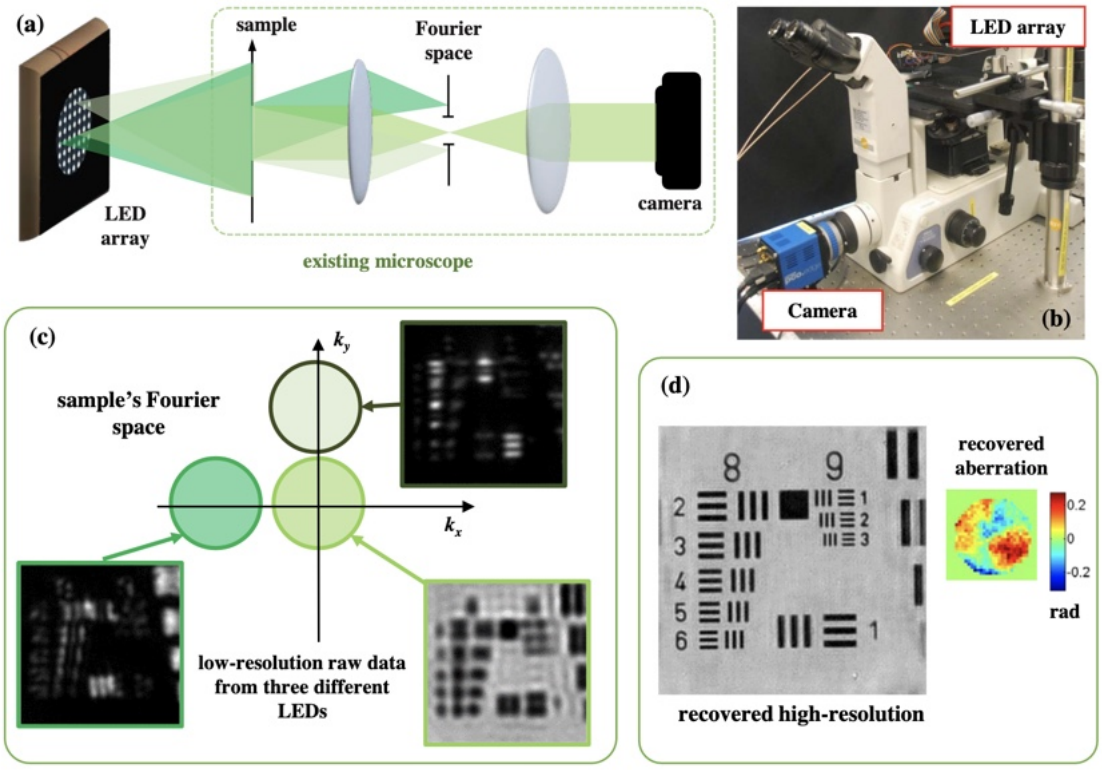

Figure 1.9: a) Fourier Ptychography Microscopy (FPM) optical diagram. b) Setup on Nikon TE300 microscope. c) Multiple low resolution images (both brightfield and darkfield) acquired using angled illumination d) Recovered high-resolution object and pupil aberration after passing raw images through the reconstruction algorithm. Figure from Reference [60]

We now build up the image formation model for single color FPM. A typical FPM setup consists of a 4-f system with an LED array for illumination as shown in Figure 1.9. The angled illumination from an off-center LED creates a phase ramp at the sample plane. This phase ramp multiplies by the sample's complex transmittance to give the following field after the sample:

$$U_1(x,y) = T(x,y)e^{i(k_{x,illum}x + k_{y,illum}y)} \tag{1.24}$$

Here, we ignore the dynamic phase factor due to time oscillations of the electromagnetic plane wave and set amplitude to 1. We also ignore any phase induced by propagation in z along the optical axis. Thus this field represents the relative phase at the sample plane with respect to the origin. This field propagates through the objective to the pupil plane which can be represented as the Fourier transform of the field after the sample:

$$U_2(k_x,k_y) = F(U_1(x,y)) = T(k_x - k_{x,illum}, k_y - k_{y,illum})P(k_x,k_y) \tag{1.25}$$

Since a phase ramp in real space corresponds to a shift in Fourier space, we are able to shift higher spatial frequencies into the pupil plane that normally would not be captured

by the low numerical aperture of the objective len as shown in Figure 1.9c. Thus the field in the pupil plane can also be written in terms of the object's Fourier space representation $T(k_x, k_y)$. The pupil function in this case would be a top hat function that allows full transmission inside the numerical aperture of the objective and zero outside.

$$P(k_x, k_y) = \begin{cases} 1 & \text{if } \sqrt{k_x^2 + k_y^2} \leq k_{pupil\_edge} \\ 0 & \text{otherwise} \end{cases} \tag{1.26}$$

The cutoff spatial frequency is: $k_{pupil_edge} = \frac{2\pi NA}{\lambda}$. For our discussion in Chapter 4, we ignore any non-idealities in the system due to aberrations, which can affect the flatness of this function. In Chapter 4, we also present a modified pupil function that incorporates the effects of a spectral filter array in the pupil plane to enable spectral FPM.

The final image is created after the light propagates through the tube lens and focuses on to the camera. This is another 2-f system and so we can model it as the inverse Fourier transform of the field at the pupil. Since cameras only measure the intensity of electric fields, we take the absolute value.

$$I(x, y) = |F^{-1}(U_2(k_x, k_y)|) = |F^{-1}(T(k_x - k_{x,illum}, k_y - k_{y,illum})P(k_x, k_y))| \tag{1.27}$$

For deeper explanation on Fourier optics, refer to Reference [21]. For more info on Fourier Ptychography see Reference [75].

1.4 Outline

We end this chapter with an outline of the rest of the thesis.

In Chapter 2, we present a compact computational spectrometer for spectral-domain optical coherence tomography. This spectrometer uses a diffuser as the dispersive element and recovers the spectrum of experimental light sources via solving a linear inverse problem.

In Chapter 3, we present a hyperspectral fluorescence microscope using a diffuser and spectral filter array to achieve higher spatial resolution than a traditional approach. We then use this microscope to image fluorescent samples such as cells and bioassay beads.

In Chapter 4, we present an approach for gigapixel hyperspectral Fourier Ptychography using a spectral filter array in the pupil plane. The reconstruction of simulated measurements is done via stitching the information from multiple low-resolution images into a high-resolution hyperspectral datacube.

Finally in Chapter 5, we present lessons learned and future work.

Chapter 2

Diffuser based speckle spectroscopy

This chapter is based on the paper: *Malone, Aggarwal, et al, "DiffuserSpec: spectroscopy with Scotch tape", Optics Letters, 2023* [36] with co-authors Joseph Malone, Laura Waller, and Audrey Bowden. We acknowledge Eric Markley for his helpful discussions and guidance.

2.1 Abstract

Computational spectroscopy breaks the inherent one-to-one spatial-to-spectral pixel mapping of traditional spectrometers by multiplexing spectral data over a given sensor region. Most computational spectrometers require components that are complex to design, fabricate, or both. DiffuserSpec is a simple computational spectrometer that uses the inherent spectral dispersion of commercially available diffusers to generate speckle patterns that are unique to each wavelength. Using Scotch tape as a diffuser, we demonstrate narrowband and broadband spectral reconstructions with 2-nm spectral resolution over an 85-nm bandwidth in the near-infrared, limited only by the bandwidth of the calibration dataset. We also investigate the effect of spatial sub-sampling of the 2D speckle pattern on resolution performance.

2.2 Introduction

Traditional spectrometers use an optical element such as a grating or prism to linearly disperse a broadband optical signal into its constituent wavelength components. The resulting one-to-one spectral-to-spatial (camera pixel) mapping simplifies measurement of the amplitudes of the underlying spectral components. A major limitation of these spectrometers, however, is the inherent trade-off between bandwidth, dispersion angle (or system footprint), and spectral resolution, which leads to bulky designs with large footprints and expensive components.

Emerging alternative spectrometer designs leverage the power of computational optics to reconstruct spectra from disordered spatial patterns in one and two dimensions [69] [9] [70].

These systems replace the one-to-one spectral-to-spatial coding of a traditional spectrometer with a spectral multiplexing element and use computational algorithms to reconstruct the spectrum of interest. Such computational spectrometers have been demonstrated using coded-apertures [63], integrated photonics [49], photonic crystal filters [30], and custom diffractive elements [64]. However, the dispersive elements used in these systems are often complex to design, fabricate, or both.

Recent computational spectrometers using speckle correlation patterns resulting from multimode fibers (MMF) [50] [33] [7], disordered alumina substrates [37], and frosted glass substrates [68] demonstrate the potential utility of off-the-shelf, low-cost components for computational spectroscopy. Here, we introduce DiffuserSpec—a simple, free-space, scattering-based computational spectrometer using an extremely low-cost diffuser: 3M Scotch Magic Tape. Tape is an exceedingly cheap, practical alternative to custom-designed optics and gratings and has been previously used for computational imaging. When illuminated, the tape produces a diffuse speckle pattern that is a function of the illumination wavelength and the tape's random refractive surface. In this work, we show that a Scotch tape diffuser can enable spectroscopy of narrowband and broadband spectra. We also examine the effect of spatial sub-sampling of the full dataset on resolution performance, as is relevant for compressed imaging. The simple, cost-effective design of DiffuserSpec highlights the potential of commercially available dispersive components to serve as new options for the construction of low-cost, compact spectrometers for scientific applications across a range of disciplines. The DiffuserSpec strategy, moreover, showcases the benefit of using computation to replace costly, sophisticated optical components.

2.3 Methods

In contrast with a traditional grating-based system [Figure 2.1(a)], DiffuserSpec [Figure 2.1(b)] takes advantage of spatial-spectral multiplexing to yield a more compact system. Its general operating principle [Figure 2.1(c)] is as follows: (1) light passes through an arbitrary dispersive element (ADE) such as Scotch tape; (2) the pattern of transmitted dispersed light, unique for each spectrum, is captured by a detector; (3) a computational reconstruction algorithm (e.g., linear inversion) maps the detected speckle pattern to the input spectrum, using data obtained during a calibration step. The calibration data, organized into what we call the spatial-spectral transfer matrix (SSTM), comprises the set of unique diffuse speckle patterns associated with each wavelength. Figures 2.1(d) and 2.1(e) show two representative speckle patterns resulting from monochromatic illumination of the DiffuserSpec with collimated light (4-mm beam diameter) at 818 nm and 828 nm set 15 mm from a Scotch tape diffuser, which was placed 50 mm from a scientific CMOS (sCMOS) sensor (PCO Edge 5.5). Figure 2.1(f) shows a color overlay of two sub-regions of the full speckle pattern that have been magnified to show the variation of the speckle distribution between the two wavelengths.

Although the detected speckle patterns appear random, they are largely deterministic. The measurement on the 2D sensor, $b(x, y)$, is approximately a weighted sum of the compo-

nents of the SSTM, $A(x, y, \lambda)$. The weights $w(\lambda)$ define the input spectrum:

$$b(x, y) = \int_{\lambda_1}^{\lambda_n} A(x, y, \lambda) w(\lambda) d\lambda \tag{2.1}$$

In the case of a finite SSTM calibrated at discrete wavelengths, this expression can be mathematically rewritten as a linear system of equations; however, a more accurate expression should include the effect of noise terms, which may arise from sources including photon shot noise in the source light, dark noise in the detector, or small perturbations or misalignments of the optics:

$$\mathbf{b} = \mathbf{A}\mathbf{w} + \mathbf{n} \tag{2.2}$$

Here, $\mathbf{b} = b(x, y)$ is a matrix containing the sensor pixel measurements, $\mathbf{w} = w(\lambda)$ is a vector that describes the input spectrum weights as applied to $\mathbf{A} = A(x, y, \lambda)$, and $\mathbf{n} = n(x, y)$ describes the noise at each pixel.

Ideally, the solution for $\mathbf{w}$ may be obtained using a simple reconstruction algorithm: the linear inverse of $\mathbf{A}$. That is, $\mathbf{w} = \mathbf{A}^{-1}\mathbf{b}$; however, the presence of noise leads to ill-conditioning and overdetermination of the system. Inverting an ill-conditioned linear system will cause any noise components along the vectors associated with small singular values to become greatly amplified. Thus, our reconstruction attempts to find the least-squares solution,

$$\hat{\mathbf{w}} = \arg \min_{w/geq0} |\mathbf{A}\mathbf{w} - \mathbf{b}|_2^2 \tag{2.3}$$

using a low-rank inverse:

$$\hat{\mathbf{w}} = \hat{\mathbf{A}}^{-1}\mathbf{b} \tag{2.4}$$

We compute $\hat{\mathbf{A}}^{-1}$ by performing the singular value decomposition (SVD) of A, inverting its singular values, and using a filter to attenuate the inverted singular values that exceed an empirically determined threshold:

$$\hat{\mathbf{A}}^{-1} = \mathbf{V}(F_\sigma(\mathbf{\Sigma}^{-1}))\mathbf{U}^T \tag{2.5}$$

Here, $\mathbf{\Sigma}$ is a diagonal matrix containing the singular values of $\mathbf{A}$ from largest to smallest, and $\mathbf{U}$ and $\mathbf{V}$ contain the corresponding singular vectors. Additionally, F_σ represents the filter on the inverted singular values. For our implementation, we used a half-Gaussian filter to smooth the inverted singular values with a tuning parameter, σ, corresponding to the Gaussian filter width. The value of σ used affects the noisiness and performance of the reconstruction and was chosen empirically to minimize error between the ground truth and DiffuserSpec spectra. Additionally, we enforced a non-negativity condition to the reconstructions by setting negative values to 0. Overall, this method is similar to the truncated SVD algorithm, which used a hard threshold on the singular values. We found that applying a hard threshold caused ripple artifacts in the reconstructed spectrum that a smoother (Gaussian) filter avoided.

To demonstrate the use of DiffuserSpec for spectroscopy, we first measured **A** for our ADE, Scotch tape, during a calibration step using a broadband superluminescent diode (SLD) source (Superlum, Broadlighter) connected to a custom-built monochromator with a spectral resolution of 0.1 nm. A 90:10 fiber coupler was used to simultaneously direct light from the monochromator to both the DiffuserSpec and a commercial spectrometer (Thorlabs, CCS175). In this way, we could obtain the ground-truth spectrum associated with each speckle pattern. We developed automated software in LabView to expedite the calibration procedure. We then collected an SSTM comprising an average of 10 frames (75-ms each) at each of 344 monochromatic wavelengths spanning 784.7-870.4 nm (0.25-nm step size). The sampling density was chosen based on preliminary measurements we carried out to ensure the spectral resolution of the DiffuserSpec was limited by the spectral dispersion of the ADE rather than the calibration matrix. To account for power differences associated with different wavelengths from the monochromator, the speckle pattern for each wavelength was normalized to have an equal total intensity. The normalization was used to remove the influence of the intensity profile of the calibration source on future reconstructions.

Using the full 3D SSTM (2560 pix by 2160 pix by 344 frames) for reconstruction by SVD resulted in an overdetermined inverse problem and required excessive computational resources. Hence, we reduced the dimensionality of the problem by sampling a subset of the pixels from each frame prior to computing **A** to yield a 2D SSTM of size P x S, where P is the number of pixels in the subset and S is the number of calibration frames. The SSTM and the sensor measurement, **b** (size P x 1, sub-sampled at the same pixels as used for **A**), were then used to determine **w** by solving the inverse problem. Note that while the reconstruction algorithm is agnostic to the order of vectorized pixel data within the SSTM, the subset of pixels used is highly relevant for determining the quality of the reconstruction, as we will discuss later.

2.4 Results

Figure 2.2(a) shows representative reconstruction results for six narrowband spectra overlaid on the same graph. The wavelengths used for reconstruction were not included in the SSTM, which was down-sampled by omitting every evenly indexed spectral column (i.e., S=172). That is, the wavelengths used for **b** in the inverse problem were selected from the omitted spectral data. In this example, **A** and **b** were sub-sampled by selecting a random distribution of P=40,000 pixels from the full 2650 x 2160 SSTM frame, resulting in a 2D SSTM sized 40,000 x 172 (spatial x spectral) pixels. DiffuserSpec is able to reconstruct the individual wavelength peaks across a broad bandwidth with good resolution, although the full width at half maximum resolution of the reconstructed peaks is worse than the resolution of the monochromator (1.25 nm versus 0.1 nm). We then tested the ability of DiffuserSpec to reconstruct a two-peak spectrum by collecting speckle patterns from two monochromatic peaks sequentially and averaging them together. Simulating data in this way is reasonable because light at two different wavelengths does not interfere; hence, the intensity patterns

can be added. Figure 2.2(b) shows that the reconstruction can resolve a 2-nm separation.

Similar to other work in computational spectroscopy, we proffer that the performance of a given ADE for spectroscopy is related to the spectral correlation of the wavelength-dependent speckle patterns it generates. Specifically, the spectral correlation function, C, can be used to assess the degree of correlation between the speckle patterns associated with two wavelengths separated by a difference $\delta\lambda$ (i.e., a spectral shift) [50]:

$$C(p, \delta\lambda) = \frac{< \mathbf{A}(p, \lambda) * \mathbf{A}(p, \lambda + \delta\lambda) >}{[< A(p, \lambda) >< A(p, \lambda + \delta\lambda) >]} - 1 \tag{2.6}$$

Here, p represents the pixel used for the calculation, A is the intensity of light measured at pixel p, and ¡.¿ represents a mean operator over wavelength. Typically, the value $C(\delta\lambda)$ is obtained by averaging $C(p, \delta\lambda)$ across all pixels used in the reconstruction. The resulting plot may then be used to estimate the spectral resolution, λ_{res}, which we define as the spectral shift at which $C(\delta\lambda)$ drops to half of its maximum value. For the data used in Figure 2(b), this value was 2 nm and is consistent with our ability to resolve the two peaks. Notably, the resolution of the two-peak reconstruction differs from that of single-peak reconstructions.

As stated previously, the full 3D SSTM contains a large amount of data, which can place a significant computational burden on performing the reconstruction. One solution to this problem is to reduce the amount of total data by using only a subset of P pixels in each frame, but the choice of which subset of pixels to use will affect the spectrometer performance. To investigate the impact of pixel choice on resolution performance, we analyzed the effects of different pixel regions on the resulting spectral correlations and the resolution of the reconstructions.

Figure 2.3(a) shows a visual representation of λ_{res} for each individual pixel in the sensor array, which relates to the contribution of a given pixel to the resolution of the final reconstruction. Here, the raw 2D heatmap has been smoothed (using a 50-pixel Gaussian filter) to illustrate the general trend: pixels near the edge of the field-of-view (FOV) show more spectral decorrelation than pixels near the center, which suggests that reconstructions that include pixels from edge regions should be capable of achieving higher resolution. This trend makes intuitive sense because the spectral dispersion of the light reaching the outer edges of the FOV is more significant than that of light toward the central FOV, similar to higher orders of a grating. Figure 2.3(b) plots the resolution versus lateral dispersion angle taken from the dotted white line in Figure 2.3(a). The FWHM (2.35°) is a measure of the angular spectral dispersion, which is characteristic for a given diffuser and is a measure of its utility for spectroscopy.

To illustrate the impact of pixel choice on the reconstruction, we designed three binary masks to select for pixels associated with low or high values of λ_{res}. To control for the number of pixels used in the reconstruction, we randomly sampled the same number (P = 40,000) of pixels from the white region of each mask. The choice of 40,000 (0.7% of the data) represents a balance of computational ease and sufficiently high sampling density to produce similar reconstruction patterns over multiple iterations of random selection (i.e., an error within the noise floor).

Figure 2.3(c) shows the spectral correlation plots generated by applying Equation (6) to the pixel subsets extracted from each mask [Figure 2.3(c) insets] and normalizing to the maximum value of C in each case. The black "x" at 0.5 indicates the half-maximum value used to determine λ_{res}, or the estimated resolution for that pixel subset. As expected, λ_{res} is significantly better (smaller) when using pixels from the "outer" parts of the FOV rather than the "inner" parts of the FOV (λ_{res} = 2.1 nm versus 5 nm). The resolution is even better (λ_{res} = 1.55 nm) when selecting pixels from the "corners" of the FOV. These results make sense because Equation (6) is merely an average of the values of $C(\delta\lambda)$ for all pixels in the subset. The single-peak reconstructions in Figure 2.3(d) corroborate this trend, suggesting that the resolution of the resulting reconstruction depends on which pixels are used. Notably, the actual FWHM resolution of the single peak is better than the prediction from C [1.23 nm (corners), 1.4 nm (outer circle), and 2.03 nm (inner circle)], suggesting that λ_{res} is not synonymous with the resolution; as with other computational spectrometers, the reconstruction performance is also a function of the algorithm and other parameters used (e.g., σ).

To explore the ability of the DiffuserSpec to reconstruct broadband spectra, we analyzed two signals. The first was a modulated version of the source spectrum created by placing a physical mask in the optical path of the monochrometer, and the second was the spectrum of a broadband SLD source (Inphenix) (λ_0 850 nm, λ_{FWHM} 45 nm). Figure 2.4 shows the ground-truth and DiffuserSpec spectra for each case using the "corners" mask sampling pattern from Figure 2.3. Each reconstruction has been normalized to its maximum value.

In Figure 2.4(a), the reconstruction shows good correlation with the two peaks at 824 nm and 840 nm. For Figure 2.4(b), the noise floor is higher for the reconstructed spectrum, and its intensity shows a sharp increase at the tail end of the calibration bandwidth, near 870 nm. We suspect that the bandwidth mismatch between the calibration range and spectral range of the source may be a contributing factor to this error. Since the SSTM and reconstruction algorithm cannot extrapolate data for wavelengths longer than 870 nm, the algorithm attributes these wavelength intensities to the next closest value within the calibration. In essence, non-calibrated wavelength information can be understood as components of the noise term presented in Equation (2), which increase the uncertainty and error of the inverse solution. It is possible that these errors may be minimized using a more sophisticated reconstruction algorithm. The difference in the noise floor between the ground truth and the reconstructed spectrum may be derived from the noise characteristic of the source itself: as the source used was different from the source used to generate the SSTM for the reconstruction, it is likely the noise floor of the SSTM depends on the source used. Overall, these results suggest that DiffuserSpec can reconstruct broadband data, and that the reconstruction depends as well on the calibration range and the noise level of the calibration dataset.

2.5 Conclusion

In this work, we have demonstrated the use of Scotch tape as the dispersive component in a simple computational spectrometer able to reconstruct narrow and broadband spectra with better resolution than other works that leverage coded-aperture detection (3.6 nm) [63], custom diffractive elements (2 nm) [64], and frosted glass (4.25 nm) [68]. The DiffuserSpec strategy can be implemented for any ADE, and our analysis can be generalized to determine the expected resolution and performance of any ADE. Some advantages of DiffuserSpec over traditional spectrometers include: (1) ADEs can be obtained at extremely low cost; (2) the system bandwidth can be tuned by changing the calibration dataset and not the system footprint, enabling compact designs with broadband performance.

Although the DiffuserSpec is insensitive to alignment during setup, the resulting reconstruction is highly sensitive to the SSTM obtained during calibration; hence, the input source, ADE, and sensor should ideally be rigidly attached. We have observed that the alignment is sufficiently stable to enable use of the same SSTM to accurately reconstruct desired spectra over multiple days (data not shown). Given that speckle contrast is the key to good performance, one should expect to achieve better performance when the wavelengths of interest are well separated, providing an opportunity to multiplex other information (e.g., spatial, polarization). It is also possible that changes to the optical setup may improve the performance, such as angling the detector or pixel binning. In conclusion, DiffuserSpec provides a simple way to make computational spectroscopy more accessible and versatile to general research and commercial communities.

Data and code available in Reference [6].

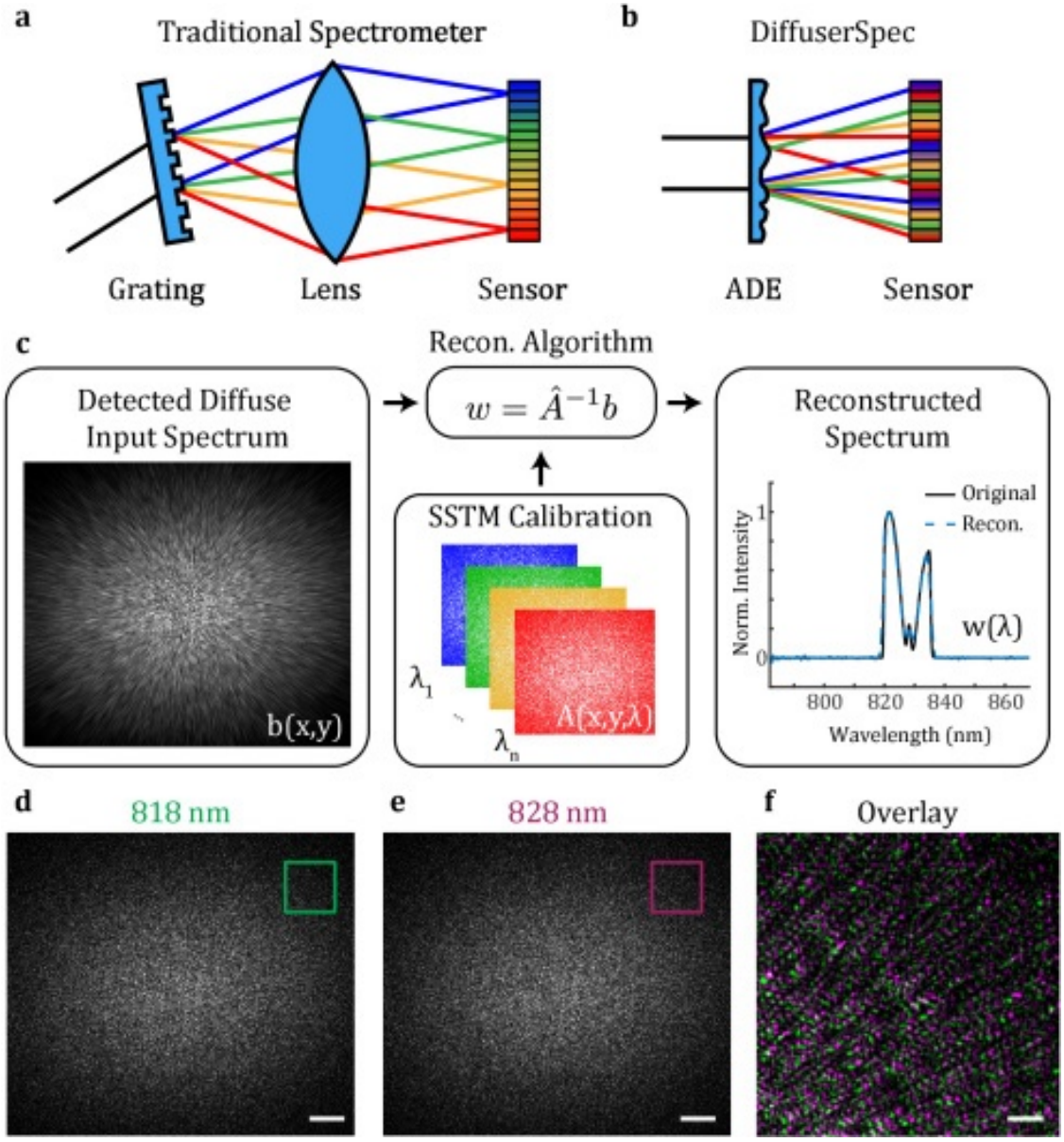

Figure 2.1: Schematic representation of (a) a traditional spectrometer and (b) the DiffuserSpec computational spectrometer. (c) Simplified flow diagram of DiffuserSpec's operating principle. Representative speckle patterns from (d) 818 nm and (e) 828 nm. Scale bar is 1.66 mm. (f) Color overlay of the sub-regions in panels (d) and (e) shows the speckle pattern changes with wavelength. Scale bar is 0.230 mm. ADE, arbitrary dispersive element (Scotch tape).

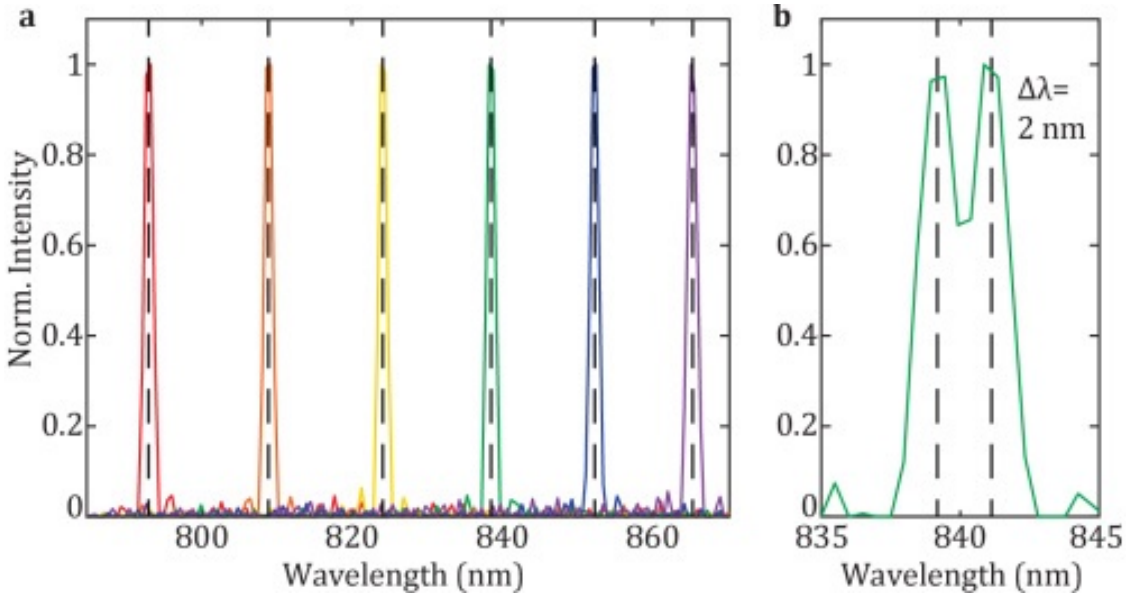

Figure 2.2: (a) Reconstruction of six narrowband spectral peaks acquired separately, where the black, dashed lines correspond to the illumination wavelengths. (b) Two-peak reconstruction of a 2-nm separation measured using the same SSTM data. For both, $\sigma = 250$ pix.

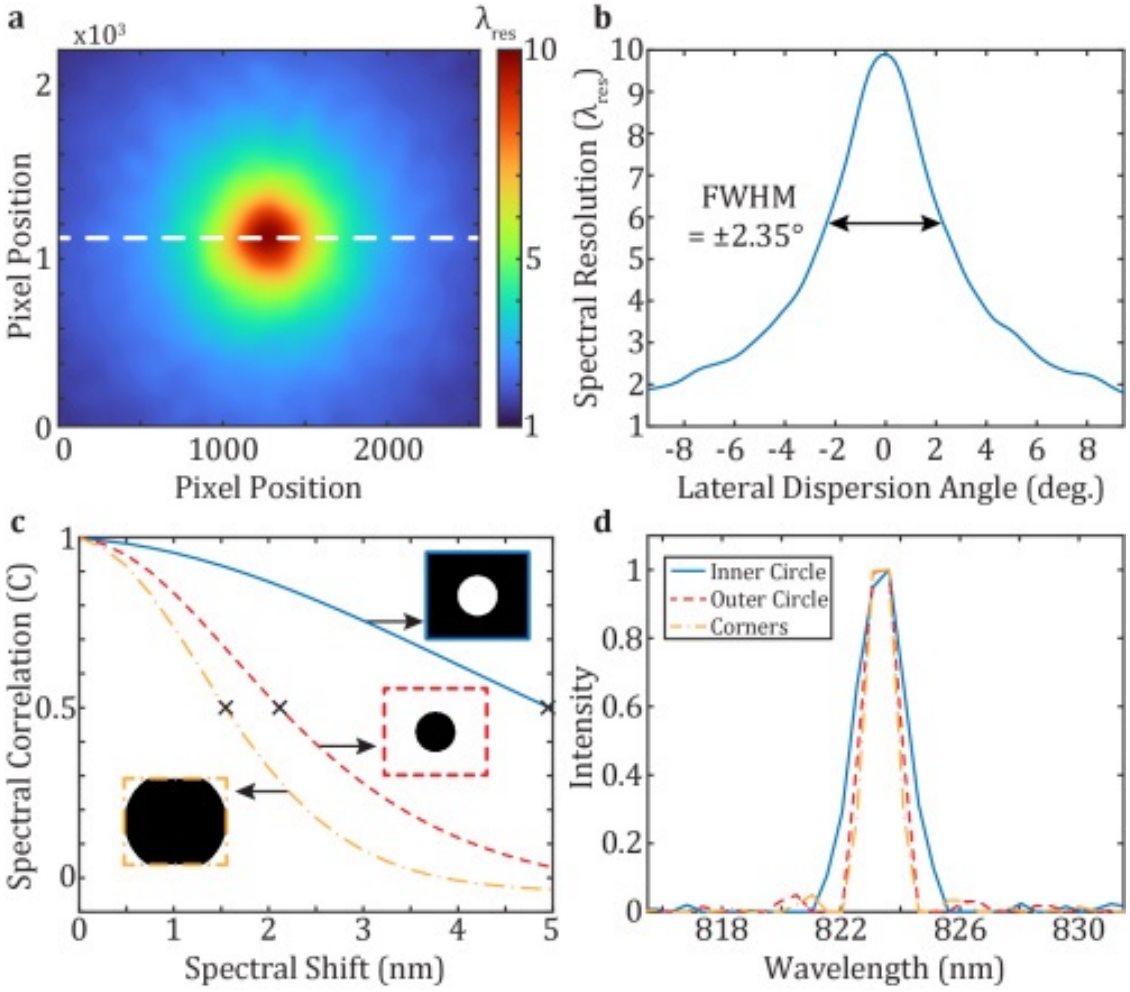

Figure 2.3: (a) Value of λ_{res} versus pixel position. (b) Value of λ_{res} versus dispersion angle. (c) Normalized spectral correlation function for different sampling masks, shown as insets. Sampled pixels were chosen randomly from within the white areas. The black "x" identifies λ_{res}. (d) Normalized single-peak reconstructions for each sampling scheme (σ = 250 pix).

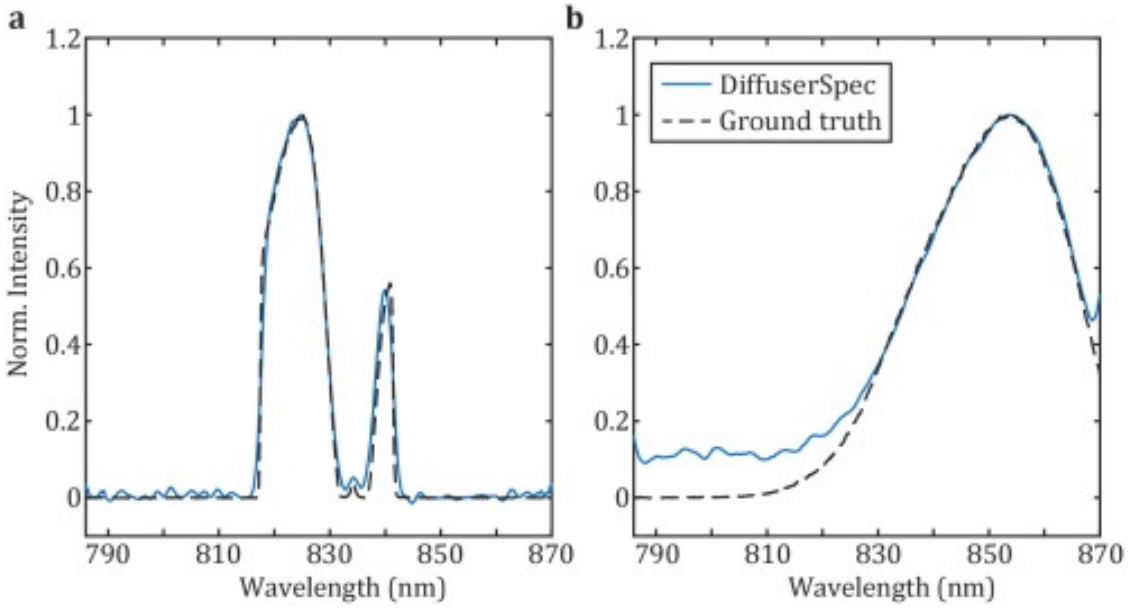

Figure 2.4: Broadband spectral reconstruction with a Scotch tape diffuser. Ground truth (solid blue) spectrum and DiffuserSpec (dashed black) reconstruction of (a) a modulated version of the source spectrum and (b) an alternate SLD source by InPhenix. Here, $\sigma = 20$ pix.

Chapter 3

Compact hyperspectral imager for fluorescence microscopy

3.1 Abstract

Hyperspectral fluorescence microscopy enables important biological and clinical applications, but conventional systems are bulky or require scanning, limiting temporal resolution and throughput. We introduce a computational snapshot hyperspectral microscope that uses compressed sensing to achieve higher spatial-spectral resolution than traditional snapshot systems. Our device is compact ($\sim$ 15 cm $\times$ 6 cm $\times$ 6 cm) and easily attaches to standard fluorescence microscopes. We benchmark our system against existing snapshot methods through simulations to evaluate its spatial and spectral performance. Experimental imaging of fluorescent beads, labeled cells, and lanthanide hydrogel beads demonstrates a practical, high-throughput solution for hyperspectral microscopy in biological and clinical applications.

3.2 Introduction

Hyperspectral microscopy aims to capture a high-resolution spectrum for each point across space in a microscopy sample. A snapshot hyperspectral microscope has the advantage of acquiring the entire datacube in a single acquisition which can improve imaging throughput or enable dynamic imaging. Hyperspectral imaging has many applications in fluorescence microscopy, including cellular imaging and bead-based bioassays. Hyperspectral microscopy enables linear unmixing of dozens of fluorophores allowing denser labeling of cell structures [38] which is useful for genomic phenotype screens [55]. It also provides higher dimensional datasets for label-free modalities such as autofluorescence imaging of cells [40]. High-content cell imaging systems aim to capture quantitative data from cellular images at high-throughput and traditionally use multichannel fluorescence [72]. Hyperspectral microscopy has the potential to enhance high-content imaging by providing richer datasets [61]. Bead based bioassays use small fluorescent beads to detect and quantify small molecules

like nucleic acids or porteins. Hyperspectral microscopy allows simultaneous detection and differentiation of multiple bead types based on their spectral signatures, enabling highly multiplexed assays [71, 14, 41, 18]. In the work by Feng *et al.*, they used a basis of six different spectra to create ratiometric lanthanide hydrogel beads that required six emission channels for identification. Hyperspectral microscopy can enable the identification of even more codes, further increasing throughput.

Most imaging systems collect a hyperspectral datacube by scanning through space or spectra. For example, in a pushbroom system, a single line in the object is dispersed using a grating onto a 2D sensor. The object is slowly scanned through the narrow imaging field-of-view to generate a datacube. Or a tunable spectral filter can be placed before the camera to scan through wavelength channels. In both cases, multiple images must be acquired to generate a hyperspectral datacube, requiring long acquisition times per sample. This is a major limitation for data-driven approaches in biology, where the ability to capture large, high-quality datasets is increasingly essential. As machine learning continues to advance, the need for fast, scalable methods for hyperspectral data acquisition becomes more important.

Snapshot hyperspectral imagers can capture the whole hypercube in one exposure, potentially speeding up the acquisition time. Several research systems demonstrate snapshot fluorescence microscopy, as summarized in Table **??**. These systems use either filters which allow customizable channel selection or dispersive prisms which improve light throughput to separate out the wavelength channels. For example, the systems in [31], [44], and [74] all use prisms to disperse the image along a single direction, allowing them to capture live cell imaging. However, these systems are large setups with limited spectral channels. Wu *et al.* uses a multi-camera array with a different color filter on each camera to obtain volumetric multispectral imaging [66]. The number of cameras scales linearly with spectral channels leading to a larger, expensive setup. We build on this previous work for a more compact and accessible system using a filter array. Previous work has also used compressed sensing to recover a 3D datacube from a 2D measurement. For example, the coded aperture snapshot spectral imaging system captures the full spectral datacube by using a prism to disperse the different wavelengths and an aperture to code the information onto a 2D sensor [10]. Inspired by this, we present a different compressed sensing approach using a diffuser for multiplexing.

In this paper we present a new computational snapshot hyperspectral microscopy system. This compact imager can easily integrated with existing benchtop epifluorescent microscopes. Our imager is an extension of our previous work in hyperspectral photography [39], consisting of only three components that can be attached to the output port of any benchtop fluorescent microscope. Notably, our system reconstructs a hyperspectral datacube with more voxels than pixels on our 2D sensor, by using compressed sensing approaches. This improves the spatial resolution by $\sim 3\times$ compared to traditional filter array-based snapshot microscopy. Our current filter has 64 spectral bands (8 nm resolution) in the visible, near-infrared range that can be expanded and tailored to specific applications in the future. We open source both the hardware design and reconstruction software to facilitate adoption and further development. Our experiments with fluorescent beads, as those used in bioassays, show accurate spatial and spectral reconstructions. Finally, we discuss this system's main

limitations (signal strength and reconstruction quality) and possible ways to overcome them.

3.3 Methods

Our imaging architecture employs multiplexing and compressed sensing to reconstruct a hyperspectral data cube from a single sensor measurement. Compressive sensing encodes a high-dimensional scene into the 2D measurement intelligently, enabling accurate recovery of the full datacube with significantly fewer samples than traditional approaches. To achieve this, our system leverages a large point spread function (PSF) with sharp caustic features, mapping each point in the sample to multiple points on the sensor. This design ensures complete spectral sampling at every spatial location while preserving high-frequency details, allowing for high spatial and spectral resolution.

The compact optical setup (Figure **??**) integrates easily with a standard benchtop fluorescence microscopes. Emission light from illuminated samples is directed through the microscope's objective and into the hyperspectral imager, which attaches to the sideport. Measuring approximately 15 cm × 5 cm × 5 cm, the imager is easily aligned using a standard sideport adapter (Figure **??**a). This architecture builds upon our prior work with the Spectral DiffuserCam [39], incorporating a relay lens improves single throughput by closer matching the size of the Fourier plane to the diffuser aperture and simplifying integration with existing fluorescent microscopes.

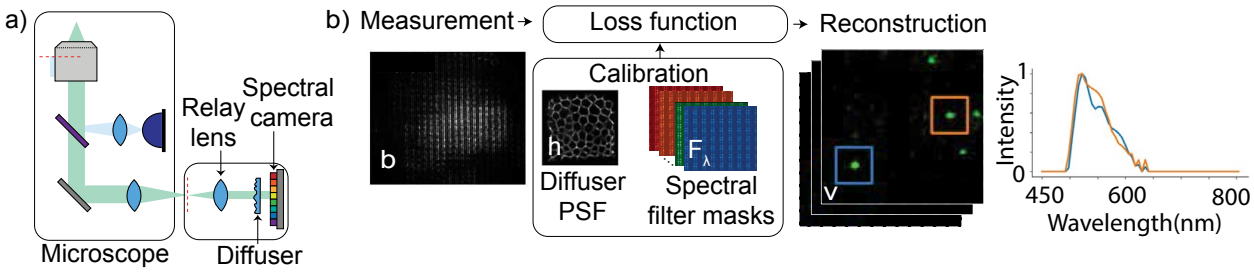

Figure 3.1: a) Our snapshot hyperspectral microscope consists of a relay lens, diffuser and spectral sensor placed at the output port of a commercial fluorescence microscope. The relay lens images the Fourier (pupil) plane of the objective onto the diffuser to shape the system's point spread function (PSF). The spectral camera has a 64-channel spectral filter array placed on top of a monochrome sensor. b) To reconstruct hyperspectral images from a single captured measurement, our algorithm starts with a monochrome 2D sensor measurement and passes it through an optimization problem with calibration data to recover the hyperspectral datacube. The recovered spectral scene here is fixed fluorescently-labeled *in vitro* cells with the spectra plotted to the right.

The imager comprises of three main components: a relay lens, a custom-engineered diffuser, and a spectral camera. The relay lens transfers the Fourier plane of the microscope's objective to an accessible location at the output port. The custom-engineered diffuser is

positioned one focal length away from the relay lens at the relayed Fourier plane to maintain shift invariance. The diffuser shapes the system's PSF, ensuring it spans multiple super-pixels on the spectral camera achieving full spectral sampling. The PSF's sharp caustic features encode the lateral position of each point source while preserving high-frequency information. Thus, the diffuser allows the system to capture both spatial and spectral details simultaneously from the sample. The hyperspectral camera is positioned at the focal plane of the diffuser to complete the optical path. The spectral camera employs an off-the-shelf CMOS sensor with a 64-channel spectral filter array adhered directly to the sensor plane. The filter array consists of 8×8 super-pixels, each containing 64 unique spectral filters, with each super-pixel spanning dozens of sensor pixels.

Forward Model

To computationally reconstruct the sample, it is necessary to first model the measurement formation of the imaging system. The system captures fluorescence emission, which is inherently incoherent, ensuring that light emitted from different points in the sample does not interfere. This results in a linear measurement model, where the total signal at the sensor is a weighted sum of contributions from all points in the scene enabling the use of a convolution-based forward model. The forward model, similar to the derivation in our previous work [39], models the captured sensor measurement, $\mathbf{b}[x, y]$, as:

$$\mathbf{b} = \sum_{\lambda=0}^{K-1} \mathbf{F}_\lambda[x, y] \cdot \mathrm{crop}(\mathbf{h}[x, y] \overset{[x,y]}{*} \mathbf{v}[x, y, \lambda]), \tag{3.1}$$

where the sample's hyperspectral datacube is denoted as $\mathbf{v}[x, y, \lambda]$, where x and y are the spatial dimensions, and λ represents the spectral dimension. The diffuser's PSF, $\mathbf{h}[x, y]$, is convolved with the sample $\mathbf{v}[x, y, \lambda]$ over the spatial dimensions, x and y, consistent with a linear shift-invariant imaging system. In our setup, the PSF does not vary significantly with wavelength, allowing $\mathbf{h}[x, y]$ to be approximated as independent of λ. The resulting convolved image is further filtered by the spectral filter array which controls the transmission of each wavelength channel. This is modeled by element-wise multiplication with $\mathbf{F}[x, y, \lambda]$, the calibrated spectral transmission matrix. Since the individual wavelength channels are incoherent, their intensity contributions can be summed across K spectral channels to compute the estimated measurement from an estimate of the hyperspectral datacube.

This forward model is similar to the photography case. However for microscopy, the magnification must be taken into account when sizing the reconstructed pixels. The effective magnification of the microscopy system combines the magnification of the microscope objective with the demagnification of the hyperspectral imager as shown in Equation **??**:

$$M_{\text{eff}} = M_{\text{obj}} \cdot \frac{f_{\text{relay}}}{f_{\text{diffuser}}} \tag{3.2}$$

The ratio of focal lengths between the relay lens and the diffuser determines the demagnification of the image. This demagnification is critical to fit the entire field of view onto the spectral filter array (4 mm). With our chosen values of $f_{diffuser} = 9$ mm and $f_{relay} = 39$mm, the effective magnification is 0.9× when using a 4 × objective. The effective magnification increases to 2.3× for a 10× objective. This effective magnification along with the sensor pixel size is used to size the reconstructed object pixels:

$$\Delta x_{recon} = \Delta x_{sensor}/M_{eff} \tag{3.3}$$

Reconstruction Algorithm

Because our inverse problem is an under-determined linear system with many possible solutions, we solve it by incorporating multiple priors that constrain the solution space. Specifically, native sparsity priors are applied to exploit the inherent spatial sparsity of some scenes, while additional spatial and spectral priors ensure smoothness. We further enforce a limited dictionary of spectral components to make up the overall datacube. This is relevant for fluorescence imaging where only a few different dyes are imaged within a scene. These constraints, rooted in compressed sensing theory, allow accurate reconstruction by leveraging the structure and properties of the hyperspectral datacube, even under the limited measurements provided by the system.

The hyperspectral datacube, $\mathbf{v}[x, y, \lambda]$, is first modeled as a decomposition of spatial and spectral components:

$$\mathbf{v}[x, y, \lambda] = \sum_{k=1}^{N_f} \mathbf{V}_k[x, y] \cdot \mathbf{U}_k[\lambda], \tag{3.4}$$

where $\mathbf{V}_k[x, y]$ represents the spatial weight map for the k-th fluorophore, and $\mathbf{U}_k[\lambda]$ represents its spectral profile, capturing its emission spectrum. An additional U_k component is included to account for any additional signal such as background or illumination leakage.

The spatial weights $\mathbf{V}_k[x, y]$ are computed from un-normalized weights $\mathbf{W}[x, y, k]$ using a softmax operation with a temperature parameter τ, followed by a reweighting term $\alpha[x, y, k]$ for intensity scaling:

$$\mathbf{V}_k[x, y] = \alpha[x, y, k] \cdot \text{softmax}\left(\frac{\mathbf{W}[x, y, k]}{\tau}\right). \tag{3.5}$$

Initially, the temperature parameter τ allows multiple spectral profiles to contribute to a single spatial location, enabling flexibility in the early stages of reconstruction. As optimization progresses, τ is gradually decreased, sharpening the softmax distribution and enforcing the selection of a single dominant spectral profile per spatial location, consistent with the assumption that only one fluorophore is present at each pixel. We deem this our low-rank, one-hot reconstruction.

The reconstruction algorithm optimizes $\mathbf{W}[x, y, k]$, $\alpha[x, y, k]$, and $\mathbf{U}_k[\lambda]$ to refine the hyperspectral datacube $\mathbf{v}[x, y, \lambda]$. This process incorporates prior knowledge, such as the known number of fluorophores, N_f, and the sparsity of active fluorophores, to guide the reconstruction toward physically meaningful results that align with the observed sensor measurements. Note that N_f serves as an upper limit of how many spectral components the algorithm learns. We do not make assumptions regarding the specific shape or peak location of the fluorescence spectra, maintaining generalization across samples.

The reconstruction is formulated as the minimization of a loss function that balances fidelity to the experimental measurement with regularization terms promoting sparsity as well as spatial and spectral smoothness:

$$\mathcal{L} = \|\mathbf{b} - \hat{\mathbf{b}}\|_2^2 + \lambda_{\text{TV}}\,\text{TV}(\mathbf{v}) + \lambda_{\text{spectral}}\|\nabla_\lambda^2 \mathbf{U}\|_1 + \lambda_{\text{sparsity}}\|\alpha\|_1. \tag{3.6}$$

The first term ensures consistency between the observed measurement $\mathbf{b}$ and the estimated measurement $\hat{\mathbf{b}}$ computed using Eq. **??**. The second term promotes spatial smoothness by penalizing high-frequency variations in $\mathbf{v}[x, y, \lambda]$ across the x and y dimensions. The third term enforces smoothness in the spectral profiles by penalizing large second derivatives along the spectral dimension. Finally, the sparsity term, $\lambda_{\text{sparsity}}|\alpha|_1$, reflects the native sparsity of the scene, enforcing the assumption that most pixels correspond to regions without active fluorophores. The parameters λ_{TV}, $\lambda_{\text{spectral}}$, and $\lambda_{\text{sparsity}}$ are hyperparameters that control the relative influence of each prior in the loss function.

By iteratively minimizing this loss function, the algorithm progressively refines the hyperspectral datacube, ensuring an accurate reconstruction that captures both the spatial and spectral properties of the sample. This optimization problem is solved using JAX's autograd functionality with the Adam optimizer from Optax [27], configured with $\beta_1 = 0.9$ and $\beta_2 = 0.999$, as per the standard momentum parameters.

Comparison with Alternatives

First, to demonstrate the advantage of the caustic pattern PSF of the diffuser, we compare reconstructions of a simulated object between three different cases. In all cases, we simulate fluorescent beads spelling CAL, with the spectral profiles of the lanthanide dyes used in Reference [14] and [41]. The fluorescent beads are 2.4 micron in diameter at the object plane. The spectral filter array is pixel aligned to the sensor and has ideal transmission curves with 100% transmission at the peak wavelength and 1% at all others. Each individual spectral filter is 20×20 micron squares arrayed into 8×8 superpixels. Each superpixel is 160×160 microns. The reconstruction results are in Figure **??**. The first column shows the system configuration, the second column depicts the captured image from a single bead, the third column shows the simulated measurements contrast stretched, and the fourth column shows the false-color hyperspectral reconstruction using our low-rank one-hot approach, with some zoom-ins.

In the first case as shown in Figure **??**,a the spectral camera is placed directly in the image plane of a 10× imaging system. The object is imaged onto the sensor, however, each bead image (24 micron diameter) only lands on a few of the spectral filters thus has insufficient sampling to recover the full spectrum. We attempt to use interpolation at each spectral channel to mimick demosaicing algorithms and recover the full spatio-spectral scene. However, there is insufficient information at each spectral channel and the recovered scene does spatially or spectrally match the ground truth.

In Figure **??**b, we try to increase the magnification to 80× to allow a spectrally homogoneous bead to land on the entire superpixel ensuring full spectral sampling, but we sacrifice the field of view. We follow the same procedure as the first case to recover the spatio-spectral scene.

In Figure **??**c, we stay with the 10× objective but reduce the numerical aperture to make the PSF wider so that each bead's light lands on the entire super-pixel. We follow the reconstruction process outlined in Section **??** using a Gaussian PSF and $N_f = 4$. The reconstructed image shows that the resolution suffers since Gaussian PSF attenuates high frequency information in the scene.

Finally in Figure **??**c, we show PSF shaping using the diffuser. The magnification is kept at 10×, and the field-of-view is maintained. The reconstructed object more closely matches the ground truth shape and spectra demonstrating the advantage of our technique. The diffuser's PSF maintains high frequency information in the scene while spreading out each bead's light across sufficient spectral filters. Our diffuser approach captures the best combination of resolution, field-of-view, and spectral information to match the ground truth for simulated datasets.

3.4 Experimental System Design

A custom hyperspectral camera was constructed in the lab using primarily off-the-shelf components. The core component was a board-level CMOS sensor (The Imaging Source, DMM 37UX178-ML) with a resolution of 3,072×2,048 pixels (6.3 MP) and a pixel pitch of 2.4 µm. To enable integration with the spectral filter array, the sensor's cover glass was removed (Wilco Imaging, Sacramento, CA). The hyperspectral filter array was sourced from Viavi Solutions (Santa Rosa, CA) and consists of an 8×8 grid of individual Fabry–Perot filters (10 µm × 10 µm each), fabricated as a dielectric stack of optical coatings on a glass substrate.

To assemble the spectral camera, the spectral filter array was bonded to the CMOS sensor using optical adhesive (Norland 61). A small drop of adhesive was applied to the sensor surface, and the filter array was carefully lowered, with its optical coating side facing the sensor. The placement ensured proper optical interfacing. The adhesive was cured under an ultraviolet lamp for 15 minutes to secure the bond.

The optical set up consisted of 3 components (a relay lens, diffuser, and spectral camera) added onto a standard microscope. The relay lens was aligned with the output side port

of a Nikon TE300 epifluorescent microscope to create a $2f$ system between the side port's image plane and the diffuser plane. The spectral camera was placed after the diffuser. This setup was also tested on a Zeiss Axio microscope using a side port adapter and cage system, which simplified alignment by limiting adjustments to the optical axis.

An achromatic scan lens (Thorlabs LSM03-VIS Scan Lens, EFL = 39 mm) was selected as the relay lens to minimize chromatic aberrations and field curvature at the diffuser plane. The engineered diffuser was positioned one focal length away from the relay lens ($f_{\text{relay}} = 39$ mm), and the spectral camera was placed at the diffuser's focal length ($f_{\text{diffuser}} = 9$ mm). The optical arrangement is shown in Fig. **??**a. The board-level camera was mounted onto a custom aluminum fixture to integrate it into a cage rod assembly, as illustrated in Fig. **??**a. The complete parts list and assembly instructions are provided in Supplementary Information **??**.

Engineered Diffuser Design

To multiplex light from the sample, a custom diffuser was designed to spread light across the spectral filters while preserving signal-to-noise ratio (SNR) and resolution. Previous work [39] used an off-the-shelf Luminit 0.5° diffuser, which produced a sharp caustic pattern. However, the light intensity varied along the ridges of the pattern, and significant light was directed into the regions between the bright ridges, decreasing SNR. In fluorescence microscopy compared to photography, total photon emission from each point in the scene is orders-of-magnitude lower. Thus, we want to spread the photons out to as few pixels as strictly necessary to achieve a high contrast PSF and limit shot noise, while maintaining sufficient multiplexing for compressed sensing.

To address these limitations, the custom diffuser was designed to distribute light more uniformly across the ridges, improving the evenness of light distribution among the spectral filters and enhancing spectral conditioning. Multiple pattern densities and focal lengths were fabricated and tested using the methods outlined in previous work [32]. The target PSF pattern was generated using a random generation algorithm, with a density matched to the spectral filter size to ensure uniform information spread. The diffuser's height profile was subsequently optimized using a differentiable design algorithm to achieve isotropic sharpness across the entire PSF pattern at a specific focal plane.

The final diffuser design had a focal length of 9 mm, with a Voronoi pattern featuring an average seed density of 44 dots/mm^2 and a mask size of 1.4 mm $\times$ 1.4 mm [32]. Additional details on PSF comparisons and diffuser specifications are provided in Supplementary Information **??**.

Calibration

Calibrating the diffuser's PSF and the spectral filter array's transmission is essential for accurate image formation modeling in the reconstruction algorithm.

Spectral calibration was performed immediately after assembling the spectral camera and prior to microscope alignment using a Cornerstone 130 monochromator and following the procedure described previously [39]. The monochromator's output slit was set to produce an 8 nm full-width half-maximum (FWHM) beam, scanned from 350 nm to 900 nm. The captured images were normalized by the monochromator's output power.

After coupling the diffuser and camera to the microscope via the relay lens, the diffuser PSF was captured by imaging a 5 µm fluorescent bead placed in the sample plane and imaged onto a region of the sensor not covered by the spectral filter, using a 4× objective.

3.5 Experimental Results

Resolution

We start by characterizing our system resolution experimentally. As this is a computational imager with a nonlinear reconstruction algorithm, its resolution is affected by the following: 1) sharpness of the diffuser's PSF, 2) focal length ratio between the relay lens and the diffuser, 3) condition number of the forward model matrix, and 4) any priors used in the reconstruction.

Theoretical resolution was calculated as the cross-correlation between simulated measurements of a shifting point source. The simulated measurements were obtained via the imaging forward model in Eq. **??** using experimental calibration data for the diffuser PSF, $h[x, y]$, and the spectral transmission matrix, $F[x, y, \lambda]$. We simulated measurements from both narrowband and broadband (uniform spectra) point sources. Figure **??**c shows the obtained theoretical resolution defined at 70% of the peak cross-correlation. We achieve 0.17 super-pixels on average across wavelength for narrowband and 0.18 super-pixels for uniform broadband points similar to [39]. The narrowband theoretical resolution varies slightly with wavelength due to the effective PSF erasure from the spectral transmission matrix. Joint design of the diffuser PSF and spectral filter may help with achieving consistent resolution across wavelength.

The system's two-point resolution was also measured experimentally with a 4× objective. Fluoromax-dyed aqueous green and orange beads (ThermoFisher) were diluted in water and a small droplet was placed on a glass slide, dried, and imaged. Due to the difficulty of precisely positioning fluorescent beads, a single 10 μm bead was imaged, shifted on a motion stage, and imaged again to simulate a two-source sample with varying separation distance. The resulting measurements were summed digitally to represent a two-source scene. Figure **??** shows that fluorescent beads spaced 0.12 super-pixels (20 μm) apart can be resolved. Notably, the experimental resolution exceeds the theoretical prediction due to the sparsity prior used in reconstruction.

Resolution in computational imaging systems is also scene-dependent. To evaluate system performance with a denser, more complex sample, we imaged the fluorescent digits on a negative US Air Force resolution target (Edmund Optics). To test performance on a com-

plex scene, we imaged a sample of 10 µm green and 30 µm orange fluorescent beads. The measurement and reconstruction are shown in Fig. **??**. Beads immediately next to each other located closer than the theoretical resolution limit could not be distinguished, but the reconstructed spectra closely matched the ground truth.

Note that this system is not diffraction-limited by the collection objective, and will have a lower spatial resolution than a traditional single channel fluorescent microscope with the same objective (ex: 30 micron vs 3 micron for a 4× objective).

Dynamic sample

A primary advantage of a snapshot system is the ability to capture dynamic samples. To demonstrate this, a drying water droplet containing fluorescent beads was imaged. As the droplet dried, the beads shifted positions, moving in and out of the focal plane. Sequential frames were acquired over a 10-minute period. The hyperspectral reconstructions of selected frames are shown in Fig. **??**. Particle tracking was performed on the reconstructed frames. As the droplet dried, the beads moved closer together, increasing the difficulty of resolving and tracking them individually.

MRBLES beads

To evaluate performance on a sample with sharper spectral features, MRBLES hydrogel beads were imaged. These beads, used in multiplexed bioassays, represent a set of six distinct spectral codes and vary in diameter (20–50 µm). Hydrogel lanthanide beads were synthesized according to Reference [14] with higher concentration of lanthanide dye to increase brightness. For imaging, the beads were placed on a quartz slide and excited with an ultraviolet (285 nm) LED in trans illumination. An additional 400 nm long pass filter was placed over the objective lens to to reject UV excitation and limit autofluorescence of the objective's glass. Ground truth spectra for lanthanides was acquired using a fluorometer (Fluorolog-3). The measurement and reconstruction are shown in Fig. **??**. The reconstructed bead spectra match the ground truth within the spectral resolution of the system. Due to the sample's low brightness, an acquisition time of 60 seconds was required.

Cells

Fixed fluorescently-labeled human umbilical vein endothelial cells (HUVECs) were imaged to further evaluate system performance when imaging samples with overlapping emission spectra. The fixed cell samples were cultured and fluorescently labeled using CellTracker Green, CellTracker Orange, and Qtracker 655 dyes (ThermoFisher). Ground truth spectra for the fluorescent dyes were obtained from SpectraViewer on ThermoFisher's website. The measurement and reconstruction are shown in Fig. **??**. The reconstructed spectra were compared with the vendor-provided ground truth spectra, demonstrating consistency within the spectral resolution of the system. The red fluorescent dye emission was significantly

brighter (10x) than the orange dye, hence the orange fluorophore component is missing in the low rank sparse reconstruction.

Dense samples

Lastly, we tried to image more complex scenes. We imaged patterned HUVEC cells in the shape of "CAL". These cells were labeled with CellTracker Green and CellTracker Orange. Single-cell patterning was achieved with a photolithography-based process called high-throughput DNA-directed patterning (htDNA-dp) [52] to create the "CAL"-shaped cell sample. HtDNA-dp employs photolithography to selectively expose regions of an aldehyde-coated glass slide, which are subsequently incubated with single-stranded DNA oligonucleotides. Through reductive amination, the oligonucleotides bind to the exposed areas. Cells tagged with complementary single-stranded DNA oligos are then flowed over the slide, where they hybridize to the patterned regions. This technique enables precise, high-resolution spatial positioning of individual cells with high throughput. For this study, three distinct photolithography masks and oligo sequences were used to pattern the letters "CAL."

The reconstructed scene and spectra are shown in **??**a. The reconstructed spectra matches the vendor-provided ground truth. The spatial reconstruction has artifacts due to the low contrast in the sample between the HUVEC cells and the background. We also imaged the zero from a USAF resolution target in Figure **??**. The reconstruction of this sample depended more strongly on total variation priors.

In addition to being significantly dimmer, these denser fluorescent samples activate fewer spectral channels compared to previous broadband scenes imaged by Monakhova *et al* in the photography application [39]. Thus, there aren't as many activated sensor pixels making spatial recovery more difficult.

3.6 Discussion

The Spectral DiffuserScope has been demonstrated as an effective method for simultaneously capturing spatial and spectral information about dynamic fluorescence microscopy samples. A primary advantage of this approach is its compact and simple design, which integrates easily with existing microscopes. The attachment can be built with minimal effort, enabling hyperspectral sample collection. Additionally, the hyperspectral imager attachment is portable and can function as a standalone imaging system for field use when magnification is not required.

Demonstrated applications include particle tracking, bead imaging, and cell imaging. The system is well-suited for use in microfluidics and other lab-on-a-chip applications. Beyond biological samples, it is also applicable to materials science and other fields, provided the samples are sparse and sufficiently bright.

The absence of moving parts is the primary advantage of this system compared to a filter wheel-based fluorescence microscope, which remains the most common approach today.

While this filter array based system is a snapshot hyperspectral method, we note it does not inherently allow faster acquisition times than a filter wheel system. In a snapshot system, light is distributed across wavelength channels spatially (pixels), whereas in a filter wheel system, light is distributed across wavelength channels temporally. To compare fairly, the total capture time per frame is equivalent for both filter wheel and filter array systems. Consequently, if the acquisition is exposure-limited, there is no time-saving advantage in using a snapshot system. However, the snapshot system provides the benefit of continuous acquisition, which can be particularly advantageous when the speed of moving parts imposes a limitation in a filter wheel-based setup.

Limitations The camera's sensitivity posed a significant challenge in our experiments. The system used a cost-effective, room-temperature CMOS camera modified with a spectral filter array attached. Filter wheel-based fluorescence systems typically allow individual adjustment of exposure time for each channel and use higher grade scientific cooled CMOS camera. In our system, weaker channels shared the same exposure as stronger, making it more difficult to visualize weaker signals without saturating the stronger ones. A camera sensor with higher dynamic range or pixel-adjustable exposure settings would address this limitation. In particular, a cooled scientific CMOS (sCMOS) camera could improve noise performance and sensitivity. However, sCMOS sensors are more expensive and it is generally not desirable or straightforward to remove the coverglass over the sensor. While the design can work with the cover glass intact, it tends to introduce angle sensitivity in the spectral calibration and alters the forward model, which should be accounted for in the inverse problem [47, 48].

Stray light was another major limitation, causing reconstruction artifacts. Measurements were conducted using an older TE300 microscope, which likely had damaged fluorescence filters contributing to stray light. Additionally, reflections between the spectral filter glass and the diffuser introduced reconstruction artifacts. Anti-reflective coating on the back of the spectral filter array's glass substrate could mitigate these issues in the future. Optical alignment also played a critical role in maintaining spatial invariance across the field-of-view. Spatial invariance was verified visually by inspecting the point spread function across the sensor's unfiltered side. The spectral filter was not pixel-aligned to the camera, which necessitated experimental calibration with a monochromator to get the spectral response of each individual camera pixel. A pixel-aligned filter in future designs would reduce calibration requirements and improve overall system performance based on simulations performed.

Reconstruction resolution and quality is scene complexity dependent. The system performed best with bright, sparse objects, while dense narrowband fluorescent scenes failed to reconstruct because the compression ratio was too high. Dense scenes required broader spectral features to activate more pixels. For example, imaging the bars of a green fluorescent USAF resolution target was unsuccessful because the bars were too narrowband to activate enough pixels. Choosing a spectral filter array tailored to the fluorophores being imaged would significantly enhance performance. A custom-designed spectral filter array optimized for the specific emission spectra of the fluorophores would improve light throughput and sensitivity, thereby reducing acquisition times, particularly for dim samples such as MRBLES

beads.

Future work To assist with low-light imaging, this work utilized a custom-designed diffuser. Future developments could jointly optimize the diffuser and spectral filter array through data-driven, end-to-end design, further enhancing light throughput and system performance.

The droplet samples were inherently 3D, but the reconstruction assumed a 2D model, leading model mismatch as beads moved in and out of the focal plane. In the future, a 3D hyperspectral reconstruction algorithm could be implemented. This would require acquiring a PSF stack at different focal planes and modifying the forward model to incorporate a 4D datacube, (x, y, z, λ), leading to significantly increased computational requirements.

Additionally, parameterized representations such as coordinate-based multi-layer perceptron (MLP) networks or Gaussian splatting could be employed to reduce the number of parameters in the reconstruction. These approaches could also impose stronger priors or enforce continuity between frames of dynamic samples, potentially improving reconstruction fidelity and particle tracking accuracy. In this work, a physics-based classical reconstruction algorithm with sparsity constraints was deliberately chosen over a deep learning-based approach to maintain the system's agnosticism to the types of samples it may encounter. Collecting a diverse dataset of fluorescent hyperspectral microscopy samples would assist with the training of data-driven approaches.

3.7 Conclusion

The Spectral DiffuserScope has been demonstrated as an effective method for snapshot hyperspectral fluorescence microscopy. Its ability to capture dynamic samples was highlighted through particle tracking in drying water droplets. Experimental reconstructions of fluorescently-labeled cells and hydrogel lanthanide beads further showcased the system's versatility for bio-imaging. The Spectral DiffuserScope offers distinct advantages over traditional hyperspectral microscopy approaches by eliminating moving parts and enabling potential miniaturization for portable field applications as well as being easily combined with existing benchtop microscopes.

We provided the bill of materials and assembly instructions for the hyperspectral camera imager attachment and the open soure code for the reconstruction pipeline in the Supplement. We also mentioned several improvements to the hardware and reconstruction pipeline to push performance further. We hope these efforts will enable others to build on this work.

Overall, the Spectral DiffuserScope presents a promising approach for hyperspectral microscopy, with potential for broader use cases and further optimization.

3.8 Supplementary methods

We expand on the methods to enable others to build the Spectral DiffuserScope.

Bill of materials

CAD file for camera adapter plate is uploaded to the data directory of this project and also available here: `https://cad.onshape.com/documents/449caf9366b28bb97cd6dcee/w/f675872992f46a11f2c93e37/e/8b24da2db02d465414c0caa0`. The plate was CNC machined from aluminum through a rapid prototype service. See Figure **??** for a drawing of the camera adapter plate.

We used a custom engineered diffuser from our collaborators. Alternatively, an off the shelf Luminit 0.5 degree holographic diffuser can be obtained from EdmundOptics.

Usage Instructions

1. Assemble the spectral camera according to the instructions in main text Section **??**.
2. Calibration the spectral filter matrix according to instructions in main text Section **??** and Supplementary Info **??**.
3. Assemble using the instructions in Supplementary Info **??**.
4. Calibrate the diffuser point spread function using the instructions in main text Section **??**.
5. Slide the spectral camera using the 60mm translation plate (part K) so that the point spread function now lands on the center of the spectral filter array.
6. The setup is now ready for imaging. Place a fluorescent sample in the microscope and acquire image using TIS software, Micromanager, or other software. Make sure to also collect a background image ideally from an empty part of the sample slide for subtraction.
7. Preprocess the calibration data using the instructions in main text **??** and in the spectral calibration notebooks in the Github repo referenced.
8. Run the hyperspectral datacube reconstruction code in the Github repo referenced.

Optical setup assembly instructions

1. Assemble the spectral camera according to the instructions in main text Section **??**.
2. Calibration the spectral filter matrix according to instructions in main text Section **??** and Supplementary Info **??**.
3. Attach the Zeiss microscope sideport c-mount adapter (part A) to the microscope sideport.
4. Attach the C-mount internal to SM1 external adapter (part B) to part A.

5. Insert the 500 nm long pass filter (part D) into the 30mm cage plate (part C) and attach to part B.

6. Attach the achromatic scan lens (part G) to the XY translation cage plate (part E) using the M25x0.75 to SM1 adapter (part F).

7. Attach part EFG to part C using cage rods (part L).

8. Align along x and y. The microscope adapter and cage system should already be aligned to the optical axis. But if not, align the scan lens to the center of the optical axis by adjusting the XY translation cage plate. This can be done by imaging a bright object in the microscope and select sideport for output. Remove the scan lens. Focus the object 1 meter away on a white paper. Place the scan lens back in the setup and adjust the XY translation cage plate until the image is in the same place as before.

9. Align the scan lens along z (optical axis) so it is one focal length away from the original sideport imaging plane. This can be done by imaging a bright object. Focus on the object using the eyepiece and then switch to the sideport. Place the scan lens roughly 2 focal lengths away. This should make a 4f imaging system. Place a monohcrome camera temporarily in the secondary image plane. Then as you move the scan lens closer to the sideport, the secondary image plane should move farther away. Adjust the monochrome camera placement to stay in focus. Once the monochrome camera is 1 meter away, the scan lens is effectively imaging at infinity and is roughly one focal length away from the sideport image plane.

10. If using a custom engineer diffuser (part Q), you can use a piece of tape with a square aperture to attach the diffuser to the mounted pinhole (part J) and then insert into the lens tube (part I) If using an off the shelf mounted diffuser, insert directly into part I.

11. Attach part I to the 30mm to 60mm cage plate adapter (part H).

12. Attach a post (part N) and post holder (part O) to the bottom of part H. Keep the post holder screw loose until the next step.

13. Attach the part assembly HIJQ to part E using the previously attached cage rods (part L). It's important that the cage rods don't stick out too far past part H (hence best to use 3" rods). Tighten the post holder screw on part O and fasten part O to the optical table.

14. Attach the board level image sensor (part S) with the glued spectral filter to the camera adapter plate (part P) using 1" cage rods (part M).

15. Use four of the 1" cage rods (part M) to attach the camera adapter plate (part P) to the 60mm translating cage segment plate (part K).

16. Use the remaining four 1" cage rods (part M) to attach part assembly KPS to part H.

17. Align the camera along the optical axis to the focal plane of the diffuser. This can be done by imaging a 5 micron fluorescent bead on the side of the image sensor unoccluded by the spectral filter and moving the camera until diffuser's caustic ridges are in focus. We used The Imaging Source's IC Capture software to view the camera feed.

Spectral calibration

The output power measured on the Cornerstone 130 monochromator was used to normalize the spectral calibration matrix acquired. See Figure **??**

Diffuser design and optimization

We iterated on the diffuser design to create a high contrast PSF as shown in Figure **??**.

3.9 Acknowledgements

This work is currently under preparation for submission. It was conducted in collaboration with Eric Markley, Kristina Monakhova, and Laura Waller. Kyung Chul Lee, Seung Ah Lee, Junghyun Bae, Nakkyu Baek, and Wook Park assisted with the phase mask design and fabrication. Minsung Cho, Youngbim Lim and Polly Fordyce assisted with hydrogel bead sample prep and capture. Stephanie Eberly and Lydia Sohn assisted with fixed cell sample prep and capture. William Houck provided the spectral filter.

Table 3.1: Hyperspectral Imaging Approaches

Reference	Approach	Samples Shown	Spectral Channels and Bandwidth	Advantages	Disadvantages
This work	Multiplexing using phase mask onto spectral filter array + compressed sensing	Fluorescent beads, fixed cells	64 channels	Compact, simple setup, customizable filters, can extend to 3D, Large FOV - can control spatial & spectral resolution separately	Restricted to sparse, bright samples - SNR tradeoff with the number of channels - Reconstruction relies on spectral priors
Wu, *Sci Reports*, 2016 [66]	Lightfield camera array with filters	Algae, lymph node, larvae	25 channels; range depends on filters	Volumetric, live imaging, customizable filters	Large, expensive, complex setup - SNR and size tradeoff with the number of channels
Cull, *App Optics*, 2010 [10]	Coded aperture dispersion + compressed sensing	Fluorescent beads	22 channels, 490-700nm	Adaptable to benchtop setups	Limited channels - Reconstruction relies on spectral priors
Lavagnino, *Biophys J*, 2016 [31]	Image dispersion onto a large sensor	Live pancreatic islets	60 channels	Live samples, subsecond temporal resolution	Limited magnification, long assembly
Orth, *Optica*, 2015 [44]	Microlens array and prism to disperse onto a large sensor	Full well HeLa cells and fluorescent beads	13 channels *adjustable	Large FOV, targeted for drug discovery-	Limited spectral channels
Zhang, *Nat Methods*, 2015 [74]	Prism to disperse along one direction + large sensor	Organelles inside fixed cells	650-800nm, 25 channels	Single molecule sensitivity	Limited to sparse samples - Not truly a snapshot since need multiple exposures to build a full image

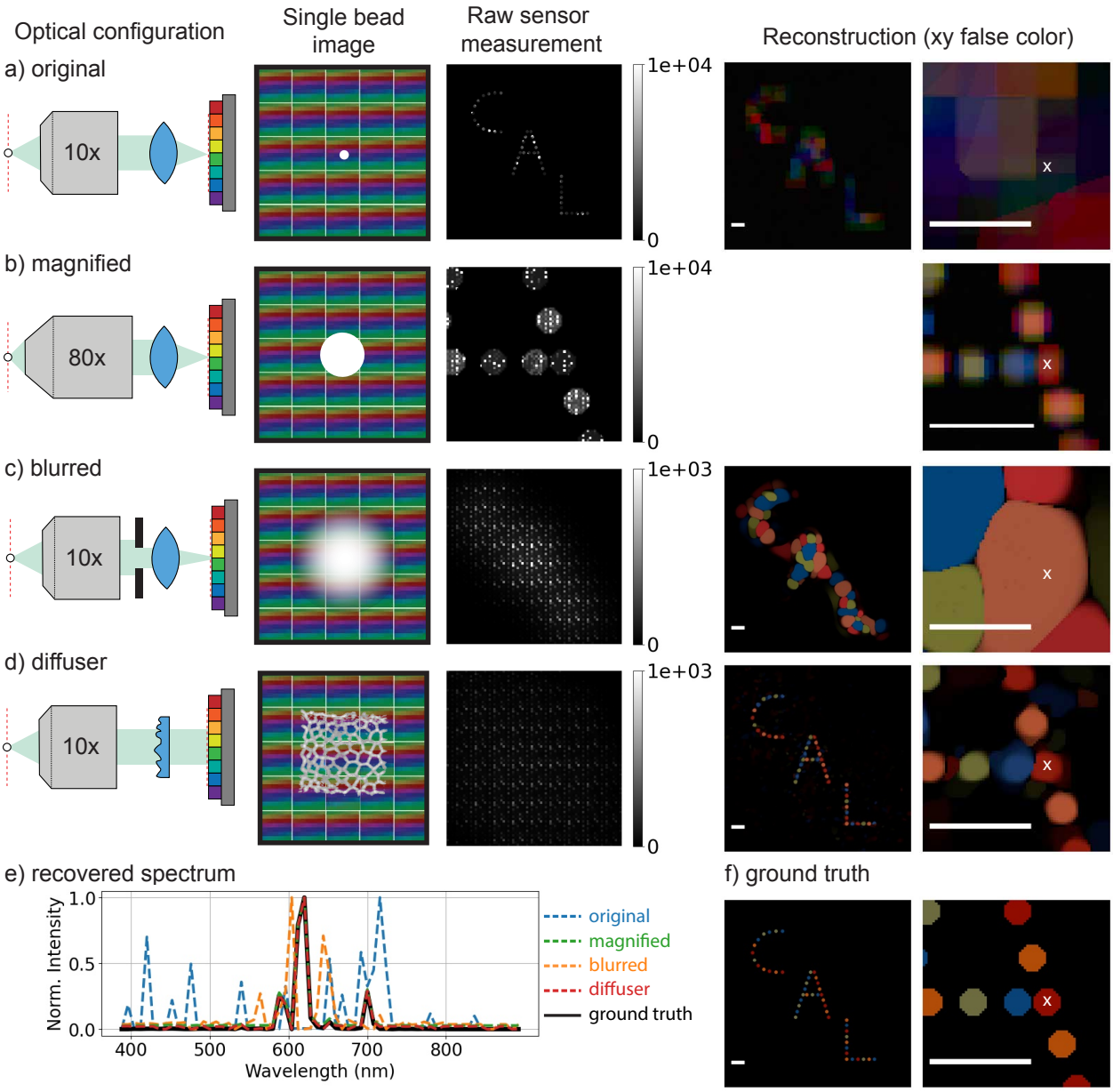

Figure 3.2: Comparison of various snapshot configurations for capturing a hyperspectral datacube using a spectral filter array based camera, in simulation. a) Original system with 10x magnification and one-to-one imaging. b) A higher magnification objective c) A system with a blurred PSF d) Our approach: a diffuser is placed in the Fourier plane of the microscope to spread the light across multiple filters on the spectral camera, giving good spectral reconstructions without severely sacrificing spatial resolution. e) Bead spectra at the location marked "x" from the different configurations' reconstructions showing that accurate spectral recovery is possible with the diffuser PSF. f) The ground truth sample used for the simulation - a scene of spectrally-encoded hydrogel beads. All scale bars = 10 μm. False color recons contrast stretched for visualization with gamma factor = 0.8.

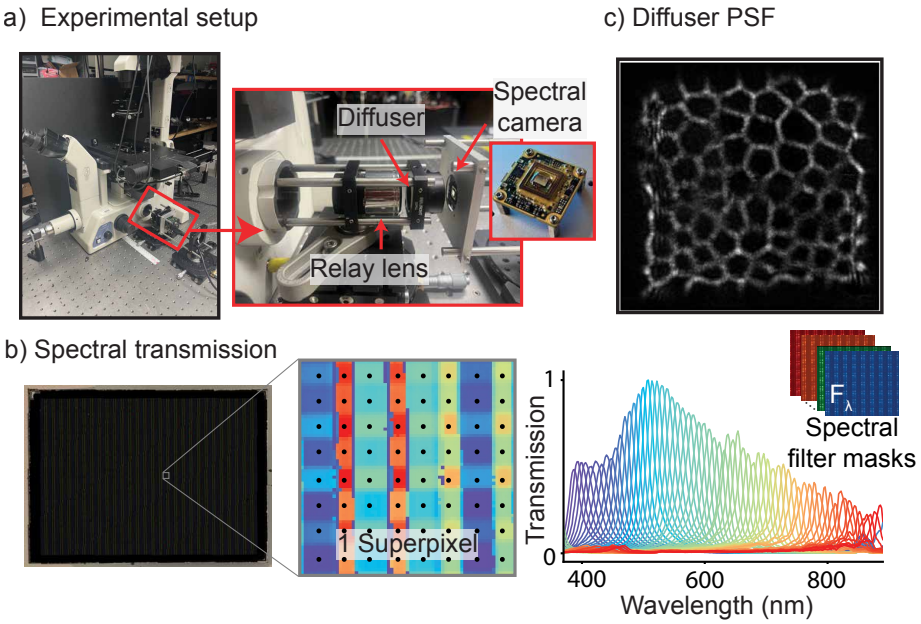

Figure 3.3: (a) Experimental setup with our hyperspectral camera mounted on the side port of a Nikon TE300 microscope, consisting of a relay lens, diffuser, and spectral camera. The spectral camera is a board-level CMOS sensor with the cover glass removed and a spectral filter adhered to its surface. (b) The diffuser's PSF, captured from a 5 µm fluorescent bead sample, is shown on the unfiltered pixels of the sensor. (c) The spectral transmission matrix was obtained by scanning the source wavelength with a monochromator. A full-sensor image illustrates the placement of the spectral filter. A zoomed false-color image of the spectral calibration matrix displays the 64 filters within a single super-pixel. The black or dark filters correspond to near-infrared transmission. To the right, the measured transmission spectrum of each filter is shown.

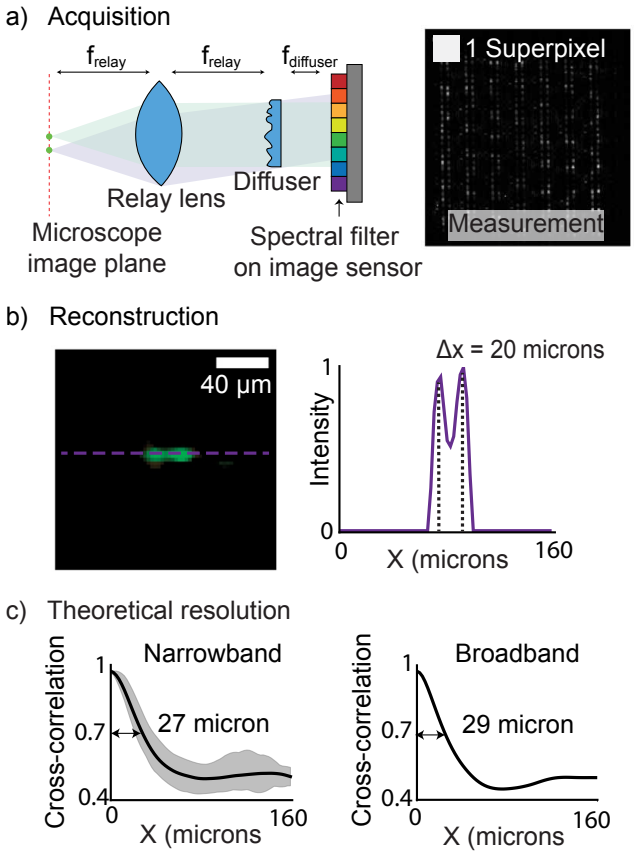

Figure 3.4: Two-point resolution test demonstrating sub-super-pixel resolution. (a) Acquisition setup showing the optical path after the microscope image plane and an example sensor measurement. (b) Experimental reconstruction of a two-source sample, with a spatial cross-section along the dashed purple line demonstrating peak separation of 20 μm. (c) Theoretical resolution defined at 70% peak cross-correlation of simulated measurements from two point sources. The narrowband source is shown on the left (range and average plotted), and the broadband (uniform spectra) source is shown on the right.

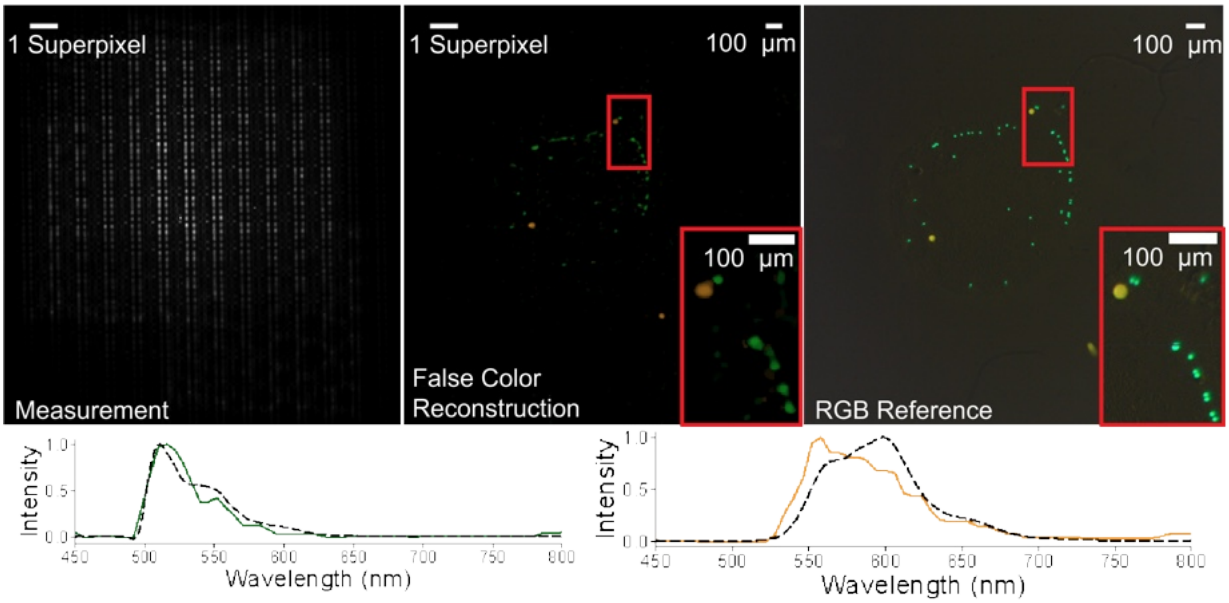

Figure 3.5: A sample with 10 µm green and 30 µm orange fluorescent beads imaged with a 4× objective demonstrates resolved features within a single super-pixel. Left: measurement (contrast-stretched for visualization) with a scale bar indicating 1 super-pixel. Center: false-color reconstruction with zoomed inset. Bottom left: spectra of annotated beads 1 and 2 compared against ground truth. Right: spatial ground truth captured on a color camera.

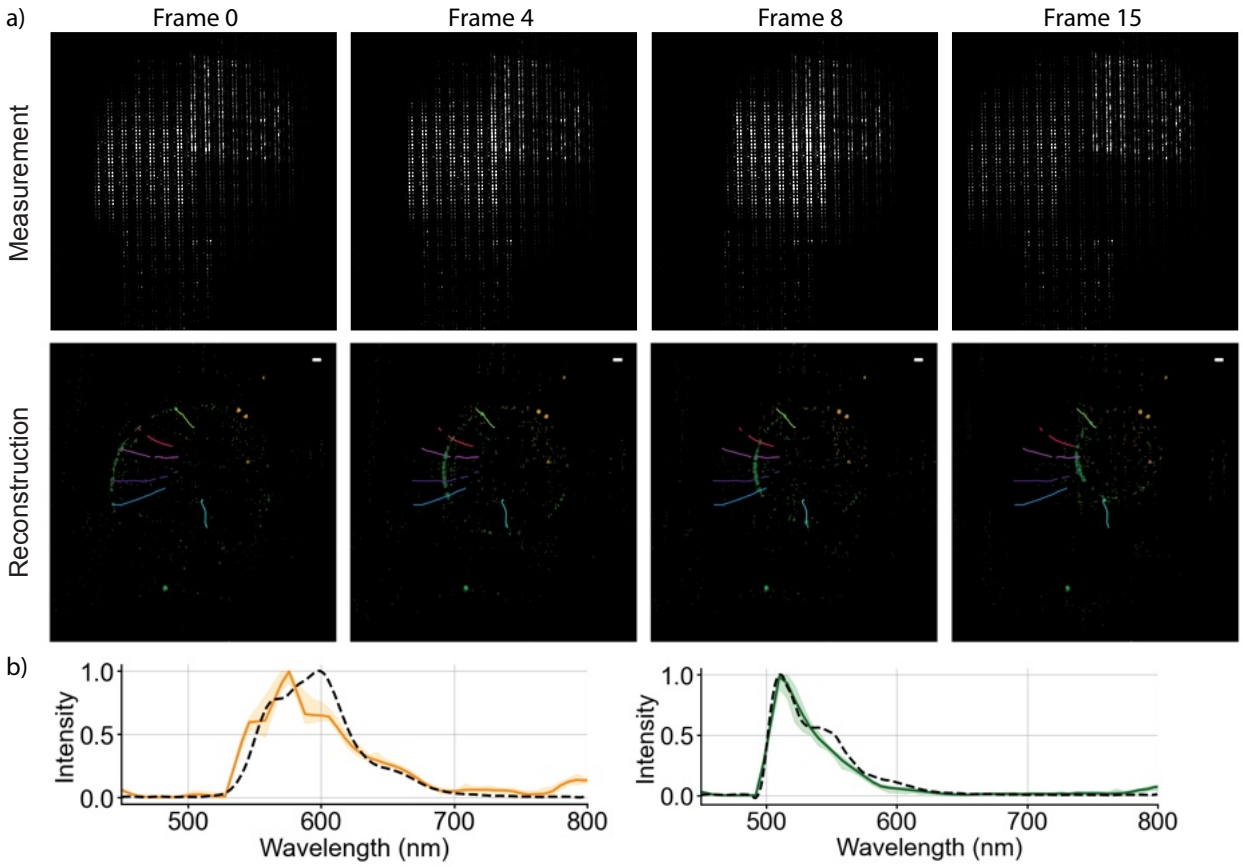

Figure 3.6: Several frames of a reconstructed hyperspectral video of a drying water droplet with fluorescent beads in it. The droplet was imaged over 10 minutes, 2 sec exposure per frame, 4× objective. Top row shows the snapshot measurement of sample over time, and below it is the spatial reconstruction of the corresponding frame. Particle tracking was done on the reconstructed frames to show the movement of the beads. The spectra of a single bead over time was captured and remains consistent.

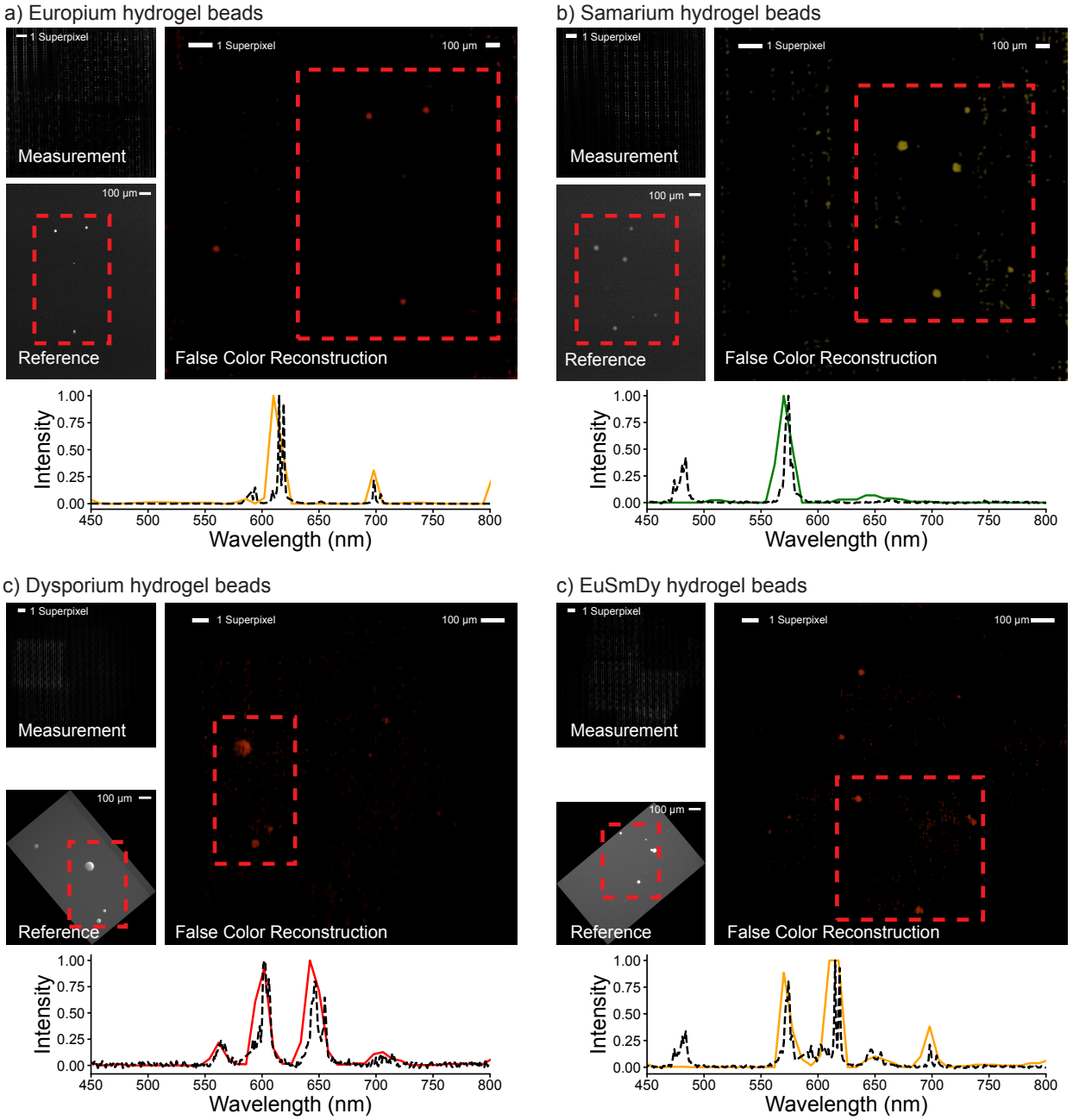

Figure 3.7: Multiplexed bioassay beads imaged using our hyperspectral microscope. (a) Europium, (b) Dysprosium, (c) Samarium, and (d) a ratio combination of 10% Eu, 34% Sm, and 4.25% Dy. The measurement is shown on the left, with the false-color reconstruction on the right. The spectra of the beads are compared against the ground truth on the bottom. The beads range from 20–50 µm in diameter. Measurements were acquired with a 60-second exposure using 4× and 10× objectives.

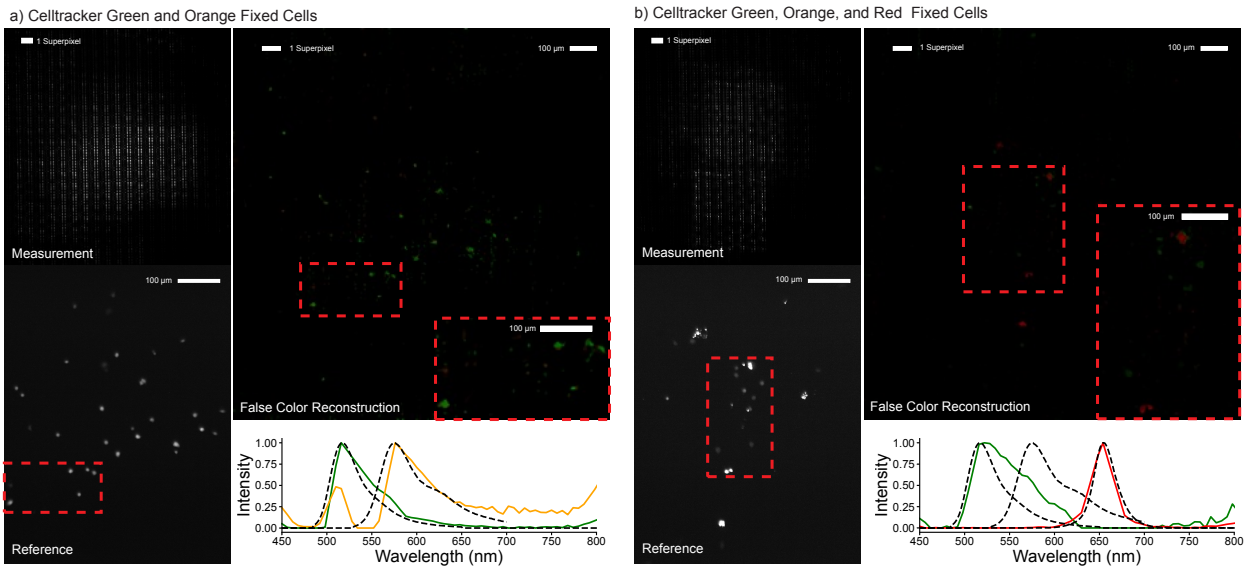

Figure 3.8: Fixed fluorescently-labeled cells imaged using our hyperspectral microscope, enabling full spectral capture and unmixing. (a) human umbilical vein endothelial cells (HUVEC) labeled with CellTracker Green dye. (b) HUVEC labeled with CellTracker Green, CellTracker Orange, and Qtracker Red dyes. Images were acquired with a 10× objective.

Item	**Part Number**	**Quantity**	**Identifier**
Zeiss microscope sideport c-mount adapter	Zeiss 60N-C	1	A
Cmount internal to SM1 external adapter	Thorlabs SM1A10	1	B
30mm cage plate	Thorlabs CP33T	1	C
500 nm long pass filter	Thorlabs FELH0500	1	D
XY translation cage plate	Thorlabs CXY1A	1	E
SM1 external to M25x0.75 internal adapter	SM1A12	1	F
Achromatic scan lens	Thorlabs LSM03-VIS	1	G
30mm to 60mm cage plate adapter	Thorlabs LCP33	1	H
SM1 0.5” lens tube	Thorlabs SM1L05	1	I
2.5 mm pinhole	Thorlabs P2500K	1	J
60mm translating cage segment plate	Thorlabs LCPX1	1	K
3” cage rods	Thorlabs ER3	4	L
1” cage rods	Thorlabs ER1	8	M
Optical post	Thorlabs TR1.5	1	N
Optical post holder	Thorlabs UPH1.5	1	O
Camera adapter plate	see link below	1	P
Diffuser	see text below	1	Q
Spectral filter array	Viavi Solutions	1	R
Board level image sensor	TIS DMM 37UX178-ML	1	S

Table 3.2: Parts list for Spectral DiffuserScope setup

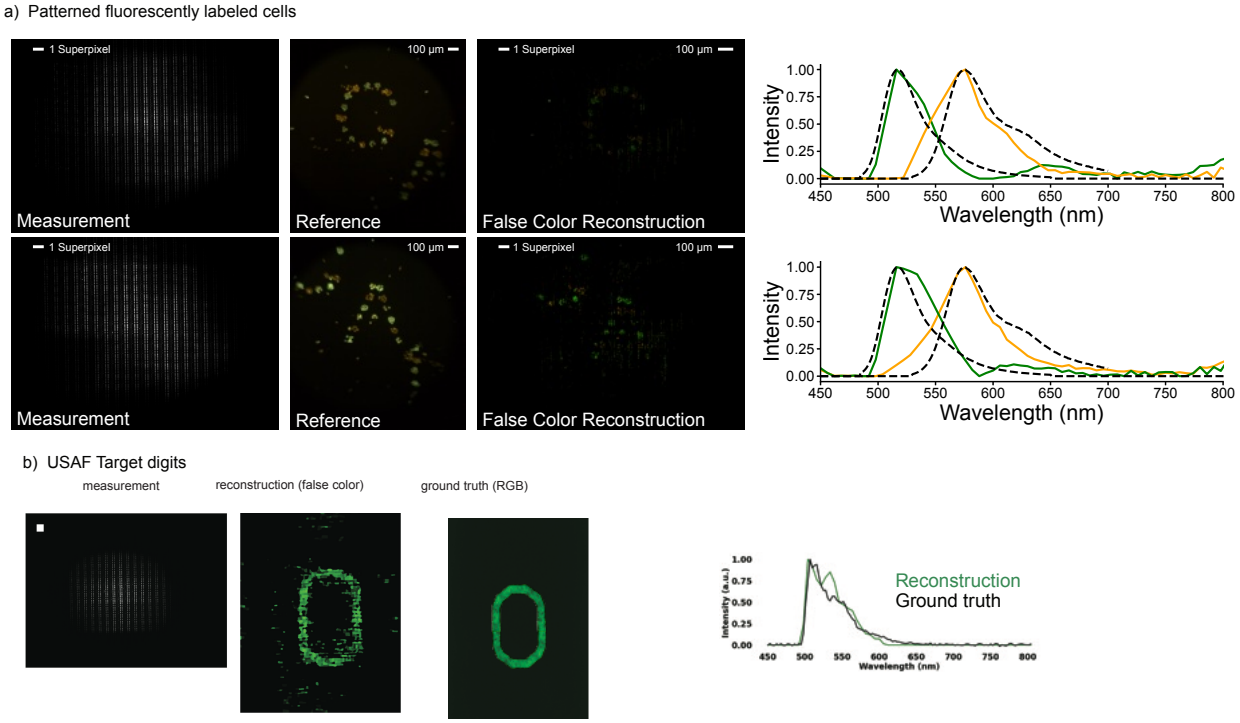

Figure 3.9: a) HUVEC cells patterned into a CAL shape labeled with Celltracker Green and Celltracker Orange dye. Multiple fields of view (3 total) were stitched together to capture the whole shape. Raw measurements shown on far left. 10× objective. b) Zero-digit of the USAF resolution target.

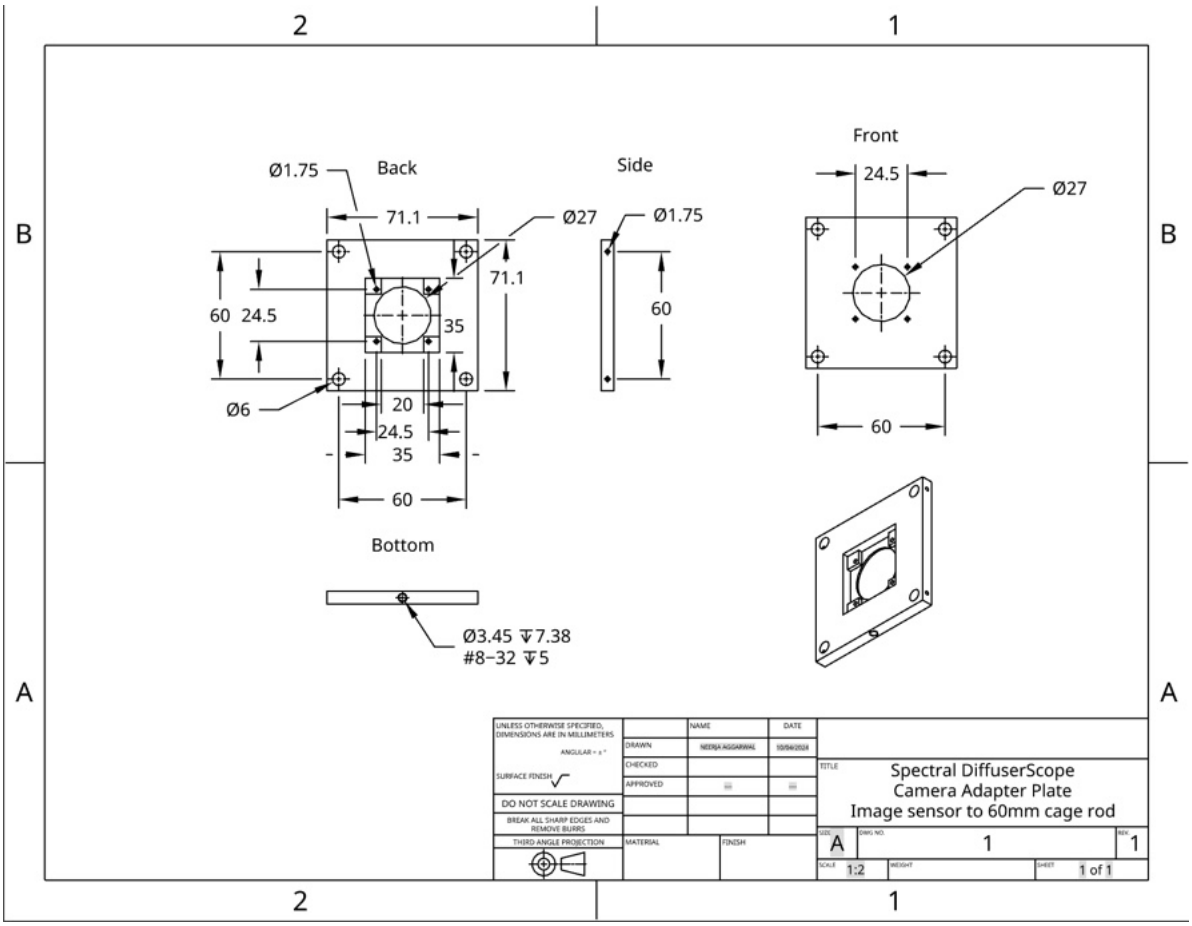

Figure 3.10: Drawing for the camera adapter plate. All dimensions in millimeters.

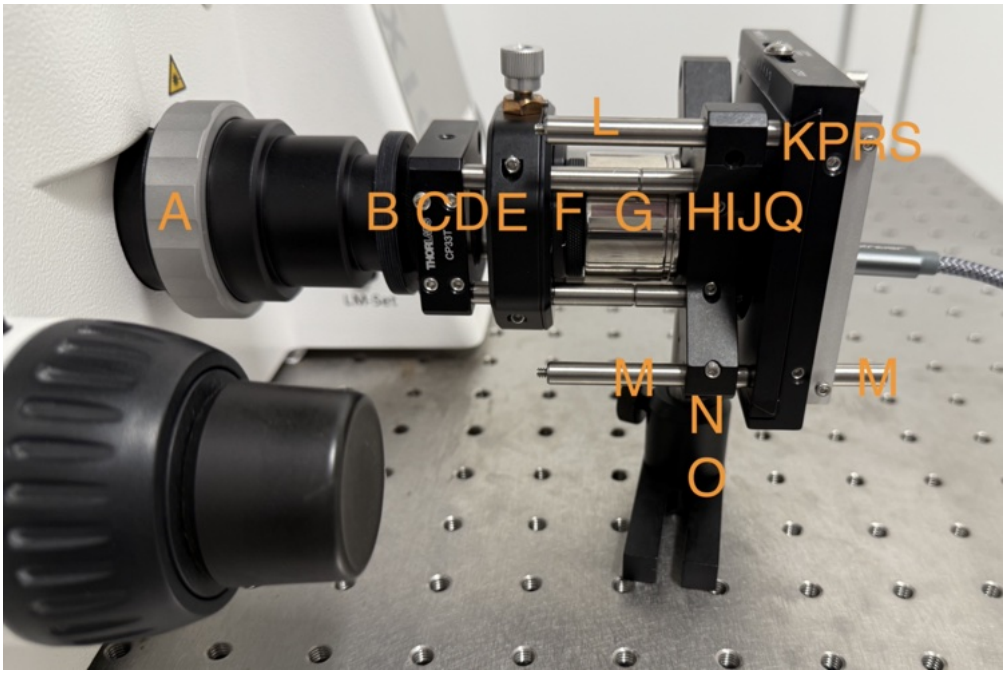

Figure 3.11: Annotated image of the optical setup with labeled parts. Note, there are variations of parts B and M in the image.

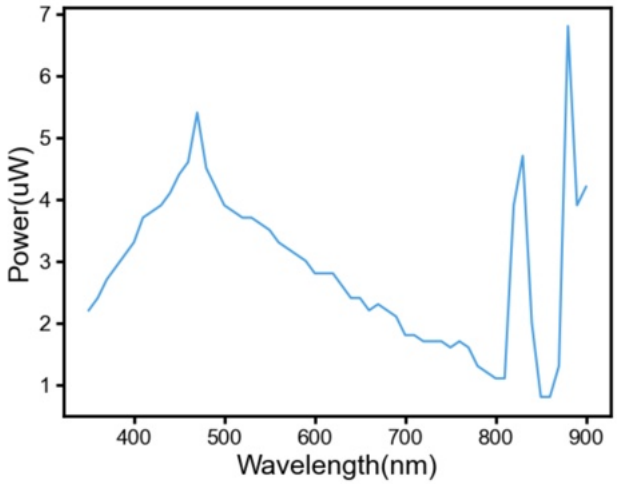

Figure 3.12: Output power for Cornerstone 130 monochromator

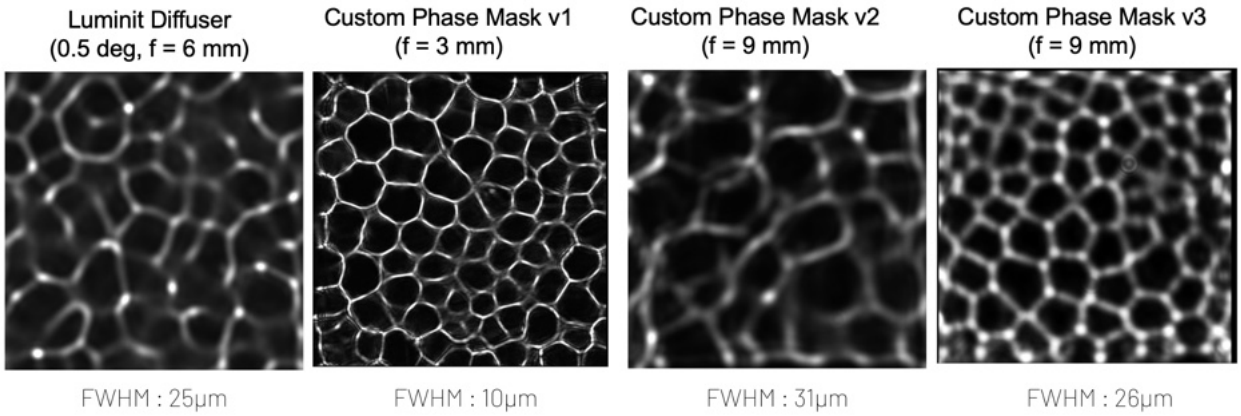

Figure 3.13: Diffuser point spread functions for various designs. Note, these images were collected according to Reference [32]

Chapter 4

Spectral Fourier ptychography using filter array

This work was published in the Conference Proceedings of SPIE Photonics West in 2025 [2] with co-author Laura Waller. It is reproduced below. We would like to acknowledge Nalini Singh, Eric Markley, Kevin Zhou, Yunzhe Li, and Mingxuan Cai, and Ruizhi Cao for helpful discussions and guidance.

4.1 Abstract

Spectral Fourier ptychography achieves high resolution transmission imaging of sample at multiple wavelengths. We propose placing a spectral filter array in the Fourier plane of the imaging system and scanning the illumination angle to capture each spatial frequency component at each spectral channel. We demonstrate via simulation high spatial and spectral reconstruction fidelity under limited measurements by using spatio-spectral priors.

4.2 Introduction

Traditional microscopy techniques often face a trade-off between spatial resolution and field of view, limiting their effectiveness in capturing detailed information across large tissue samples. Additionally, hyperspectral imaging typically faces resolution challenges when trying to capture multiple spectral (i.e. wavelength) channels at once. In this work, we propose a novel approach that combines the strengths of Fourier ptychography and hyperspectral imaging, leveraging compressed sensing and priors to reconstruct high resolution, wide field-of-view, and hyperspectral data with reduced measurements. This approach has the potential to significantly improve the efficiency and effectiveness of tissue diagnostics, enabling rapid and detailed analysis of biological samples.

Fourier ptychography microscopy (FPM) allows gigapixel imaging of biological tissue with large field of view, high resolution, and large depth of field [25]. It uses multiple images

captured with varying angled illumination to scan through the Fourier space of the object and achieve a higher synthetic aperture. Angled illumination creates a phase ramp at the sample plane, which translates to a shift in Fourier space of the object spatial spectrum. Different spatial frequencies are shifted into the aperture by different angles of illumination, and the full synthetic aperture is sampled through multiple acquisitions. The multiple low resolution images, containing different spatial frequencies are combined to form a high-resolution image. Fourier ptychography is being used widely for pathology applications. The work by Tian et al. [60] demonstrated gigapixel imaging of a stained tissue sample capturing both amplitude and phase information. Unstained or label-free tissue samples have also been imaged primarily via quantitative phase eliminating the need for sample prep [62]. Most previous work in Fourier ptychography has focused on illumination and reconstruction at a single wavelength to follow the quasi-monochromatic assumption. There has been some work in using RGB (red, green, and blue) LED arrays as illumination sources and color cameras as detectors to do multifocal plane imaging [43] and single shot quantitative phase imaging [56].

Recently there has been some interest in hyperspectral imaging (HSI) of tissue samples. Scientists have been studying the reflectance spectra of tissue for labeled or label-free diagnostics, especially in the field of cancer detection. For example, work by Lu et al. [35] demonstrated the association between the histological features of neoplasia and the spectral signature of the corresponding tissue measured by reflectance HSI. There are many ways to capture hyperspectral information. Spatial scanning collects the full spectra at every point in the sample, one point at a time. Spectral scanning captures the entire field of view one spectral channel or color at at time. Previous work by Monakhova et al. [39] demonstrated snapshot sensing by capturing the full spatio-spectral datacube in a single acquisition and relying on compressed sensing for reconstruction. Here, we propose a new way of capturing hyperspectral information by scanning in spatial frequency space. By using Fourier ptychography, we can build up the resolution of the spatio-spectral data cube as we collect higher spatial frequencies.

The third concept we leverage is compressed sensing. Data informed priors allow for reconstruction with reduced measurements. In our previous snapshot hyperspectral work [39], we were able to use sparsity priors and multiplexed measurements to reconstruct more voxels than pixels in our sensor. Other work has also shown the use of priors in FPM like total variation (TV) [54] or implicit neural networks [76] to reduce the overlap requirements for the case of highly-multiplexed measurements. In this work, we propose a spectral filter array in Fourier space to add a different kind of spatial and spectral multiplexing to the 3D hyperspectral datacube measurements, which can then benefit from careful choice of priors to enable high-quality reconstructions.

Previous work in spectral Fourier ptychography used a wavelength tunable source such as a filter wheel placed on a halogen lamp [73] or a multicolor LED array to scan through the wavelengths and illumination angles [77]. Work by Du and colleagues attempted ptychographic optical coherence tomography (OCT) [12] to achieve high-resolution 3D reflectance imaging, although the spectral information was not captured.

Here, we propose using a spectral filter array in the Fourier plane, with broadband white

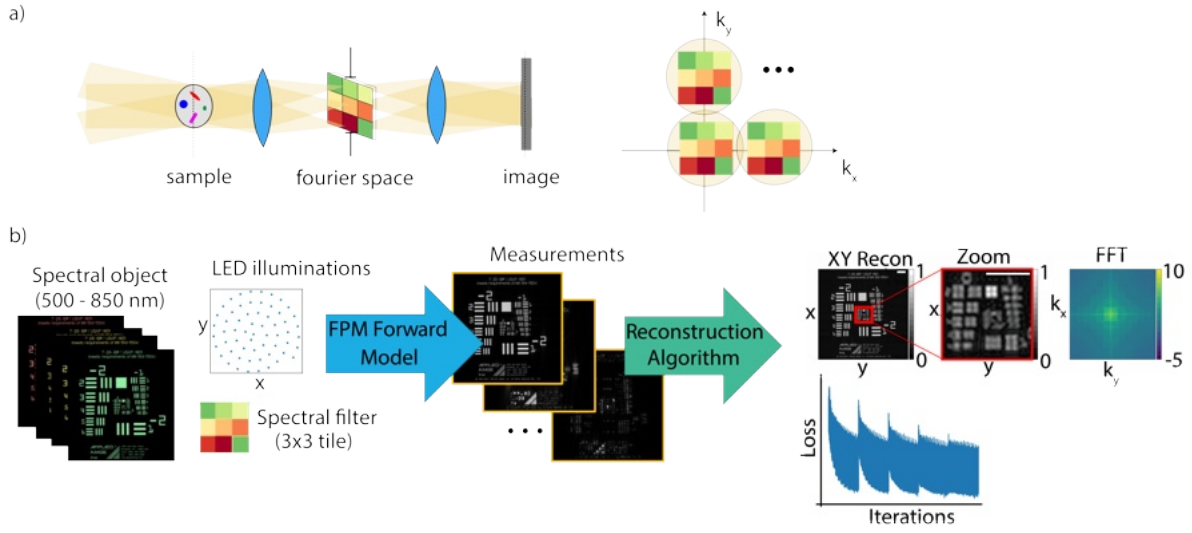

Figure 4.1: Overview of spectral Fourier Ptychography Microscopy (FPM). (a) Optical setup showing the $4f$ system with a spectral filter array (500-850 nm) in the Fourier plane. The k-space diagram illustrates the wavelength-dependent sampling of spatial frequencies at three different illumination angles. (b) Simulation pipeline showing the forward model for measurement generation and inverse reconstruction. Scale bars = 100 μm.

LED illumination, to obtain spectral information at each spatial frequency by scanning the pupil plane in k-space via illumination angle coding. These measurements are then combined to reconstruct a high resolution image at each spectral channel, similar to the typical FPM reconstruction. Our proposed design requires only a single component addition to the FPM system hardware, and non-bulky illumination. The illumination source is still an LED array, but with broadband emitters with a relatively flat emission spectrum in the visible (see Thorlabs Part: MBB1D1 470 - 850 nm Broadband LED). The spectral filter is similar to one used in prior work [39] (available from Viavi Solutions).

As compared to previous work[39] in hyperspectral imaging, our system design significantly relaxes the pixel size requirements on the spectral filter array, making both fabrication and alignment easier. Further, since the spectral filter is placed in Fourier space, rather than at the camera sensor plane, there is no need to remove the sensor's cover glass to install the filter array, nor to align the filter array carefully to the sensor pixels.

4.3 Methods

Given a $4f$ system, placing a spectral filter in the Fourier plane will act as a wavelength-dependent pupil function $P(\lambda, kx, ky)$ (see Fig. **??**a). This pupil function will allow each spatial frequency region to pass a different spectral band, while blocking other wavelengths.

Using an LED array to illuminate the sample with various plane waves at different angles will cause the spatial frequency components to be shifted into the aperture and sampled through multiple acquisitions. The multiple low resolution images containing different spatial frequencies are combined to form a high-resolution image.

The maximum effective resolution of the system after image reconstruction is determined by the size of the filter array and the maximum angle of illumination, as well as the imaging system's numerical aperture (NA), set by the objective lens. It can be approximated by the following equation:

$$\Delta(\lambda) = \frac{\lambda}{2 * (NA_{obj,filter}(\lambda) + NA_{illumination})}, \tag{4.1}$$

where $NA_{obj,filter}(\lambda)$ is the effective NA set by the size of the spectral filter for a given wavelength, as seen through the microscope's objective lens. $NA_{illumination}$ is the effective NA of the illumination, set by the maximum illumination angle used. The key difference from single-color FPM is that $NA_{obj,filter}(\lambda)$ is a function of wavelength and typically smaller than the full NA of the objective due to the spectral filter. Thus, the system will need to scan through more illumination angles to increase the effective resolution beyond the system's native diffraction limit.

Now let's look at the image formation model for this system. The main change from single-color FPM is the wavelength dependence. The object's transmittance, $T(x, y, \lambda)$, is wavelength dependent and so is its Fourier representation, $O(k_x, k_y, \lambda)$. The filter array acts as a wavelength-dependent pupil function, $P(k_x, k_y, \lambda)$. The image formation model is then:

$$\hat{I}(x, y) = \sum_{\lambda} |F^{-1}(F(T(x, y, \lambda) * e^{i(k_{x,illum}x + k_{y,illum}y)}) * P(k_x, k_y, \lambda))|. \tag{4.2}$$

The object transmittance is multiplied by a plane wave at incident angle $(k_{x,illum}, k_{y,illum})$. Then we compute a Fourier transform to represent the object in Fourier space. This is then multiplied by the pupil coding from the filter array, $P(k_x, k_y, \lambda)$. The inverse Fourier transform of this product is taken to propagate out to the image plane. The final image is a sum of the magnitudes over all wavelengths. The spectral response of the image sensor is omitted here for simplicity.

Object reconstruction is done by minimizing the following objective function:

$$\hat{T}(x, y, \lambda) = \arg \min_{\hat{T}(x,y,\lambda)} (\sum_{m} ||I_{m,est}(x, y) - I_{m,actual}(x, y)||_2 + \sum_{k} \tau_k R_k(\hat{T}(x, y, \lambda))). \tag{4.3}$$

The first term is the data fidelity term which minimizes the L2 error between the estimated and actual image over the collected stack of measurements. The second term is a regularization term which applies any chosen spatial/spectral priors to the object. τ_k is a regularization parameter which controls the strength of each kth prior.

For this given object, we found that a combination of total variation (TV) and spectral smoothness worked best. TV is implemented as the L1 norm on the first derivative of the

object along x and y as shown in Equation **??**), and spectral smoothness is the L2 norm on the second derivative of the object along wavelength as shown in Equation **??**.

$$R_1 = ||\frac{d(T(x,y,\lambda))}{dx}||_1 + ||\frac{d(T(x,y,\lambda))}{dy}||_1 \tag{4.4}$$

$$R_2 = \frac{d^2(T(x,y,\lambda))}{d\lambda^2} \tag{4.5}$$

Simulations

For our analysis, we chose a USAF resolution target as our sample object, with the sample transmission varying spatially and spectrally. The object was illuminated with a broadband LED array with set positions and numbers of LEDs. For simplicity, the LED source was assumed to have uniform intensity across all wavelengths (500-850 nm).

First a stack of measurements was simulated using the image formation model in Equation **??**. The measurements were then used to iteratively reconstruct the object transmittance at every wavelength by minimizing the objective function in Equation **??**.

The Fourier coverage at each spectral channel will affect the convergence properties of the reconstruction, and it is generally recognized that significant overlap in Fourier space is required for reliable convergence of the FPM phase retrieval problem [8]. We can analyze the effects of the Fourier coverage here by looking at coverage for a single color channel. Measurements were simulated at NA = 0.05 with a 4× objective at 500 nm. Instead of 3×3 filters, a 1×1 filter was used. 3 epochs were used for reconstruction, and no priors were used.

For multi-color Fourier coverage analysis, measurements were simulated at NA = 0.1 with a 4× objective at 500-850 nm in steps of 50 nm (8 spectral channels total). A spectral filter array containing 3×3 filters from 500 to 800 nm in steps of 50 nm was placed in the Fourier plane. The 500 nm filter was repeated as the first and ninth filter, since only 8 spectral channels were reconstructed and there were 9 sub-filters in the 3x3 array. The spectral filter array design is flexible and can be adapted 5 epochs were used for reconstruction. The regularization hyper-parameters (τ_k) for the spatial and spectral priors were swept from 1e-5 to 1e-2.

All simulations were conducted via Python using Pytorch libraries for GPU acceleration. The objective function was solved using the Adam optimizer [27]; Pytorch's autograd feature [59] was used to compute the gradients of the objective function with respect to the object transmittance and momentum parameters were adjusted to achieve convergence. The object was initialized as fully transparent at all wavelengths. The learning rate was chosen to be 1e-3 and the default momentum parameters for Adam were used. The number of iterations was chosen to be 50 per measurement with at least 3 epochs over the whole dataset (3 for single color and 5 for multi-color). The code base is available at `https://github.com/neerja/spectral_fourier_ptychography`.

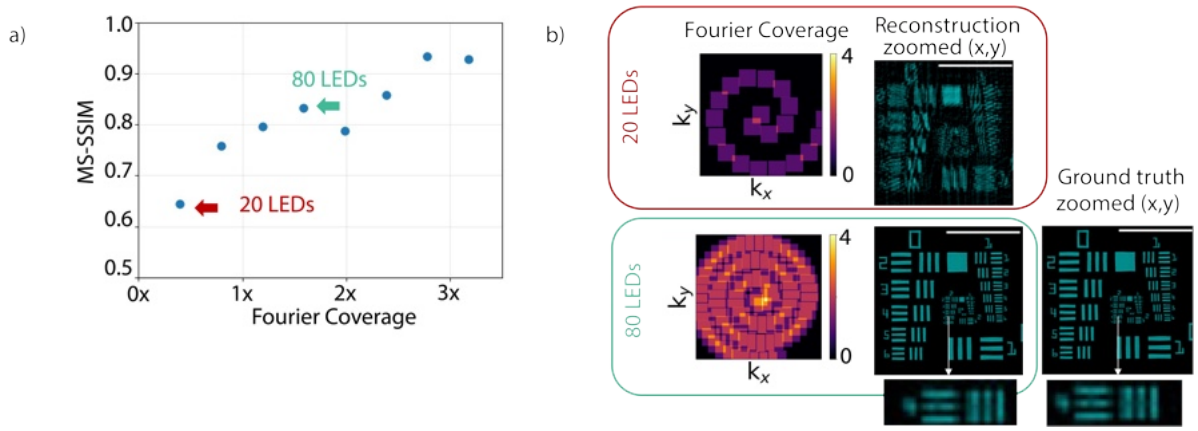

Figure 4.2: Spectral Fourier ptychography analysis of Fourier coverage requirements for each spectral channel. (a) Reconstruction quality measured by the Multi-scale structural similarity index metric (MS-SSIM) versus Fourier space coverage (the proportion of the object's spatial frequencies that are sampled by the measurement scheme) for a single wavelength, showing improved performance with increased sampling density. (b) Example reconstructions with insufficient Fourier coverage (0.5× coverage, 20 LEDs) and sufficient coverage (1.5× coverage, 80 LEDs) demonstrating successful high-resolution recovery. Scale bars = 100 μm

4.4 Results

Single-Color FPM

First we simulated a single-color FPM reconstruction to understand what the overlap needs would be for a the square pupil. Traditional FPM requires a 30-60% overlap between illumination angles to achieve a high resolution reconstruction [8]. which converts to sampling the object's Fourier space effectively 1.5× to 3×. This means each spatial frequency component is sampled at least once. We evaluate reconstruction quality quantitatively (as compared to the ground truth) using the multi-scale structural similarity index metric (MS-SSIM), which results in a higher value for better reconstructions. This image metric evaluates the perceptual similarity between the reconstruction and the ground truth, and tends to match better with visual inspection than typical error metrics like Mean-squared error (MSE).

The plot in Figure **??**a shows the MS-SSIM quality metric increasing for reconstructions with increasing Fourier coverage, from 0.4× to 4×, which corresponds to the number of measurements increasing from 20 to 200. If we look closer at the 0.5× coverage (20 LEDs) shown in the Fig. **??**b, we see that there is insufficient Fourier coverage and thus the reconstruction does not match the ground truth. At 1.5× (80 LEDs), there is appropriate Fourier coverage (most components are sampled 2×) and the reconstruction is better.

Multi-Color FPM

Next we simulated the multi-color measurement. The spectrally varying USAF target had varying transmission in both spatial and spectral dimensions. This is visualized by the single channel transmission images and effective false color transmission shown in Figure **??**a. The effective pupil for different wavelength channels varied given a fixed filter array as shown in Figure **??**b. This is because the the Fourier plane scales with the inverse of the wavelength. For example, the 850 nm effective pupil area was almost 4× smaller than the 500 nm pupil area. Thus we needed roughly 160-500 measurements to get 1.5× coverage at the higher wavelengths.

Figure **??**b shows the reconstruction with varying Fourier coverage (number of measurements: 160, 300, and 500 LEDs). The reconstruction quality improved with more measurements, as expected, and the spectra from the 500 measurements closely matches the ground truth as shown in Fig. **??**c.

Effect of Priors

In a typical experiment, 500 acquisitions would increase the total collection time significantly. Thus, to reduce the number of measurements, we can use data-informed priors to interpolate some parts of the datacube, since our measurements are highly multiplexed. Figure **??**a shows the reconstruction with 160 measurements and varying priors. The reconstruction quality along x, y, and λ improved with the addition of TV and spectral smoothness priors. The spectra for two regions of interest are shown in Fig. **??**c. Although the spectrum improved for the "3" region, it still did not fully match the ground truth. More parameter tuning of the priors could alleviate these artifacts in future work.

4.5 Discussion

So far all our reconstructions have been done using noiseless measurements. In practice, the measurements will be noisy and the reconstruction will need to be robust to noise. We also need to explore additional spectral priors and tuning parameters to achieve higher spectral fidelity. We would also like to explore more representative objects for biological imaging such as stained tissue and cell culture samples. We predict that the stained tissue samples may benefit from pre-trained networks as priors due to the dense scenes. Lastly, we would also like to compare the Fourier sampling effects of using spectral filter array vs a tunable source.

After simulations, we will need to build an experimental setup to test the feasibility of the approach. For this work, we will need to assemble a broadband LED array that may require higher current draw, and thus electronic redesign of past LED arrays developed for FPM. Most FPM is in transmission mode, but previous work in hyperspectral imaging of tissue has been mostly in reflectance. We would need to capture transmission data on thin tissue samples and look for any spectral variations in amplitude or phase of the transmitted

light. Lastly, calibration of the system would involve learning the exact LED positions and positioning of the spectral filter in the pupil plane [13] [45].

As demonstrated by Figure **??** longer acquisition time (i.e. more measurements) allows for higher detailed reconstructions, and the incorporation of priors (Figure **??** could mitigate scan time. Multiplexing LED illuminations could further decrease acquisition time [60].

Thus, spectral FPM may be useful in an application such as rapid onsite evaluation of tissue biopsies where sample prep, imaging, and analysis time is significantly limited to a few minutes [19]. In addition to being label-free, another advantage of spectral FPM is the ability to capture a varying resolution hyperspectral datacube with the same hardware and no moving parts. This allows a low-resolution full-slide scan followed by detailed reconstruction of a few regions of interest without an additional objective.

4.6 Conclusion

We explored a new approach of using a filter array in the Fourier plane to capture spectral, or wavelength, information at each spatial frequency. This hardware architecture is convenient since it only requires a single component change to the FPM system. We showed that data-informed priors can reduce the number of measurements needed to achieve a high-resolution reconstruction. The end goal of this work is multi-spectral gigapixel imaging; our initial results here demonstrate the feasibility of spatial and spectral reconstruction through simulations. Future work includes building an experimental setup to test the approach.

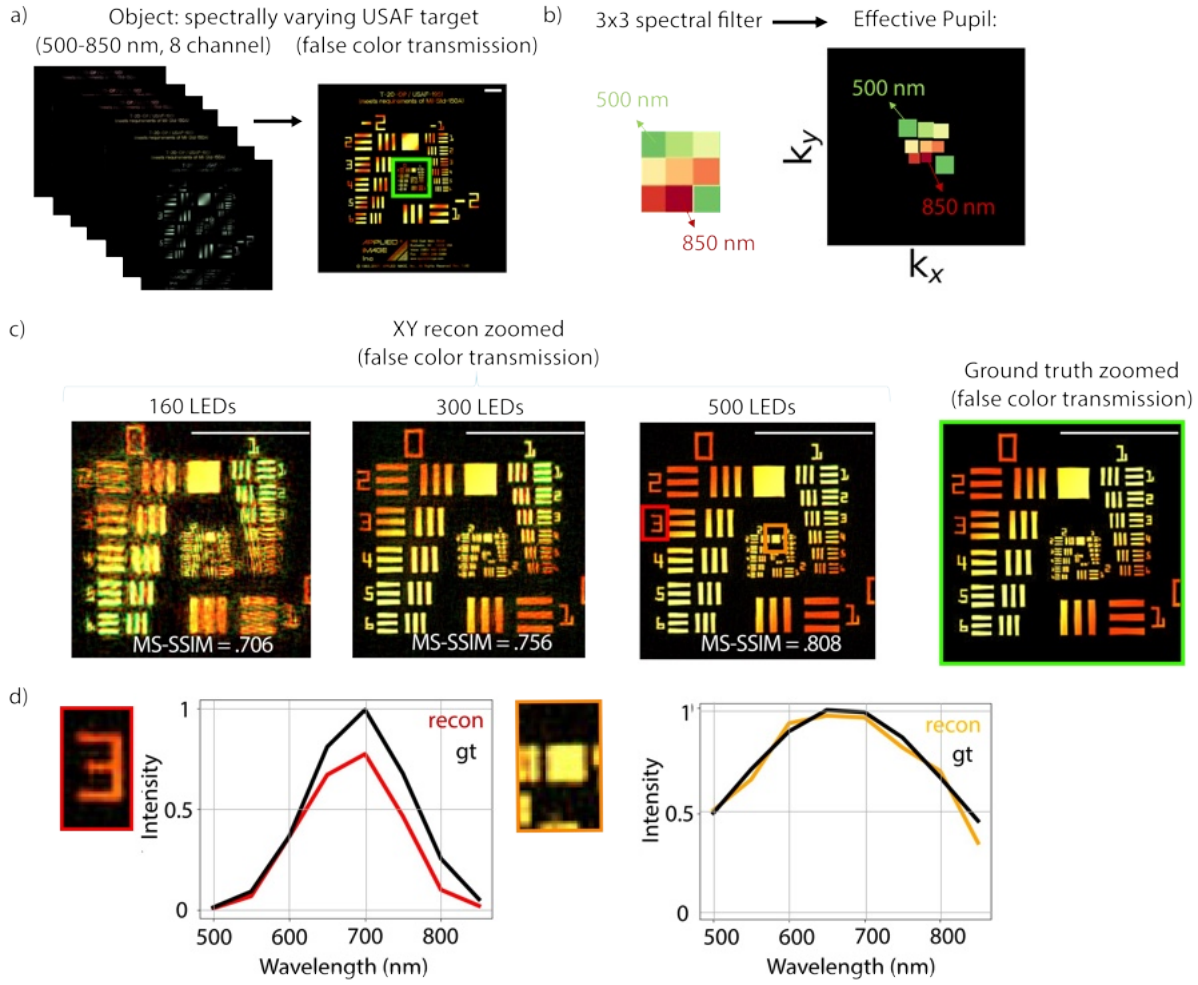

Figure 4.3: Multi-wavelength reconstruction results. (a) Our simulated ground truth spatially and spectrally varying USAF transmission target shown both as a stack and as a single false color image. (b) The 3×3 spectral filter that was placed in the Fourier plane, and the resulting wavelength-dependent Fourier coverage for on-axis illumination. (c) Reconstruction of zoomed region outlined in green in sub-figure a) using increasing density of illumination angles, measured by number of LED measurements (160, 300, and 500). As expected, reconstruction quality improves with increased sampling density. The average MS-SSIM quality metric across all wavelengths is shown at the bottom of each reconstruction. Scale bars = 100 μm. (d) Spectral accuracy comparison between ground truth and reconstructed spectra with 500 measurement for two regions of interest outlined in red and orange in c).

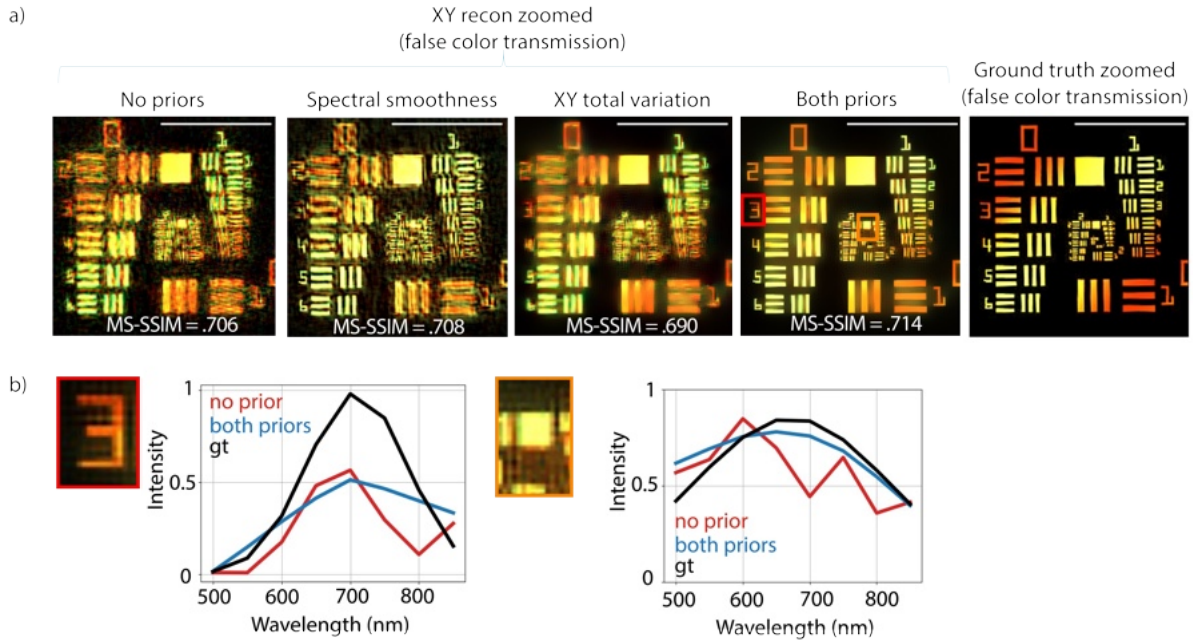

Figure 4.4: Impact of spatial and spectral priors. (a) Simulated reconstructions using 160 measurements with comparison of algorithms with: no priors, only a spectral smoothness prior, only total variation (TV) prior (in the lateral dimensions), and combined TV with spectral smoothness priors. Ground truth is shown on the right. Scale bars = 100 μm (b) Comparison of spectral reconstruction accuracy with and without priors of select regions of interest.

Chapter 5

Conclusion

Computational hyperspectral imaging has many improvements in performance over traditional imaging systems. These include compactness, increases in spatial resolution, and ease of integration with existing microscopy systems. By investigating ways to make minor modifications to existing systems and put some of the load into computation, we can improve performance and enable new applications.

In this thesis, we have presented three computational imaging systems for bioimaging applications. The first system is a compact computational spectrometer that uses a diffuser such as scotch-tape in place of a grating for spectral-domain optical coherence tomography. The second system is a snapshot hyperspectral fluorescence microscope using a diffuser and spectral filter array to multiplex light onto a camera to achieve higher spatial resolution than a traditional approach. The third system is a gigapixel hyperspectral Fourier ptychography system using a spectral filter array in the pupil plane that scans the object's spatial frequencies through each spectral filter to build up a high resolution spatio-spectral datacube. In each of these systems, we explain the optical setup, forward model and reconstruction algorithm. We demonstrate simulation and experimental results for various applications.

5.1 Challenges and open questions

Now we discuss some broader challenges in computational hyperspectral imaging.

Sensors

Multiplexing systems spread out light from a single point onto multiple pixels. Thus dense scenes have washed out measurements with very little intensity variation across sensor on a large background. Additionally, when imaging scenes with both bright and dim components, the exposure had to be set for the brightest component to avoid saturation. This requires sensors with a high well depth and dynamic range. Pixel controllable gain and exposure

would also help to avoid saturation of the measurement which breaks down the forward model accuracy.

Calibration

Model mismatch and calibration errors between theory and experiment were a big challenge in our work. For example, having a spatially varying PSF from an achromatic lens before we switched to a scan lens in our Spectral DiffuserScope project caused poor reconstruction performance. We also expect that the calibration of the spectral filter array in the Fourier Ptychography microscope will pose a challenge. Imagine a situation where after rough alignment of an optical setup, we train the forward model which has learnable degrees of freedom using a calibration dataset. Creating the calibration dataset would require automated data collection on a breadth of hyperspectral samples.

Priors

One open question is the use of priors in scientific imaging. In our work, although we did not train a U-net or similar on a prior dataset, we still had to hand tune the hyperparameters for the optimization algorithm. We carefully chose the priors for each sample based on what prior knowledge would be readily available for that imaging task. This is a challenge in scientific imaging where the goal sometimes is to see something new that doesn't fit an existing prior. Recently, there has been a trend to use trained networks as priors which become even more opaque in understanding. A main reason for using hand-tuned priors is to help the reconstruction algorithm navigate a non-convex optimization landscape. If we can design imaging systems that create better conditioned one-to-one mapping between the object and measurements, we may reduce the reliance on priors.

Large image models

We could also swing in the opposite direction. Large language models have been trained on a diverse set of data. Similarly, if we had large image models that have been trained on diverse set of scientific data along with their downstream analysis steps, then would could use them for image reconstruction. The measurement along with a scientific question or hypothesis could serve as a prompt for the model. The output of the large image model could include the reconstruction along with a specific answer and confidence score relating to the scientific question. One specific example is quantifying the amount of specific protein or cancerous state of a cell from a label free cell image measurement. The hyperspectral imaging system would efficiently encode the hypercube onto a sensor measurement. This sensor measurement would be automatically analyzed to answer the hypothesis. This step could be part of a larger autonomous scientific lab pipeline which is being developed these days.

5.2 Future work

Now we discuss future directions for computational hyperspectral imaging.

Multi-layer spectrometer

The first direction is to extend the work from Chapter 2 where we developed a computational spectrometer by incorporating multiple scattering elements and multiple pinholes. In our experiments we used a single diffuser layer to disperse the light. By introducing multiple scattering elements we hope to improve the resolution within a given form factor. This could be because the single wavelength point spread function may evolve differently between a single stronger scattering diffuser and multiple weaker scattering diffusers. In the first case, we saw that the PSF spreads radially as wavelength increases. In the second, we predict the PSF will change more chaotically which could potentially improve the obtainable resolution. We also do not need the entire sensor pixel area to deduce the spectrum of a single point object. Thus we could image multiple points in the scene using different parts of the diffuser/sensor. One way to do this is having an array of slits or pinholes at the entrance of the spectrometer instead of a single fiber. Finally, a reflective tube could help redirect highly scattered light back into the sensor plane to improve throughput.

Compact fluoroscope for field assays

In Chapter 3, we developed a portable snapshot hyperspectral microscope. The main advantage of a system with no moving parts would be in portable field use and so we had a Master's student explore building a portable version of Spectral DiffuserScope [48]. This system requires further development such as customizing the spectral filter array for a specific application to improve light throughput. It could be useful for MRBLES bead based bioassays in the field or to image the spectra of single cells or other small samples. Another direction is to improve the spatio spectral resolution of the system via end to end optimization of the spectral filter array and diffuser.

The reconstruction algorithm used in Chapter 3 focused on single frames. However, the application of the system is for dynamic samples which would have redundancy between time frames. Thus we could use space-time neural network or parametric gaussian model to represent the 4D hyperspectral data cube. This may help with quickly processing the reconstructions from a stack of acquired images.

Label-free imaging

In Chapter 4 we propose spectral transmission imaging as label-free digital pathology method and develop an imaging system. However, a more fundamental direction is to image the hyperspectral data from unstainined pathology tissue samples and test for a correlation with stained tissue diagnosis. This study could be done with an existing hyperspectral line

scanning system on a brightfield microscope. Deep ultraviolet microscopy has been shown to be useful for digital pathology [23], and so the ptychography system could easily be adapted with UV source, filters, and sensor. Phase and UV microscopy could potentially be useful for developing a rapid onsite analysis system for label-free cervical cancer screening which currently suffers from a follow-up rate.

In label-free cell imaging such as transmission, autofluorescence, and Raman spectroscopy, one common challenge is interpreting the spectra of cell and tissue samples. This requires understanding the relationship between spectra and cell components or cell state. In the past, scientists have deduced peaks by isolating individual components in cells and tissue. For example, previous work showed that the peaks of isolated collagen fibers matched the bulk Raman spectrum of skin tissue [1]. However there are hundreds more components inside cells that may also be contributing to the bulk spectrum. By creating a large dataset where cells are analyzed via both optical spectroscopy and a ground truth method such as mass spectroscopy, we could learn to interpret cell spectra. Additional methods such as genetic editing could help in creating perturbations on a specific cell type to increase the diversity of the dataset. Another approach is to use machine learning to deduce the cell state from the spectrum. Single cell RNA expression profiles have been deduced from Raman spectra using deep learning [28]. However, Raman is only one label-free modality for imaging cells. By training on larger multi-modal datasets between Raman, autofluorescence, phase imaging, polarization imaging, and single cell sequencing, the deduction of cell state from the label-free imaging could become more precise. This dataset could be used for a larger effort in creating foundational models for cells.

Compact imaging systems

The original motivation of this work was using computational imaging to build compact hyperspectral imaging systems. Beyond the applications of microscopy, spectral imaging is also useful for drones, satellite, mobile and wearable imaging. Some of the microscopy systems could easily be adapted for telescopy or photography applications by adjusting the magnification. At the time of this work, the new Meta AI glasses were recently released. Incorporating spectral imaging into these sensors would give the computer vision pipeline additional information about the materials being imaged. For example, food quality at the supermarket could be more accurately assessed along with plant health at home. This way hyperspectral imaging can penetrate people's lives and help us all experience the utility of light-matter interactions.

Bibliography

[1] Aggarwal, Neerja, and M. Eng. Massachusetts Institute of Technology. "Raman and fluorescence spectroscopy of in vitro skin tissue for diagnostics and monitoring". en. PhD thesis. Massachusetts Institute of Technology, 2018.

[2] Neerja Aggarwal and Laura Waller. "Spectral Fourier ptychography using a filter array". en. In: *Three-Dimensional and Multidimensional Microscopy: Image Acquisition and Processing XXXII*. Ed. by Thomas G Brown, Tony Wilson, and Laura Waller. Vol. 13325. SPIE, Mar. 2025, p. 1.

[3] Silke Aumann et al. "Optical coherence tomography (OCT): Principle and technical realization". In: *High Resolution Imaging in Microscopy and Ophthalmology*. Cham: Springer International Publishing, Aug. 2019, pp. 59–85.

[4] Amir Beck and Marc Teboulle. "A fast iterative shrinkage-thresholding algorithm for linear inverse problems". In: *SIAM J. Imag. Sci.* 2.1 (2009), pp. 183–202.

[5] Ayush Bhandari, Achuta Kadambi, and Ramesh Raskar. *Computational Imaging*. en. MIT Press, 2022.

[6] Audrey Bowden, Joe Malone, and Neerja Aggarwal. *diffuserSpec*. en. Nov. 2022.

[7] Graham D Bruce et al. "Overcoming the speckle correlation limit to achieve a fiber wavemeter with attometer resolution". en. In: *Opt. Lett.* 44.6 (Mar. 2019), pp. 1367–1370.

[8] Oliver Bunk et al. "Influence of the overlap parameter on the convergence of the ptychographical iterative engine". en. In: *Ultramicroscopy* 108.5 (Apr. 2008), pp. 481–487.

[9] Hui Cao and Yaniv Eliezer. "Harnessing disorder for photonic device applications". en. In: *Appl. Phys. Rev.* 9.1 (Mar. 2022), p. 011309.

[10] Christy Fernandez Cull et al. "Identification of fluorescent beads using a coded aperture snapshot spectral imager". en. In: *Appl. Opt.* 49.10 (Apr. 2010), B59–70.

[11] Wolfgang Drexler et al. "Optical coherence tomography today: speed, contrast, and multimodality". en. In: *J. Biomed. Opt.* 19.7 (July 2014), p. 071412.

[12] Mengqi Du et al. "Ptychographic optical coherence tomography". In: *Opt. Lett.* 46.6 (2021), p. 1337.

[13] Regina Eckert, Zachary F Phillips, and Laura Waller. "Efficient illumination angle self-calibration in Fourier ptychography". en. In: *Appl. Opt.* 57.19 (July 2018), pp. 5434–5442.

[14] Yinnian Feng et al. "MRBLES 2.0: High-throughput generation of chemically functionalized spectrally and magnetically encoded hydrogel beads using a simple single-layer microfluidic device". en. In: *Microsyst Nanoeng* 6 (Nov. 2020), p. 109.

[15] A F Fercher et al. "Optical coherence tomography - principles and applications". en. In: *Rep. Prog. Phys.* 66.2 (Feb. 2003), pp. 239–303.

[16] Rafael de la Fuente. *Simulating Diffraction Patterns with the Angular Spectrum Method and Python*. en. `https://rafael-fuente.github.io/simulating-diffraction-patterns-with-the-angular-spectrum-method-and-python.html`. Accessed: 2025-3-27.

[17] Liang Gao and R Theodore Smith. "Optical hyperspectral imaging in microscopy and spectroscopy - a review of data acquisition". en. In: *J. Biophotonics* 8.6 (June 2015), pp. 441–456.

[18] R E Gerver et al. "Programmable microfluidic synthesis of spectrally encoded microspheres". en. In: *Lab Chip* 12.22 (Nov. 2012), pp. 4716–4723.

[19] Patrik Gilley et al. "Development and assessment of multiple illumination color Fourier ptychographic microscopy for high throughput sample digitization". en. In: *Sensors (Basel)* 24.14 (July 2024), p. 4505.

[20] Ian Goodfellow, Yoshua Bengio, and Aaron Courville. *Deep Learning*. MIT Press, 2016.

[21] Joseph W Goodman. *Introduction to Fourier Optics, 3rd Edition*. en. Roberts & Company, 2005.

[22] Joseph W Goodman. *Speckle phenomena in optics: Theory and applications*. en. Society of Photo-Optical Instrumentation Engineers (SPIE), Jan. 2020.

[23] Viswanath Gorti et al. "Compact and low-cost deep-ultraviolet microscope system for label-free molecular imaging and point-of-care hematological analysis". en. In: *Biomed. Opt. Express* 14.3 (Mar. 2023), pp. 1245–1255.

[24] Shane M Hickey et al. "Fluorescence microscopy-an outline of hardware, biological handling, and fluorophore considerations". en. In: *Cells* 11.1 (Dec. 2021), p. 35.

[25] Roarke Horstmeyer et al. "Digital pathology with Fourier ptychography". en. In: *Comput. Med. Imaging Graph.* 42 (June 2015), pp. 38–43.

[26] Kedar Khare, Mansi Butola, and Sunaina Rajora. *Fourier optics and computational imaging*. en. 2nd ed. Cham, Switzerland: Springer International Publishing, Jan. 2023.

[27] Diederik P Kingma and Jimmy Ba. "Adam: A method for stochastic optimization". In: *arXiv [cs.LG]* (Dec. 2014).

[28] Koseki J Kobayashi-Kirschvink et al. "Prediction of single-cell RNA expression profiles in live cells by Raman microscopy with Raman2RNA". en. In: *Nat. Biotechnol.* 42.11 (Nov. 2024), pp. 1726–1734.

[29] Sander Konijnenberg, Aurèle J L Adam, and H Paul Urbach. *6.6: Fresnel and Fraunhofer Approximations*. en. https://phys.libretexts.org/Bookshelves/Optics/BSc_Optics_(Konijnenberg_Adam_and_Urbach)/06\%3A_Scalar_diffraction_optics/6.07\%3A_Fresnel_and_Fraunhofer_Approximations. Accessed: 2025-3-27. Jan. 2022.

[30] Maksim Kunitski et al. "Double-slit photoelectron interference in strong-field ionization of the neon dimer". en. In: *Nat. Commun.* 10.1 (Jan. 2019), p. 1.

[31] Zeno Lavagnino et al. "Snapshot Hyperspectral Light-Sheet Imaging of Signal Transduction in Live Pancreatic Islets". en. In: *Biophys. J.* 111.2 (July 2016), pp. 409–417.

[32] Kyung Chul Lee et al. "Design and single-shot fabrication of lensless cameras with arbitrary point spread functions". In: *Optica* 10.1 (Jan. 2023), pp. 72–80.

[33] Seng Fatt Liew et al. "Broadband multimode fiber spectrometer". en. In: *Opt. Lett.* 41.9 (May 2016), pp. 2029–2032.

[34] L Lo Gerfo et al. "Spectral algorithms for supervised learning". en. In: *Neural Comput.* 20.7 (July 2008), pp. 1873–1897.

[35] Guolan Lu et al. "Histopathology Feature Mining and Association with Hyperspectral Imaging for the Detection of Squamous Neoplasia". en. In: *Sci. Rep.* 9.1 (Nov. 2019), p. 17863.

[36] Joseph D Malone et al. "DiffuserSpec: spectroscopy with Scotch tape". en. In: *Opt. Lett.* 48.2 (Jan. 2023), pp. 323–326.

[37] Michael Mazilu et al. "Random super-prism wavelength meter". en. In: *Opt. Lett.* 39.1 (Jan. 2014), pp. 96–99.

[38] George McNamara et al. *Spectral Imaging and Linear Unmixing*. https://www.microscopyu.com/techniques/confocal/spectral-imaging-and-linear-unmixing. Accessed: 2024-10-7. 2024.

[39] Kristina Monakhova et al. "Spectral DiffuserCam: lensless snapshot hyperspectral imaging with a spectral filter array". In: *Optica* 7.10 (2020), p. 1298.

[40] Monica Monici. "Cell and tissue autofluorescence research and diagnostic applications". en. In: *Biotechnol. Annu. Rev.* 11 (Jan. 2005), pp. 227–256.

[41] H Q Nguyen et al. "Programmable Microfluidic Synthesis of Over One Thousand Uniquely Identifiable Spectral Codes". en. In: *Adv Opt Mater* 5.3 (Feb. 2017).

[42] Georg J Ockenfuss et al. *Metal-dielectric optical filter, sensor device, and fabrication method*. Dec. 2015.

[43] Giseok Oh and Hyun Choi. "Simultaneous multifocal plane Fourier ptychographic microscopy utilizing a standard RGB camera". en. In: *Sensors (Basel)* 24.14 (July 2024), p. 4426.

[44] Antony Orth and Kenneth B Crozier. "High throughput multichannel fluorescence microscopy with microlens arrays". en. In: *Opt. Express* 22.15 (July 2014), pp. 18101–18112.

[45] Xiaoze Ou, Guoan Zheng, and Changhuei Yang. "Embedded pupil function recovery for Fourier ptychographic microscopy". In: *Opt. Express* 22.5 (2014), p. 4960.

[46] C V Raman. "A new radiation". en. In: *Indian J. Phys.* 2 (1928), pp. 387–398.

[47] Y Raniwala, N Aggarwal, and L Waller. "Improved fabrication and calibration for snapshot computational hyperspectral imaging". In: *SPIE Proceedings*. Vol. 12363. Mar. 2023, pp. 1236306–1236306–7.

[48] Yashovardhan Raniwala. "Exploring alternative designs for a computational hyperspectral imager for microscopy". en. MA thesis. EECS Department, University of California at Berkeley, May 2023.

[49] Brandon Redding et al. "Compact spectrometer based on a disordered photonic chip". en. In: *Nat. Photonics* 7.9 (July 2013), pp. 746–751.

[50] Brandon Redding et al. "High-resolution and broadband all-fiber spectrometers". en. In: *Optica* 1.3 (Sept. 2014), p. 175.

[51] Rudi Rottenfusser, Erin E Wilson, and Michael W Davidson. *Introduction to Fluorescence Microscopy*. en. `https://zeiss-campus.magnet.fsu.edu/print/basics/fluorescence-print.html`. Accessed: 2025-3-25.

[52] Olivia J Scheideler et al. "Recapitulating complex biological signaling environments using a multiplexed, DNA-patterning approach". en. In: *Sci. Adv.* 6.12 (Mar. 2020), eaay5696.

[53] R A Schultz et al. "Hyperspectral imaging: a novel approach for microscopic analysis". en. In: *Cytometry* 43.4 (Apr. 2001), pp. 239–247.

[54] Qiushuai Shi et al. "Under-sampling reconstruction with total variational optimization for Fourier ptychographic microscopy". en. In: *Opt. Commun.* 492.126986 (Aug. 2021), p. 126986.

[55] Srinivasan Sivanandan et al. "A pooled Cell painting CRISPR screening platform enables de novo inference of gene function by self-supervised deep learning". en. In: *bioRxiv* (Aug. 2023), p. 2023.08.13.553051.

[56] Jiasong Sun et al. "Single-shot quantitative phase microscopy based on color-multiplexed Fourier ptychography". en. In: *Opt. Lett.* 43.14 (July 2018), pp. 3365–3368.

[57] Martín Testa-Anta et al. "Raman spectroscopy to unravel the magnetic properties of iron oxide nanocrystals for bio-related applications". en. In: *Nanoscale Adv.* 1.6 (June 2019), pp. 2086–2103.

[58] The Event Horizon Telescope Collaboration et al. "First M87 event horizon telescope results. I. the shadow of the supermassive black hole". en. In: *Astrophys. J. Lett.* 875.1 (Apr. 2019), p. L1.

[59] The Linux Foundation. *The Fundamentals of Autograd*. `https://pytorch.org/tutorials/beginner/introyt/autogradyt\_tutorial.html`. Feb. 2024.

[60] Lei Tian et al. "Multiplexed coded illumination for Fourier Ptychography with an LED array microscope". en. In: *Biomed. Opt. Express* 5.7 (July 2014), pp. 2376–2389.

[61] J A Timlin et al. "Hyperspectral imaging of biological targets: The difference a high resolution spectral dimension and multivariate analysis can make". en. In: *2004 2nd IEEE International Symposium on Biomedical Imaging: Macro to Nano (IEEE Cat No. 04EX821)*. IEEE, 2005, 1529–1532 Vol. 2.

[62] Marika Valentino et al. "Beyond conventional microscopy: Observing kidney tissues by means of fourier ptychography". en. In: *Front. Physiol.* 14 (Feb. 2023), p. 1120099.

[63] Ashwin Wagadarikar et al. "Single disperser design for coded aperture snapshot spectral imaging". en. In: *Appl. Opt.* 47.10 (Apr. 2008), B44–51.

[64] Peng Wang and Rajesh Menon. "Computational spectrometer based on a broadband diffractive optic". In: *Opt. Express* 22.12 (2014), p. 14575.

[65] John Wright and Yi Ma. *High-Dimensional Data Analysis with Low-Dimensional Models: Principles, Computation, and Applications*. Cambridge University Press, 2022.

[66] Jiamin Wu et al. "Snapshot Hyperspectral Volumetric Microscopy". en. In: *Sci. Rep.* 6 (Apr. 2016), p. 24624.

[67] Yagi Laboratory. *Computational Imaging*. en. `http://www.am.sanken.osaka-u.ac.jp/research\_/ci-en/`. Accessed: 2025-3-25. 2011.

[68] T Yang et al. "Compact Spectrometer Based on a Frosted Glass". In: *IEEE Photonics Technol. Lett.* 29.2 (Jan. 2017), pp. 217–220.

[69] Zongyin Yang et al. "Miniaturization of optical spectrometers". en. In: *Science* 371.6528 (Jan. 2021), eabe0722.

[70] Erika Ye et al. "Miniature, sub-nanometer resolution Talbot spectrometer". en. In: *Opt. Lett.* 41.11 (June 2016), pp. 2434–2437.

[71] Jinzhou Yuan, Jenny Sheng, and Peter A Sims. "SCOPE-Seq: a scalable technology for linking live cell imaging and single-cell RNA sequencing". en. In: *Genome Biol.* 19.1 (Dec. 2018), p. 227.

[72] Fabian Zanella, James B Lorens, and Wolfgang Link. "High content screening: seeing is believing". en. In: *Trends Biotechnol.* 28.5 (May 2010), pp. 237–245.

[73] Peiwei Zhang et al. "Hyperspectral microscopy imaging based on Fourier ptychographic microscopy". en. In: *J. Opt.* 24.5 (Mar. 2022), p. 055301.

[74] Zhengyang Zhang et al. "Ultrahigh-throughput single-molecule spectroscopy and spectrally resolved super-resolution microscopy". en. In: *Nat. Methods* 12.10 (Oct. 2015), pp. 935–938.

[75] Guoan Zheng et al. "Concept, implementations and applications of Fourier ptychography". en. In: *Nat. Rev. Phys.* 3.3 (Feb. 2021), pp. 207–223.

[76] Haowen Zhou et al. "Fourier ptychographic microscopy image stack reconstruction using implicit neural representations". en. In: *Optica* 10.12 (Dec. 2023), p. 1679.

[77] You Zhou et al. "Fourier ptychographic microscopy using wavelength multiplexing". en. In: *J. Biomed. Opt.* 22.6 (June 2017), p. 66006.